NUMERICAL SIMULATIONS AND SENSITIVITY STUDIES OF A

FLORIDA SEA BREEZE AND ITS ASSOCIATED CONVECTION

IN THE GRAY-ZONE GRID SPACING

by

Nessa E. Hock

A thesis submitted to the faculty of
The University of Utah
in partial fulfillment of the requirements for the degree of

Master of Science

Department of Atmospheric Sciences

The University of Utah

August 2017

The University of Utah Graduate School

STATEMENT OF THESIS APPROVAL

The thesis of   **Nessa E. Hock**

has been approved by the following supervisory committee members:

Zhoaxia Pu	, Chair	**03/22/2017**
		Date Approved
Steven K. Krueger	, Member	**03/22/2017**
		Date Approved
John Chun-Han Lin	, Member	**03/22/2017**
		Date Approved

and by   **Kevin Perry**   , Chair/Dean of

the Department/College/School of   **Atmospheric Sciences**

and by David B. Kieda, Dean of The Graduate School.

ABSTRACT

The Florida (FL) peninsula has the most frequent occurrence of warm-season thunderstorms in the US, with the majority of this convection initiated by the sea breeze (SB) circulation. Previous numerical studies of FL SB convection have emphasized either large mesoscale grid scales (tens of kilometers or greater) or much smaller large-eddy simulation (LES) grid scales (less than a hundred meters). Few studies have been conducted in the numerical *gray-zone* scale (e.g., 1-5 km). In this thesis, numerical simulations of a convective FL SB case study are conducted using an advanced research version of the Weather Research and Forecasting (WRF) model with gray-zone grid spacing and 40 different simulation configurations. Simulations are evaluated against surface observations and analysis data to determine the accuracy of the model-simulated SB convective initiation (CI). The dependence of the SB and its associated convection on variations in physics parameterizations, initial conditions (ICs), stochastic perturbations, and grid scale spacing is also evaluated.

Results indicate that the WRF model can realistically reproduce the SB CI. However, large sensitivities of simulations to boundary layer parameterizations, ICs, grid scale, and stochastic perturbations of potential temperature and wind tendency fields are found in predicting the timing and intensity of the SB and its associated convective systems. Further analysis indicates that the specific representation of atmospheric variables (e.g., sensible surface heating, synoptic winds, and low-level convergence) and

geophysical features (e.g., coastline shape and lake resolution) within the simulations are

important for the accurate representation of the timing, location, and intensity of the SB

and its associated convection.

TABLE OF CONTENTS

LIST OF TABLES

Tables

ACKNOWLEDGEMENTS

CHAPTER 1

INTRODUCTION

In the United States, central Florida (FL) has the highest annual number of days with convective rainstorms (Williams et al. 1992). In the summertime, it experiences an almost daily occurrence of thunderstorms. Hazards of thunderstorms include strong surface winds (which can result in low-level wind shear and extreme turbulence), heavy rain (which can cause localized flooding and impact visibility), lightning, hail, and reduced visibility and ceilings. These hazards lead to impacts on local transportation, the economy (e.g., tourism), and restrict flight and ground operations at airports and military installations. There are over 100 public use airports, 2 spaceports, and 12 aviation-related military installations located across the FL peninsula (Figure 1.1), whose ground, maintenance, and flight operations are severely restricted by the onset of thunderstorms. These summertime convective events often develop and move quickly, are relatively short-lived, and can occur over small distances, making them one of the primary forecasting challenges for meteorologists in this region (Watson and Zavodsky 2015). The summer maximum in FL thunderstorms is primarily linked to the initiation and propagation of the sea breeze (Byers and Rodebush 1948).

A sea breeze (SB) is a local mesoscale circulation generated when a large temperature gradient between the warmer land surface and the cooler ocean surface

creates boundary layer pressure differences, which in turn, leads to a diurnal system of breezes that propagate inland (Abbs and Physick 1992). Consider a coastline with a uniform temperature field across both land and water. After sunrise, the water will heat much slower than the land surface due to its higher heat capacity and its ability to transfer heat downward from the ocean surface to much lower depths through turbulent mixing. Once the land surface has heated significantly over the water surface, the initiation of the SB will begin. According to Walsh (1974), at least a 3°C land-sea temperature difference is needed to initiate the SB. The energy from the sensible heating of the land surface is distributed upward by mixing, leading to a thermal expansion of the air and an increase of pressure aloft, but a decrease in air pressure directly over the land surface, relative to that over water. This change in pressure produces the sea breeze circulation (SBC): an outflow of air from the near-coastal ocean areas to the land at the surface called the sea breeze gravity current (SBG), leading to convergence of rising air currents inland at the edge of the SBG called the sea breeze front (SBF), a much weaker return current (RC) above the SBG flowing from the land to ocean, leading to divergence of sinking currents several kilometers out to sea (Miller et al. 2003).

Due to its diurnal nature, the SB strength reaches a maximum an hour or two after the largest temperature gradient between the land and sea is reached (i.e., early afternoon) and then slowly declines before dissipating in the evening, usually several hours after sunset (Haurwitz 1947). Following the loss of surface heating at sunset, the land cools more rapidly than the water and the process reverses itself with the formation of the weaker land breeze circulation at night. The strength of the SBCs are proportional to the magnitude of the land-sea temperature gradients, with observational and modeling studies

indicating that the average depth of the SB ranges from 200 to 1,400 m, while the inland penetration of the SB usually ranges from 40 to 150 km (Abbs and Physick 1992).

As the SB propagates inland, the SB frontal boundary will force the ascent of the continental air mass above the maritime air mass through enhanced low-level convergent forcing. If the ascending air reaches its level of free convection (LFC) and maintains sufficient buoyancy through significant upward displacement, shallow cumulus (cu) or deep convective initiation (CI) may occur (Miller et al. 2003; Trier 2003). Thus, the SBF is a favored low-level convergence boundary line for thunderstorm development. The FL peninsula averages 160 to 240 km wide and 725 km long, giving it the longest coastline (1,926 km) in the contiguous United States. This lengthy coastline makes FL a natural laboratory to study SBs and their associated CI (Song 1986).

Numerous observational (Blanchard and Lopez 1985; Atkins and Wakimoto 1997; Weaver 2006) and numerical studies (Bechtold et al. 1991; Nicholls et al. 1991; Boybeyi and Raman 1992; Arritt 1993; Gilliam 2004) have indicated that the synoptic-scale flow plays an important role in the strength and inland penetration of the FL SBs. Onshore synoptic flow tends to create weaker SBs that propagate long distances, offshore synoptic flow tends to create stronger SBs that propagate only a short distance inland due to the opposing synoptic flow, and coast-parallel flow tends to create SBs whose magnitudes are between the onshore and offshore cases, but propagate only slightly further inland than offshore flow cases (Atkins and Wakimoto 1997). Blanchard and Lopez's (1985) work was one of the first studies to link synoptic wind patterns with south FL's observed radar data, leading to a classification of three basic SB convective patterns or "Types."

A "Type 1" SB event is typified by southeasterly synoptic flow, leading to the development of a weak east coast sea breeze (ECSB) and a strong west coast sea breeze (WCSB). The ECSB moves significantly inland, while the WCSB moves slightly inland, leading to SBF merger and significant rainfall over the west-central portion of the peninsula. Similar to the "Type 1," a "Type 2" SB event 1is typified by easterly synoptic flow and a weak and less convective ECSB moving inland, while a stronger WCSB develops and does not propagate inland, leading to a merger of the SBFs directly along the western FL coast producing sparser rainfall amounts. A "Type 3" SB event is typified by southwesterly synoptic flow, leading to a weak WCSB that moves considerably inland and strong ECSB that moves only slightly inland. The two convective zones meet in the east-central portion of the peninsula, producing strong convective rainfall amounts.

The similarities and differences in the CI by various FL SB convergence lines has been investigated in numerous observational and numerical studies (e.g., Byers and Rodebush 1948; Ulanski and Garstang 1978; Tripoli and Cotton 1980; Burpee and Lahiff 1984; Pielke 1974; Nicholls et al. 1991; Boybeyi and Raman 1992; Arritt 1993; Rubes et al. 1993; Fankhauser et al. 1995; Halverson et al. 1996; Xu et al. 1996; Wilson and Megenhardt 1997; Rao and Fuelberg 2000; Etherton and Santos 2008). These, and other studies, have shown that the CI produced along the SB's convergent boundary occurs at discontinuous locations along the SBF, rather than in an uninterrupted line. These locations of preferred CI have been shown to occur where the SBF collides or merges with other boundary convergence lines such as: thermally-driven mesoscale breezes on the order of sea, river, or land breezes (Blanchard and Lopez 1985; Boybeyi and Raman 1992; Laird et al. 1995; Baker et al. 2001), gust front (GF) or outflow boundaries

(Nicholls et al. 1991; Fankhauser et al. 1995; Rao and Fuelberg 2000), or microscale horizontal convective roll (HCR) updrafts (Fankhauser 1995; Rao and Fuelberg 2000; Ogawa et al. 2003; Fovell 2005).

Moreover, it has been found that CI can also occur ahead of or behind the SBF, though the convection produced in this manner is often much weaker and more short-lived than the convection that occurs along the SBF. Observations and numerical simulations by Nicholls et al. (1991) and Fankhauser et al. (1995) noted that convection initiation could develop prior to the merger of two SBFs within an enhanced convergence zone formed as a natural consequence of declining surface heating and the inland progression of the two SBFs. Fovell (2005) conducted a high-resolution, three-dimensional numerical simulation that showed that an intersecting HCR's moist updraft interacting with obstacle-generated gravity waves produced a convective roll cloud ahead of the SBF. More recently, Abulikemu et al. (2016) have investigated CI prior to the merger of a SBF and gust front in North China and found that low-level convergence, conditional instability, and dynamic vertical forcing were the key ingredients for the CI produced between the two boundaries. Convection behind the stable SBF has been studied in high-resolution numerical simulations produced from an outflow boundary intersecting a deep layer of upward motion that was enhanced and carried by microscale Kelvin-Helmholtz billows (KHBs) along the top of the SBG (Rao and Fuelberg 2000) or intersecting outflow boundaries modified and enhanced by the placement of the SBF (Fankhauser et al. 1995).

From aforementioned studies, it is evident that the mesoscale SB and its associated convection is highly affected by locally driven boundaries and microscale

features that change on a daily, and even hourly basis, that make forecasting the exact

timing, location, and intensity of the convective systems difficult to predict.

Observational studies have aided in our understanding of how CI is produced from SBs;

however, this and other types of warm-season convection are still among the most

difficult atmospheric events to predict (Clark et al. 2014, Lock and Houston 2014).

Operational numerical weather prediction (NWP) models have long been used to bridge

the gaps in forecasters' ability to predict warm season CI due to the FL SB and aid in the

generation of their forecasts (Miller et al. 2003; Hahmann et al. 2006; Crosman and Horel

2010).

Current operational NWP models are generally run as regional models. Regional

models are nonhydrostatic models whose grid scales usually encompass that of 10-18 km

grid spacing (with some regional models now running at less than 10 km) and obtain their

boundary conditions from a coarser global model. However, these global and regional

models have been found to be unable to properly resolve local-scale weather features that

influence SB CI (Watson and Zavodsky 2015), as their horizontal resolution is too coarse

to resolve the important subgrid meteorological processes. The Intergovernmental Panel

on Climate Change (IPCC) states that the source of most large-scale errors is that "many

important small-scale processes cannot be represented explicitly in model" (Randall et al.

2007), as these subgrid features can only generally be accounted for by parameterization

processes in these models.

Physical parameterization is a method of representing subgrid processes that are

too small or complex to be physically represented in the model by a more simplified

process or resolvable scale field, thus allowing for less degradation of the forecast than

omitting the subgrid processes entirely. However, while lessening the effects of degrading the model forecast, parameterization of these subgrid processes also introduces a different source for systematic model errors. In order to significantly reduce this source of errors in models, the much smaller large-eddy simulation (LES) domain is often used. A LES model has a horizontal grid scale of a hundred meters or less have been found to be a useful method in modeling the convection produced by the interactions of the SBs with the aforementioned microscale features such as HCRs or KHBs (e.g., Rao and Fuelberg 2000; Fovell 2005). At the much smaller LES domain resolution, the subgrid processes that had been previously parameterized at the larger grid can now be explicitly resolved. However, due to the extremely fine horizontal resolution of the LES, a large amount of computing power is required, so they can only be effectively run in a simulation domain of a few kilometers, making it inefficient for use of forecasters to use in an operational setting.

Between the regional and LES domain scales lies what is known as the numerical *gray-zone* scale (Hong and Dudhia 2012). This gray scale, or what Wyngaard (2004) refers to as the *terra incognita*, is composed of grid sizes on the order of the scale of a few kilometers. The gray-zone contains grid sizes small enough to explicitly resolve some model dynamics that were previously parameterized at larger grid sizes, such as cumulus parameterizations (thus reducing a source of model error), yet is still not fine enough to resolve all the boundary-layer interactions without some sort of implicit model parameterization (which reduces computer processing requirements).

In addition to the inability of regional models to resolve microscale features (and some mesoscale features) in their horizontal domain resolution, the relatively short time

scales of these processes also prove a challenge for NWP models to accurately capture these features in the initial conditions (ICs) of the model. It is well known that small errors in the ICs can lead to growing errors in the forecast (Kalnay 2003). A number of numerical studies have emphasized the importance of ICs in the prediction of the SB and its associated convection (Berri and Paegle 1990; Zhang et al. 2005; Srinivas et al. 2006; Watson 2007; Etherton and Santos 2008; Lombardo et al. 2016), as uncertainty in the representation of atmospheric (e.g., surface winds, pressure, relative humidity, precipitation, radiation, cloud cover, etc.) and land surface (e.g., temperature, soil moisture, terrain, coastline, etc.) ICs, lead to widely differing SBC and precipitation forecasts.

The ability for a NWP model to make as skillful forecast requires that the model be a realistic representation of the atmosphere (i.e., has correct dynamics and parameterizations) and that the ICs be known accurately (Kalnay 2003). Results from NWP work indicate that model errors in model resolution (grid spacing, parameterization, etc.), initial and boundary conditions, and systematic model errors (i.e., model bias) are the main factors that lead to model discrepancies and errors (Kalnay 2003). As the current operational weather centers' computing power has advanced to the point of allowing regional numerical simulations in the gray-zone grid scales of 1-4 km (Hong and Dudhia 2012), research into the strengths and weaknesses in how the gray-zone models handle the dynamics, physical parameterizations, geophysical characteristics, boundary-layer effects, etc., in simulating various atmospheric phenomena is of pressing importance in aiding future improvements to NWP forecasts. *However, relatively few of the numerical studies mentioned previously have simulated a*

real-data case study of FL SB convection in the gray scale in order to examine how the

model's ability to accurately forecast the FL SB and its associated convective systems.

Moreover, within the last ten years, a new area of NWP research on unresolved

atmospheric features has emerged called stochastic parameterization. This method

involves representing atmospheric processes as a combination of a predictable

deterministic component and an unpredictable and randomly determined (i.e., stochastic)

component. While traditional deterministic parameterization schemes represent the bulk

average estimate of unresolved subgrid scale processes on the resolved flow, stochastic

parameterization represents the statistical variability of these unresolved processes (i.e.,

perturbations) within the NWP model (Duda et al. 2016; Christensen et al. 2017).

Equations 1.1 and 1.2 below illustrate the differences between physics parameterizations

(Equation 1.1) and stochastic parameterizations (Equation 1.2).

$$\frac{\partial X}{\partial t}\bigg|_{total} = \frac{\partial X}{\partial t}\bigg|_{dynamics} + \frac{\partial X}{\partial t}\bigg|_{physics} \qquad (1.1)$$

$$\frac{\partial X}{\partial t}\bigg|_{total} = \frac{\partial X}{\partial t}\bigg|_{dynamics} + \frac{\partial X}{\partial t}\bigg|_{physics} + \frac{\partial X}{\partial t}\bigg|_{stoch} \qquad (1.2)$$

The term on the left sides of the two equations represent the local tendency for a

variable *x,* while the 1st terms on the right side of the equations represent the dynamical

tendencies (i.e., the resolved scales of the model). The 2nd terms on the right sides of

Equations. 1.1 and 1.2 represent the physical tendencies (bulk-averaged unresolved

scales), while the 3rd term on the right side of Equation 1.2 represents the additive

stochastic perturbation tendency (from an unresolved scale). While the physical

tendencies predict the most likely subgrid scale motion, the stochastic perturbations

represent one possible realization of the subgrid feature or process.

The stochastic perturbation ensemble method has shown to be successful in

operational and research forecast studies (Berner et al. 2008, 2009, 2011, 2012). *Despite a decade of study, the use of stochastic parameterization schemes in gray-zone grid spacing is relatively new*, though several studies of note have been conducted at this scale. Romine et al. (2014) found that stochastic perturbed simulations at 3-km grid spacing showed skill in ensemble mean forecasts but decreased deterministic ensemble member forecast skill. Charron et al. (2010) determined that a stochastic perturbation scheme applied to physical tendencies was pronounced in improving the probabilistic skill of the low-level winds at 1-2 km grid spacing. Duda et al. (2016) conducted stochastic perturbations on warm season convection allowing probabilistic forecasts at gray-zone grid spacing, finding it produced improvements for mid- and upper-tropospheric fields, but found that it had less improvements at the surface compared to an ensemble of mixed physics simulations.

In light of all the above problems and advances, the overarching goal of this study is to improve the understanding of predictive ability of the state-of-the-art NWP model for the FL SB and its associated CI in gray-zone simulations. In order to accomplish this, an evaluation of various physics parameterization schemes, ICs, and stochastic parameterizations on the model's ability to accurately simulate the FL SB convection is conducted. In addition, an evaluation of the sensitivity of the numerical model in its ability to simulate the characteristics of a SB and its associated CI at various gray-zone grid resolutions is performed. Special attention is paid to verifying how the model resolves the timing, location, and intensity of the SB convection as well as the effects of geophysical factors on convective ingredients and the interactions between the SB and its associated convective characteristics in the gray-zone. Finally, an evaluation of the

model's performance using a stochastic perturbation scheme is accomplished in order to determine the effect on added subgrid energy effects to the gray-zone simulations.

A description of the SB convection case study and the Weather Research and Forecasting (WRF) model used for this study is presented in Chapter 2, along with the experimental setup for the parameterization and initialization sensitivity studies. Results from the parameterization and IC simulations testing SB convection are presented in Chapter 3. Further analysis of the "best" simulation from Chapter 3 and the effects of differing gray-zone grid spacing on resolving atmospheric and geophysical features are presented in Chapter 4. A description and analysis of the impact of a stochastically perturbed simulations on the SB convection is given in Chapter 5. A summary and concluding remarks are given in Chapter 6.
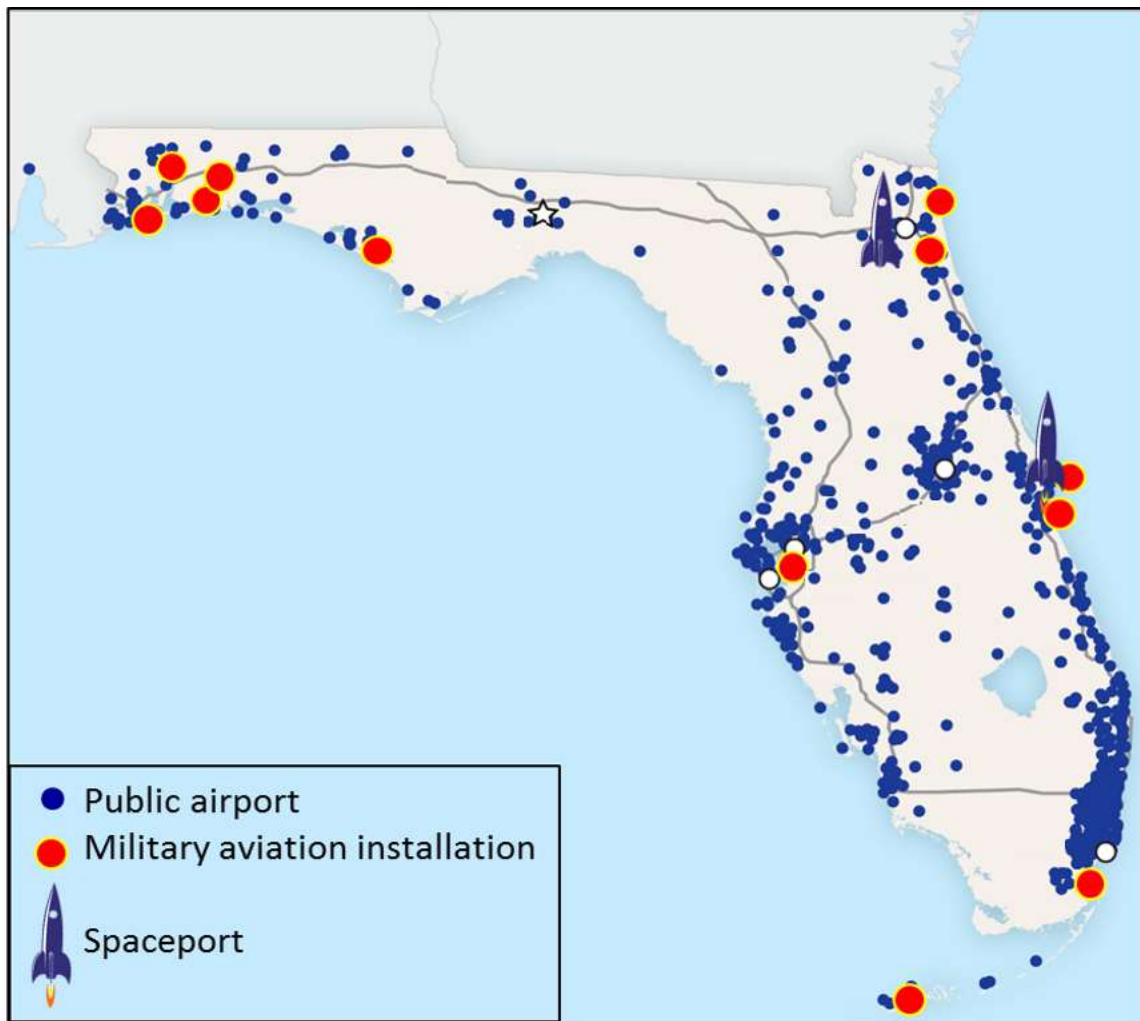
Figure 1.1 Map of Florida's major aviation and aerospace installations.

CHAPTER 2

DESCRIPTION OF SEA BREEZE CONVECTION CASE AND

CONFIGURATION OF NUMERICAL SIMULATIONS

The accurate representation of the small-scale features affecting and interacting

with the FLSB is crucial for high-quality thunderstorm forecasts. Therefore, a case study

is conducted to investigate how well the WRF model can represent the gray-zone

environmental features supporting SB development and the convective systems produced

therein based on the configurations chosen for physics parameterizations and ICs. A case

study for a FL SB convection event was chosen for the WRF model simulations.

Following a control simulation of the chosen SB convection case study, an ensemble of

various physics parameterization and initial conditions (P/IC) simulations is run in order

to test the sensitivity of the model to these processes in the gray-zone grid spacing.

2.1 An Overview of a Florida Sea Breeze Convection Case

The case study chosen for our simulations occurred 6-7 September 2012. This

case was characterized by SB convergences and convective developments typified by a

fast-moving WCSB and slow-moving ECSB. According to Blanchard and Lopez (1985),

this is a classic "Type 3" SB pattern, characterized by heavier rainfall amounts and SB

convection that is sustained through the late evening hours. Figure 2.1 illustrates the

surrounding synoptic features for 1200 UTC 6 September 2012 at the 850-hPa-pressure level. At this level, a ridge of surface high pressure to the south is centered over the Atlantic Ocean, a weak shortwave trough to the north is located over the southeastern US, and a low-pressure system is situated over the Gulf of Mexico (remnants from Tropical Storm Isaac). At the 300 hPa pressure level (Figure 2.2) for this same time, a low-pressure system over the Atlantic is evident to the east over the Bahamas, producing north-northeasterly flow in the upper-levels over the FL peninsula and weak subsidence in place on the back (western) side of the low. This large-scale synoptic pattern induced warm-air advection from the south and vertical lifting over the peninsula, aiding in a quicker destabilizing of the atmosphere. The south-southwesterly flow induced at the surface and eastward synoptic motions creating enhanced vorticity and wind shear over the FL peninsula significantly influenced the mesoscale SB forces.

This onshore synoptic flow modified the WCSB, weakening the SBF, but aiding in its inland movement so that it penetrated faster and farther into the interior of the peninsula than did the contrasting ECSB, whose inland propagation speed and progression were significantly impeded by the offshore synoptic flow. This synoptic flow pattern led to a broad, indistinct, and discontinuous WCSB front, while the strengthened ECSB had a narrow, distinct, and continuous front, indicative of a sharply compressed land-sea thermodynamic gradient. The southwesterly onshore (offshore) synoptic winds played a significant role in weakening (strengthening) SB frontal characteristics, while aiding (inhibiting) inland propagation distance and speed and increasing (decreasing) the SB head and circulation depth. The effects of synoptic winds over FL's irregular coastlines on SB frontal characteristics are well documented (e.g., Boybeyi and Raman

1992; Atkins and Wakimoto 1997).

Figure 2.3 shows the soundings at 1200 UTC 6 September 2012 [hereafter all times are in UTC, UTC = EDT (Eastern Daylight Time) + 4 h] from four FL stations: Tallahassee (purple line), Jacksonville (red line), Tampa Bay (black line), and Miami (blue line). These soundings represent the atmospheric conditions about an hour after sunrise, several hours before the SBs are initiated. All four soundings show convective inhibition (CIN) values less than 25 J kg^{-1} and convective available potential energy (CAPE) values ranging from almost 900 J kg^{-1} (TLH) to over 2,500 J kg^{-1} (MFL). The level of free convection (LFC) for each of the four soundings is between 895 and 850 hPa, while the lifting condensation level (LCL) for each of the four soundings ranges between 970 and 950 hPa. Precipitable water (PW) values for the soundings are around 48 mm, except for JAX, which is slightly less than that of the other soundings at 42 mm. Consequently, the soundings for the stations across the peninsula show a warm, moist, and unstable atmosphere favorable for the SB convection event, given that the weak subsidence and associated CIN over the peninsula could be overcome in the afternoon through convective heating and lifting effects.

A day before this event (5 September 2012), SB convection also occurred during the afternoon and extended to the evening hours. However, by 0600 UTC on 6 September 2012, the sky over FL was mostly clear and cloud free for the rest of the morning, allowing for plenty of morning insolation to occur over the peninsula. Both the west coast and east coast SBs developed between 1340 and 1420 UTC 6 September 2012, while convection began along the WCSB at 1400 UTC (Figure 2.4a) and along the ECSB at 1600 UTC (Figure 2.4b) 6 September 2012, respectively. The enhanced WCSB and its

associated convection traveled significantly inland, while the ECSB and convection remained adjacent to the east coast for most of the period. As the SBFs propagated inland, they continued to initiate robust thunderstorms, clearly visible in Figure 2.4 with the towering cumulonimbus tops being sheared to the southwest by the upper-level northeasterly flow. This upper -level flow aided the WCSB convection as the lack of the cumulonimbus cloud debris ahead of the WCSB front aided in increased surface heating and destabilization of the atmosphere. The two SBs collided just inland of the eastern coast of FL at 2030 UTC 6 September 2012 (Figure2.4h), producing a strong squall line of enhanced deep convection. The deep convection produced by the colliding SBs was oriented in a north-to-south line along Interstate 95 from Jacksonville (JAX) to Vero Beach (VRB), while the convection to the south was oriented in a northeast-to-southwest line across the peninsula from VRB to just inland and north of Naples (APF). Following the production of this squall line at 2100 UTC 6 September 2012, there were several reports of 60 mph winds along the southeast coast of FL. The last remnants of convective precipitation associated with the SB event ended at 0500 UTC 7 September 2012 in east-central portions of the FL peninsula.

2.2 Description of WRF Numerical Simulations

2.2.1 Model Description and Setup

The numerical simulations of SB convection presented in this paper were performed using an advanced research version of the Weather Research and Forecasting [Advanced Research WRF (WRF-ARW)] model (version 3.7.1) developed by the National Center for Atmospheric Research (NCAR) in conjunction with National Centers

for Environmental Prediction (NCEP), Earth System Research Laboratory (ESRL), Air Force Weather Agency (AFWA, now 557th Weather Wing), Naval Research Laboratory (NRL), University of Oklahoma (OU), and the Federal Aviation Administration (FAA). The WRF system consists of fully compressible, Euler nonhydrostatic equations of motion, suitable for both weather prediction and research over a wide range of scales (Skamarock et al. 2008). The prognostic variables include three-dimensional wind and the perturbations of potential temperature, geopotential, surface pressure, and turbulent kinetic energy (TKE). The vertical coordinate system is a terrain-following, dry hydrostatic-pressure coordinate and the horizontal grid uses Arakawa C-grid staggering to gain better accuracy in high-resolution simulations. A detailed description of the basic equations and numerical schemes of the WRF-ARW can be found in Skamarock et al. (2008).

The WRF-ARW model is configured using a 3rd-order Runge-Kutta time-integration and a 6th-order spatial-discretization scheme for the advection terms. Additionally, a horizontal Smagorinsky 1st-order closure eddy coefficient option is used and vertical velocity damping is turned on, with a fixed damping depth of 5,000 m from the model top employed. A 6th-order numerical diffusion scheme is used, however up-gradient diffusion is prohibited. The model top is set at 50 hPa. The model domain configuration is a four-level, nested grid centered over the FL peninsula. The outermost, two middle, and innermost horizontal domain grids consist of grid spacings of 27-km (d01), 9-km (d02), 3-km (d03), and 1-km (d04), respectively. The outermost domains are chosen to cover the southeastern US and the surrounding Atlantic Ocean in order to capture synoptic dynamics that might influence the SB and convection, while the

innermost domain covers the area of interest for the case study: the FL peninsula and its surrounding waters. Figure 2.5 shows a detailed map of the domain area configurations. All four domains contain 62 vertical eta levels with 26 levels below 850 hPa. Table 2.1 gives a full list of the configurations used in the setup of the WRF-ARW model.

2.2.2 Configuration of Control Simulation

In order to have a baseline simulation for investigating the sensitivity of numerical simulations to the physical parameterization and ICs, a control (CTRL) WRF simulation is performed. The WRF model and domain setup described in Section 2.2.1. is used with a one-way domain feedback configuration. Physical parameterizations options used include the New Thompson microphysics, New Kain-Fritsch (KF) cumulus, MM5 Dudhia shortwave radiation, and Rapid Radiative Transfer Model (RRTM) longwave radiation, Yonsei University (YSU) planetary boundary layer, revised MM5 surface layer, and Unified Noah land surface model schemes. The microphysics and PBL schemes are applied to all four domains, while the cumulus schemes are only applied to the outermost d01 (27 km) and d02 (9 km) domains. A further description of the physics parameterization schemes is given in the next section. A summary of the CTRL parameterization options is given in Table 2.2. The WRF-ARW model initial and boundary conditions for the CTRL simulation are provided by the NCEP North American Mesoscale (NAM) Forecast System analysis at 12-km horizontal resolution from 0000 UTC 6 September 2012 to 1200 UTC 7 September 2012 at the interval of every 6 h. The model was then integrated in the one-way nested mode for 36 h from the start of the initialization period.

2.2.3 Configuration of Sensitivity Experiments to Physical Parameterizations

Physical parameterization is one of the most challenging aspects of numerical modeling, especially in the gray-zone grid scale, as the assumptions made in deriving the theory behind some of these parameterization processes may no longer be valid at this scale, such as that the fraction of the grid column that is occupied by active convection is small or that a large number of up- and downdrafts are found within the grid column (Grell and Freitas 2014). Within the last five years, gray-zone scale modeling at the operational level has become practically feasible, thus research into the effects of parameterization is a pressing area of study (Hong and Dudhia 2012). The WRF model has become an invaluable tool in this research area as it offers multiple physical parameterization options for key physical processes, such as planetary boundary layer (PBL), cumulus (CU), cloud microphysics (MP), longwave (LW) radiation, shortwave (SW) radiation, surface layer processes, and land surface model (LSM) interactions that can be combined to create various model configurations.

Three groups of sensitivity simulations are performed for the CU, MP, and PBL physics options within the WRF-ARW model. An additional simulation is also performed by changing the CTRL simulation from a one-way to a two-way domain feedback configuration (2WAY simulation) to address the effect of the smallest gray-zone grid (d04) to the larger gray-zone grid (d03) within the model. The same ICs and similar model configurations as specified in the CTRL are applied to these simulations. The specific physics parameterization simulations performed are listed in Table 2.2.

2.2.3.1 Overview of Cumulus Parameterization Schemes

Cumulus parameterization schemes are responsible for the cumulative subgrid effects of the redistribution of grid column moisture and temperature associated with updrafts and downdrafts, making clouds and convection precipitation, and the role of convection in drying and warming the atmosphere (Skamarock et al. 2008). Previous research has indicated that SB convection and precipitation output appear to be sensitive to the choice of CU parameterization (Cohen 2002, Evans et al. 2012), though many of these studies have been idealized case studies, for locations in the UK and Australia, and for grid sizes greater than 10 km. Thus, an investigation of CU parameterization effects to a real FL SB case in the gray-zone spacing is warranted. Four CU parameterization simulations (simulations annotated by CU in Table 2.2) are conducted and briefly described below.

The New Kain-Fritsch CU scheme (CTRL simulation) accounts for deep and shallow convection using a mass flux approach for moist updrafts and downdrafts and is programmed to eliminate CAPE (Skamarock et al. 2008). In this scheme, entrainment and detrainment rates only depend on the buoyancy of mixtures of clear and cloudy air and a parcel that is negatively buoyant at the LCL is allowed to form a cloud only if it is supported by grid scale upward motion (Kain 2004). The Grell-Freitas (GF) scheme (CU1_GF simulation) and Grell 3D (G3) scheme (CU2_G3 simulation) are multiclosure, multiparameter ensemble methods that have been improved from the original Grell-Devenyi (GD) CU scheme to be used on high-resolution simulations (Grell and Freitas 2014). The GF scheme is modified to smooth the transition to cloud-resolving scales by eliminating the assumption of small fractional area covered by convection as the

resolution increases, as proposed by Arakawa et al. (2004). The G3 scheme is distinguished from other CU schemes in that it allows subsidence effects to be spread to neighboring grids. The New Simplified Arakawa-Schubert (NSAS) scheme (CU3_NSAS simulation) is a deep and shallow convection scheme that uses a mass-flux parameterization that replaces a previous turbulent diffusion-based approach (Han and Pan 2011). Improvements were also made to the cloud-top selection, deep convection processes, and the turbulence diffusion in stratocumulus regions. The New Tiedtke (NT) scheme (CU4_NT simulation) accounts for both updrafts and downdrafts separately, and uses a bulk model for different types of convection (Tiedtke 1993).

2.2.3.2 Overview of Microphysics Parameterization Schemes

Microphysics parameterizations control the formation and dissipation of water vapor, cloud, and precipitation processes within the simulation (Skamarock et al. 2008). For gray-zone grid models, the effects of aerosols for cloud and ice nucleation, as well as how mixed-phase growth of hail or graupel in riming processes become more important factors (Hong and Dudia 2012). As the effects of MP schemes on SB convection is relatively sparse, this in an important area of research. Four MP parameterization simulations (simulations annotated by MP in Table 2.2) are conducted and briefly described below.

The New Thompson (CTRL simulation), Purdue Lin (MP1_Lin simulation), WRF Single-Moment 6-Class (WSM6, MP2_WSM6 simulation), and Morrison (MP3_Mor simulation) schemes are 6-class MP parameterizations that include mixing ratio predictions for water vapor, cloud water, rain, cloud ice, snow, and graupel

processes, while the Stony Brook University (SBU, MP4_SBU simulation) is 5-class MP scheme that neglects the graupel processes. The Thompson, Lin, WSM6, and SBU schemes are single-moment bulk parameterizations, though the Thompson scheme has a double-moment cloud ice process and includes rain and ice number concentrations (Thompson et al. 2004). The Morrison scheme is a two-moment bulk MP scheme that allows for a more robust treatment of the 6-class hydrometeors by specifying their number concentrations as well as their mixing ratios (Morrison et al. 2009). The SBU scheme predicts riming intensity to better account for mixed-phase processes (Lin and Colle 2011). The WSM6 scheme better represents mixed-phase particle fall speeds for snow and graupel particles than the simpler schemes that use only 3-class and 5-class hydrometeor specifications and is more suitable for cloud-resolving grids (Hong and Lim 2006). The Lin MP scheme includes ice sedimentation and time-split fall terms and is suitable for parallel computation and high-resolution simulations (Lin et al. 1983).

2.2.3.3 Overview of PBL Parameterization Schemes

One source of forecast inaccuracy in gray-zone grid scale models is the representation of lower-tropospheric thermodynamic and kinematic structures in the PBL – that portion of the lower troposphere directly affected by the earth's surface via exchanges of heat, momentum, and moisture (Cohen et al. 2015). In the WRF-ARW, the PBL parameterization schemes determine the vertical subgrid scale flux profiles (i.e., temperature, moisture, and horizontal momentum) within the well-mixed boundary and stable layer due to eddy transports (Skamarock et al. 2008). Several PBL parameterization studies for SB cases have been carried out with the last ten years in the

gray-zone (Srinivas et al. 2007; Challa 2009; Miao et al. 2009; Evans et al. 2012), but none have been conducted for cases over the FL peninsula. Five PBL parameterization simulations (simulations annotated by PBL in Table 2.2) are conducted and briefly described below. The surface layer and land surface model physics options are only changed from the CTRL settings (i.e., revised MM5 and Noah LSM, respectively) for the PBL simulations if the changes were specified by the PBL scheme designers for the optimal performance of the parameterization scheme in the WRF model.

The YSU PBL scheme (CTRL simulation) is a 1st-order nonlocal eddy-diffusivity turbulence closure scheme that explicitly represents entrainment processes at the top of the PBL (Hong et al. 2006). The Mellor-Yamada- Janjić (MYJ) PBL scheme (PBL1_MYJ simulation) is a local 1.5-order, level 2.5 closure scheme, that determines eddy diffusion coefficients from prognostically calculated TKE (Janjić 1994). The Monin-Obukhov Janjić Eta (MO-JE) surface layer scheme is used with the MYJ PBL scheme and is based on the modified Monin-Obukhov similarity theory. The Mellor-Yamada Nakanishi and Niino Level 3 (MYNN3) scheme (PBL2_MYNN3 simulation) is a local 2nd-order, level 3 TKE closure scheme whose expressions of stability and mixing length are based on the results of a LES rather than observations (Nakanishi and Niino 2006). The MYNN surface layer scheme is used in conjunction with the MYNN3 PBL scheme. The Asymmetrical Convection Model, version 2 (ACM2) scheme (PBL3_ACM2 simulation) is a hybrid local-nonlocal 1st-order closure PBL scheme where the representation of upward fluxes within the PBL are nonlocal interactions between the surface layer and each and every layer above, while downward fluxes are represented through local interactions with the underlying layers. This represents

convective plumes arising from diurnally heated surface layer, whereas downward fluxes are more gradual (Pleim 2007). The Pleim-Xiu (PX) surface layer and LSM are used in conjunction with the ACM2 PBL scheme instead of the CTRL's MM5 surface layer and Noah LSM options. The Quasi-Normal Scale Elimination (QNSE) scheme (PBL4_QNSE simulation) is a 1.5-order local closure that uses a TKE-prediction option and is intended to account for wave phenomena using spectral theory within stable boundary layers (Sukoriansky et al. 2005). The QNSE surface layer scheme is used in conjunction with the QNSE PBL scheme. The Grenier-Bretherton-McCaa (GBM) scheme (PBL5_GBM simulation) is a 1.5-order TKE local closure that depicts a PBL influenced by stratocumulus clouds through vertical variations in static stability profiles are driven by moist thermodynamics such as longwave radiation fluxes owing to the presence of these clouds (Grenier and Bretherton 2001).

2.2.4 Configuration of Sensitivity Experiments to Initial Conditions

NWPs are known to have difficulty in initiating, developing, and organizing convection owing to the small-scale nature of many of the features that act to initiate and maintain convection (Kain and Fritsch 1992; Stensrud et al. 2000). Thus, the atmospheric conditions specified in the model's ICs can make large differences in NWP forecasts. As mentioned in the description of the SB case study in Section 2.1, 5 September 2012 saw convective activity by the SB over the FL peninsula. At 0000 UTC 6 September 2012 (initialization time of CTRL simulation), remnants of convective activity were still occurring, simulations are conducted with initialization times prior to and after this time in order to observe how adding or removing these convective IC effects affect the WRF

simulation.

Five ICs simulations with different start times and initialization data are performed. First, a simulation is performed using the same initialization and ending times as the CTRL simulation (0000 UTC 6 September 2012 to 1200 UTC 7 September 2012), but using NCEP's Global Forecast System analysis (GFS-ANL) data at 0.5 degree (~28 km) horizontal resolution instead of the 12 km NAM data for the initialization data (IC1_GFS). Additionally, utilizing the same NAM data as the CTRL simulation, but varying the initialization start times, four other simulations are performed: IC2_0512, IC3_0518, IC4_0606, and IC5_0612. These simulations are run until 1200 UTC 7 September 2012, producing simulation durations ranging from 48 to 24 h. The specific IC simulations performed are listed in Table 2.3.
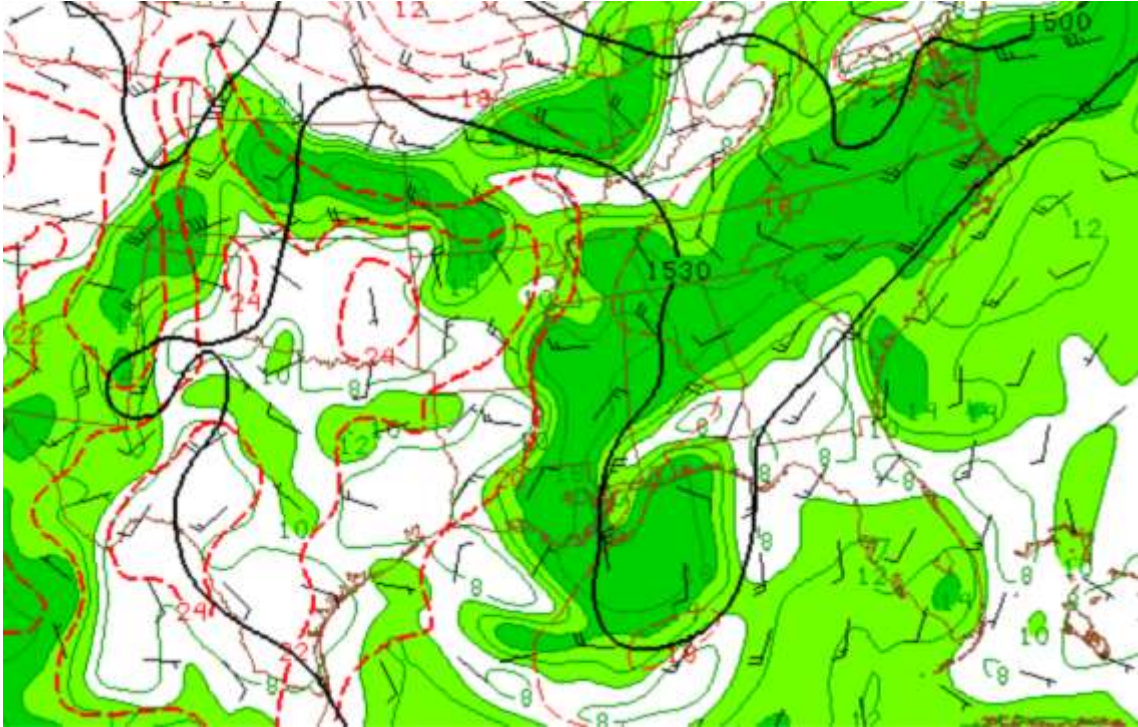
Figure 2.1 Upper air analysis at 1200 UTC 6 September 2012 for 850 hPa observations, geopotential heights (black contours, units every 30 gpm,), temperatures (red dashed contours, units every 2°C), and dew point temperatures (green contours, units every 2°C above 8°C, light green filled at 10 °C, dark green filled at 14 °C). Image courtesy of the National Oceanic Atmospheric Administration's (NOAA) Storm Prediction Center (SPC) [http://www.spc.noaa.gov/obswx/maps/].
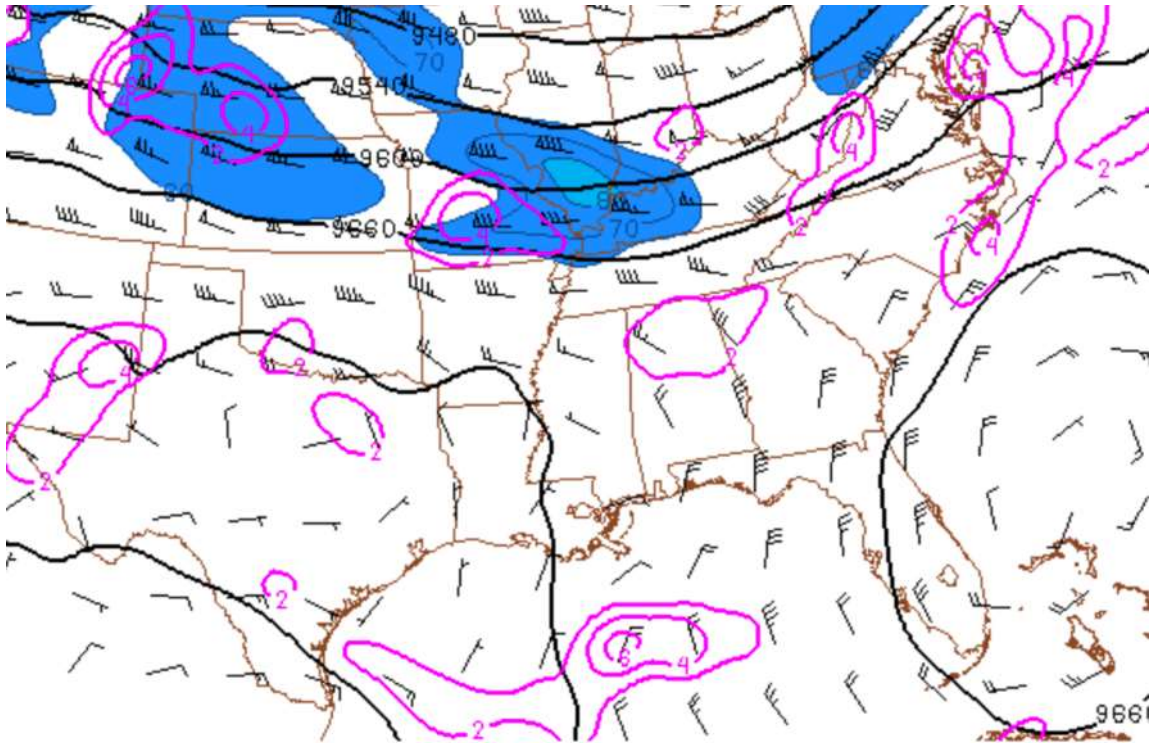
Figure 2.2 Upper air analysis at 1200 UTC 6 September 2012 for 300 hPa observations, geopotential heights (black contours, units every 60 gpm), divergence (pink contours, units every 10^{-5} s^{-1}), and isotachs (blue contours, units every 10 kts above 60 kts). Image courtesy of the National Oceanic Atmospheric Administration's (NOAA) Storm Prediction Center (SPC) [http://www.spc.noaa.gov/obswx/maps/].
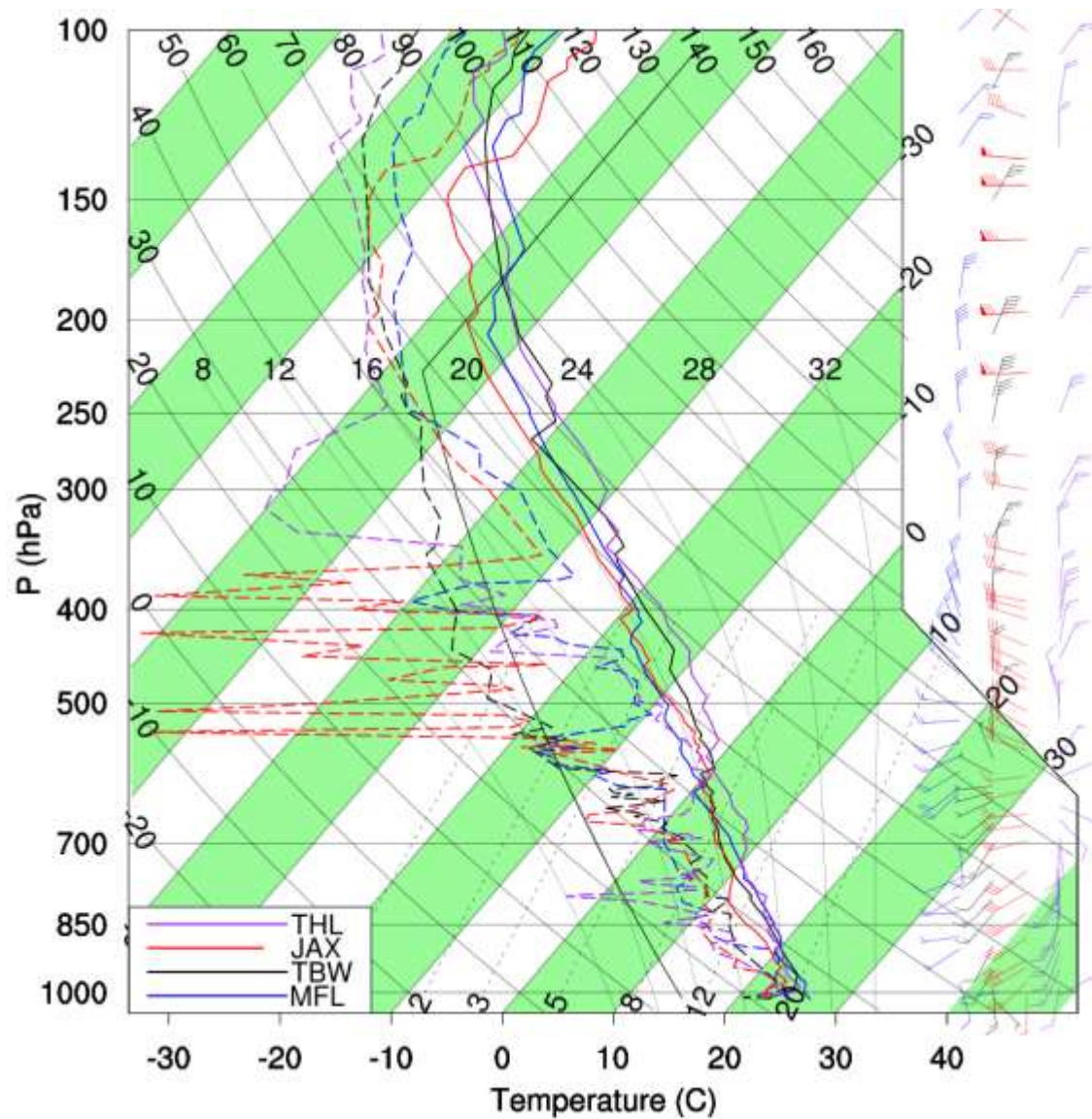
Figure 2.3 Observed soundings for four Florida stations: Tallahassee (TLH, purple line), Jacksonville (JAX, red line), Tampa Bay (TBW, black line), and Miami (MFL, blue line) at 1200 UTC on 6 September 2012. CAPE (units J kg^{-1}), CIN (units J kg^{-1}), LFC (units hPa), LCL (units hPa), and PW (units mm) values for each of the four stations are listed below the Skew-T.
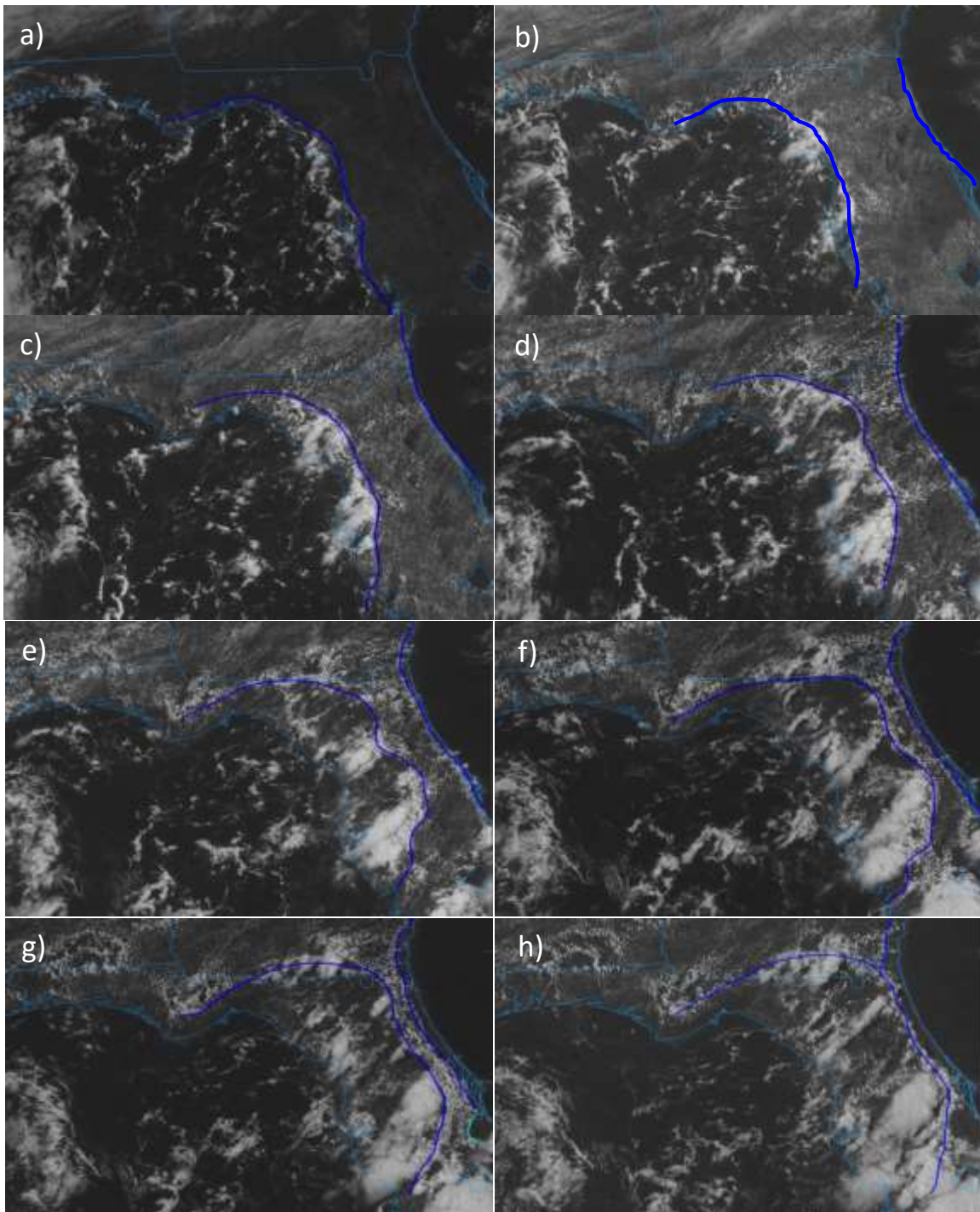
Figure 2.4 Geostationary Operational Environmental Satellite-East (GOES-E) visible satellite images of convective cloud cover over the Florida peninsula at a) 1401 UTC, b) 1515 UTC, c) 1601 UTC, d) 1745 UTC, e) 1831 UTC, f) 1931 UTC, g) 2001 UTC, and h) 2031 UTC 6 September 2012. Dark blues lines show the location of the west coast and east coast SBFs. Images courtesy of College of DuPage [http://www.cod.edu/] and Carl Jones [https://northflwx.wordpress.com/2012/10/01/florida-coast-to-coast-sea-breeze-convergence/].

Figure 2.5 WRF simulation domains for the 27-km grid (d01 – color map), 9-km grid (d02 – white box), 3-km grid (d03 – red box), and 1-km grid (d04 – blue box).

Table 2.1 WRF –ARW model simulation parameter settings.

Parameter	D01	D02	D03	D04
Horizontal dimensions	139x97	253x202	343x313	502x661
Horizontal resolution	27 km	9 km	3 km	1 km
Vertical resolution	62 levels with variable Δz (26 levels below 850 hPa) *			
Time integration	120s time step, 36 h duration*			
Boundary conditions	Damping depth over top 5,000 m*			
Lateral boundary interval	21600 sec*			
Nested feedback	One way with no smoothing*			
Vertical diffusion	2nd order diffusion*			
Time-integration	Runge-Kutta 3rd order*			
Numerical diffusion	6th-order, 0.12 nondimensional rate, prohibits up-gradient diffusion*			
Advection options	Positive-definite for moisture and scalars			
Eddy coefficient	Horizontal Smagorinsky 1st order closure*			

*Values are the same for all four grids

Table 2.2 List of WRF physics parameterization simulations. CTRL simulation is shaded in gray. Boxes highlighted in shades of orange indicate changes in physics options from the CTRL simulation.

Simulation	Feedback	Cumulus	Microphysics	PBL	Sfc Layer	Land Sfc
CTRL	1-way	KF	Thompson	YSU	MM5	Noah
2WAY	2-way	KF	Thompson	YSU	MM5	Noah
CU1_GF	1-way	GF	Thompson	YSU	MM5	Noah
CU2_G3	1-way	G3	Thompson	YSU	MM5	Noah
CU3_NSAS	1-way	NSAS	Thompson	YSU	MM5	Noah
CU4_NT	1-way	NT	Thompson	YSU	MM5	Noah
MP1_Lin	1-way	KF	Lin	YSU	MM5	Noah
MP2_WSM6	1-way	KF	WSM6	YSU	MM5	Noah
MP3_Mor	1-way	KF	Morrison	YSU	MM5	Noah
MP4_SBU	1-way	KF	SBU	YSU	MM5	Noah
PBL1_MYJ	1-way	KF	Thompson	MYJ	MO-JE	Noah
PBL2_MYNN3	1-way	KF	Thompson	MYNN3	MYNN	Noah
PBL3_ACM2	1-way	KF	Thompson	ACM2	PX	PX
PBL4_QNSE	1-way	KF	Thompson	QNSE	QNSE	Noah
PBL5_GBM	1-way	KF	Thompson	GBM	MM5	Noah

Table 2.3 List of WRF initial conditions simulations. CTRL simulation is shaded in gray. Boxes highlighted in shades of orange indicate changes in initial conditions from the CTRL simulation.

Simulation	IC Data	Initialized	CU	MP	PBL	Sfc Layer	Land Sfc
CTRL	NAM	06/00 UTC	KF	Thompson	YSU	MM5	Noah
IC1_GFS	GFS	06/00 UTC	KF	Thompson	YSU	MM5	Noah
IC2_0512	NAM	05/12 UTC	KF	Thompson	YSU	MM5	Noah
IC3_0518	NAM	05/18 UTC	KF	Thompson	YSU	MM5	Noah
IC4_0606	NAM	06/06 UTC	KF	Thompson	YSU	MM5	Noah
IC5_0612	NAM	06/12 UTC	KF	Thompson	YSU	MM5	Noah

CHAPTER 3

SIMULATION RESULTS AND SENSITIVITY TO PHYSICAL

PARAMETERIZATION AND INITIAL CONDITIONS

Numerical simulations are verified against upper air and surface conditions and

precipitation characteristics in order to verify the large-scale synoptic pattern and the SB

and CI timing and evolution. The WRF sensitivity experiments with various physical

parameterization schemes and initial conditions (P/IC) are each verified against

observational and analysis data to note changes from the CTRL simulation and also to

identify sensitivities to the parameterizations and ICs within the WRF model.

3.1 Verification Data and Methods

The WRF model outputs are compared to NCEP's 32-km horizontal grid

spacing/45-level vertical resolution North American Regional Reanalysis data (NARR,

Mesinger et al. 2005). As the NARR data are on a much coarser grid scale than the gray-

zone WRF simulations, the NARR data are only used to verify the upper air synoptic

wind and pressure fields in a subjective determination of the simulation's forecast skill.

The evaluation has also been done by comparing a time series of surface variables

from the model outputs with the surface observations. Specifically, the simulation results

are verified using surface parameters obtained from local aviation routine weather reports

(METARs) and aviation special weather reports (SPECIs) from 23 locations across the FL peninsula (see Figure 3.1). The 2-m temperature and humidity values and 10-m winds for the surface observations are compared to the model value from the model grid box that contains the location of the observation. The root-mean-square error (RMSE), which is defined as the square root of the mean of the squared differences between corresponding elements of the forecast value (f) and observation value (o) (Barnston 1992), are used to verify surface variables from the WRF simulations. The RMSEs are calculated for the 2-m temperature and dewpoint and 10-m wind speed using the following formula:

$$RMSE = \sqrt{\sum_{i=1}^{N} (f - o)^2 / N} \qquad\qquad (\,2.1\,)$$

where N is the total number of verification points for the forecast and observed values. RMSE values range from 0 to infinity, with lower values showing greater skill in the forecast. A subjective analysis of the simulation's forecast skill was also conducted using surface observation analysis plots.

The convection within the simulation determined by simulated precipitation amounts and dBZ values. An evaluation of subjective precipitation forecasts in determining the timing, location, and intensity of WRF-simulated convection was conducted, along with a quantitative precipitation forecasting (QPF) analysis utilizing NCEP's Stage IV data (Lin and Mitchell 2005) and the Climatology-Calibrated Precipitation Analysis (CCPA) data (Hou et al. 2014). The Stage IV precipitation analysis data are 4-km grid scale mosaics of regional multisensor (gauge, radar, and satellite data) analyses produced by the National Weather Service (NWS) River Forecast Centers (RFCs). CCPA data are Stage IV analyses products further adjusted based on Climate

Prediction Center (CPC) unified global daily gauge analysis through a linear regression

method.

In order to evaluate the QPFs, the Threat Score (TS), also known as a Critical

Success Index (CSI), and the Bias Score (BS) for the two innermost domains are

calculated. The values used to calculate these scores are given in a 2 x 2 contingency

table (Table 3.1). Four specific precipitation thresholds are used in the QPF statistics

calculations: 2.54, 6.35, 12.7, and 25.4 mm. Knowing information about the forecast area

(F), observed area (O), and the correctly forecasted "hits" (H), the TS seeks to answer

how well the forecast "hits" (H) correspond to the observed occurrences. The BS seeks to

answer how similar were the frequencies of "hit" forecasts and correct observations. The

TS and BS are mathematically defined as

$$TS = H/(O + F − H) \text{ and} \qquad\qquad (2.2)$$

$$BS = F/O. \qquad\qquad (2.3)$$

TS values range from 0 to 1, with 0 indicating no skill in the forecast. BS values range

from 0 to infinity, with a bias of less than one indicating a tendency to underforecast in

the forecast system, while a bias of greater than one indicates a tendency to overforecast.

The subjective analysis of convection compared locations and timing of the WRF-

simulated precipitation accumulations are also conducted with Stage IV and CCPA

analyses.

3.2 Verification of Control Simulation

The NARR data were used to verify the upper air synoptic features of the CTRL

simulation, as well as how the CTRL simulation predicted the diurnal heating and SB

effects. Results show that the CTRL simulation was able to capture the overall upper air

synoptic features over the southeast area of North America, as described in Chapter 2, to include the 850 hPa high over the Atlantic Ocean and low-pressure system over the western Gulf of Mexico, as well as the low pressure system over the Bahamas at the 300-hPa level. In terms of a quantitative analysis of the surface conditions, Table 3.2 shows RMSE values for the CTRL simulation surface variables (temperature, dewpoint, and wind speed). The CTRL RMSE values are less than 2°C for the temperature and dewpoint values and less than 1.5 ms^{-1} for wind speeds. With the relatively small RMSE values, it appears that the CTRL simulation does a relatively good job in forecasting the surface variables, with the largest errors seen in forecasting temperature values. Overall, this indicates that the model is well able to capture the synoptic situation and surface conditions of 6-7 September 2012.

3.2.1 Sea Breeze Verification

Figure 3.2 shows that about an hour after daybreak in the simulation (1230 UTC 6 September 2012, Figure 3.2a), diurnal heating of the land has started, and by 1530 UTC 6 September 2012 (Figure 3.2c), the entire FL coastal regions have reached surface temperatures exceeding those of the nearby coastal waters. This land-ocean temperature gradient leads to surface pressure decreases over the land and the turning of the land breeze into a SB. The SB circulations can be identified by the direction and speed changes of the observed and simulated near-surface wind fields.

The WRF-simulated gray-zone SB is initiated between 1405 and 1435 UTC 6 September 2012 on both sides of the peninsula (Figure 3.2d), which is similar to the SB initiation time in the surface observations and NARR data. The SBs reach an average

heights of 850 -1,000 m in the d03 and d04 CTRL simulations, as seen in the CTRL results listed in Table 3.3. The two SBs meet inland of the eastern coast of FL at 2120 UTC 6 September 2012 for the d03 simulation and at 2040 UTC for the d04 simulation (Table 3.3), slightly later than the merger time in the observations (2030 UTC 6 September 2012).

Overall, the gray-zone CTRL simulation does a relatively good job simulating the general features of the synoptic situation and the initiation and evolution of the FL SB on 6-7 September 2012. However, the d03 CTRL simulation has some issues with resolving the timing of the SB frontal merger, though improvements to the SB timing and strength are achieved in the smaller grid spacing and will be discussed further in Chapter 4.

3.2.2 Convective Initiation Verification

In looking at the QPF analysis, the TS and BS values for the d03 and d04 CTRL simulation results are given in Table 3.4. As seen by the relatively low TS values in both domains for all four precipitation thresholds, the gray-zone simulations are relatively poor at forecasting the correct intensities for the SB event, and the BS shows that the gray-zone simulations considerably underforecast the precipitation intensity events. However d04 performs slightly better than d03 in all the QPF threshold categories due to the overall increased spatial precipitation amounts that occur in the d04 compared to the d03 as seen in Figure 3.3.

Figures 3.3a and 3.3b compare the CTRL simulation accumulated precipitation to CCPA data from 1200 UTC 6 September 2012 to 0600 UTC 7 September 2012 (18-h accumulated precipitation totals) for domains d03 and d04, respectively. Both CTRL

simulation domains and the CCPA analysis observe relatively sparse areal coverage of rainfall along the west coast and northern FL, while distinct patterns of rainfall are observed along the east coast and central FL. In addition, an obvious lack of rainfall occurs northeast of Lake Okeechobee in both the CCPA analysis and the CTRL simulations, although the "rain shadow" is more pronounced in d03 (Figure 3.3a) than in d04 (Figure 3.3b). Meanwhile, a light rainfall occurs across the north-central and northeast portion of the FL peninsula in the d04 simulation (Figure 3.3b), while the d03 grid scale shows almost no precipitation in those areas (Figure 3.3a). Overall, the d04 simulation shows better ability to simulate the accurate locations of the convective precipitation than does the d03, though Figures 3.3c and 3.3d show that both CTRL gray-zone grid scales are relatively poor in forecasting the large spatial areas of high intensity precipitation accumulations (greater than 12.8 mm), though d03 has larger organized spatial areas of high intensity precipitation than does d04.

Figure 3.4 further compares the hourly timing and spatial locations of the d03 and d04 simulated precipitation for the CTRL simulation with Stage IV data. Simulated timing of the initial convection along the west coast of FL at 1400 UTC 6 September 2012 for an inland location just northeast of Waccasassa Bay (near station CGC in Figure 3.1) in d03 and d04 (Figures 3.4a and 3.4b) is concurrent with observations, however, the d03 fails to resolve the convection produced east of Waccasassa Bay. In contrast, with higher resolution, the d04 is able to capture the convection east of Waccasassa Bay (Figure 3.4b), but also overestimates the WCSB convection just north of Naples (APF in Figure 3.1). By 1800 UTC 6 September 2012, the d04 resolves the convection along the east coast of FL, while the d03 has no convection associated with the ECSB at this time

(Figures 3.4c and 3.4d). It is not until 1900 UTC 6 September 2012 that the d03 domain begins to resolve significant convection along the ECSB. At this time, we also see small convective cells that are not associated with the SBF in the central portion of the peninsula in d04 (Figure 3.4d) that are not seen in the d03 (Figure 3.4c).

In the d03 and d04 CTRL simulations, the SBFs collide and merge at 2120 and 2040 UTC 6 September 2012, respectively, and produce an enhanced convective squall line which is markedly similar to the Stage IV analysis convective pattern (Figure 3.4e and 3.4f). However, from 2230 UTC 6 September 2012 until 0200UTC 7 September 2012, the orientation of the convective in the d03 CTRL simulation becomes more north-to-south orientated, while the Stage IV analysis data clearly shows the convective line in southern FL maintaining a northeast-to-southwest orientation (Figure 3.4g). The convection produced in d04 shows greater ability to capture this northeast-to-southwest convective orientation (Figure 3.4h). Finally, the duration of the convection across the FL peninsula in the d03 and d04 simulation lasts until 0500 UTC 7 September 2012 (not shown), concurrent with the Stage IV and CCPA analyses.

In summary, the CTRL simulation in both gray-zone grid spacings is able to capture the overall spatial locations and timing of the convective mesoscale systems (MCSs) that occurred for the 6-7 September 2012 SB event reasonably well. However, the intensities of the WRF-simulated convective precipitation are overall much weaker for the gray-zone simulations as compared to CCPA and Stage IV analysis convective precipitation intensities in subjective and QPF analyses. The timing and overall spatial locations of the CI is captured better in d04 than d03, and the d04 simulation is able to more accurately resolve the orientation of the convection after the SBF merger into the

squall line. D03, however, is better able to produce convective cells that are slightly

larger and more convectively organized than in the d04 results.

<u>3.3 Sensitivity of Simulations to Parameterizations and Initial Conditions</u>

All of the P/IC simulations were able to successfully resolve the overall synoptic

features of the 6-7 September 2012 SB case. The P/IC simulations were also all able to

resolve the SBs, though differences in SB timing and intensity are seen among the

different simulations. Furthermore, the P/IC simulations are able to produce the SB

convection, though differences in the timing, spatial locations, and intensity of the SB

convection varied among the various simulations as well, with the simulated SB

convection showing the most sensitivity to the PBL schemes and ICs.

3.3.1 Sea Breeze Sensitivities

Table 3.2 shows the results of the various P/IC simulations in terms of their

RMSEs for surface variables (temperature, dewpoint, and wind speed). All the P/IC

simulations have fairly small RMSE values, similar to the CTRL simulation, indicating

that all the simulations were able to achieve relatively good forecast results of surface

variables. The results also showed most simulations had improvements in forecasting the

surface variables for d04 compared to d03, with the exception of wind speed, which

showed an averaged decreased skill in forecasting at the higher resolution. Boldface and

gray italics in Table 3.2 indicate the best and worst simulations in terms of RMSE values

(i.e., top and bottom 10% of RMSE values). As can be seen in Table 3.2, overall, the

PBL3_ACM2 and the CU4_NT simulations are the best simulations in terms of RMSE,

while the IC5_0612 and PBL4_QNSE simulations are the worst. In addition, the largest

range of best and worst forecasts for surface variables in terms of RMSE values is seen in

the PBL and IC simulations, which indicate greater sensitivity of the surface parameters

to the chosen PBL parameterizations and ICs. All the P/IC simulations have a small range

of RMSE values for the surface variables, so we expect all the simulations to see a

production of a SB due to similar surface variable values.

In terms of diurnal heating of the land surface, all the P/IC simulations began

surface sensible heating at 1130 – 1200 UTC 6 September 2012, and by 1430-1500 UTC

6 September 2012, the coastal surface temperatures are exceeding those of the nearby

coastal waters. The PBL and IC simulations showed the most sensitivity in the speed,

timing, and the spatial structure of the sensible heating of the land surface. Figure 3.5

shows surface temperatures for four of the PBL simulations at 1500 UTC 6 September

2012. All four of these simulations demonstrate significant differences in the areas of

maximum heating, such as PBL3_ACM2 (Figure 3.5c) heating urban areas heating much

faster than other simulations, but the rest of the land surfaces much slower. These large

differences in location and timing of the sensible surface heating led to more significant

differences in SB initiation in the PBL and IC simulations. Table 3.3 shows the SB

initiation timing differences among the P/IC simulations.

In almost all the d03 and d04 P/IC simulations, the WCSB is initiated at 1400

UTC and the ECSB at 1430 UTC 6 September 2012, however, there are significant

differences in the SB initiation timing in the PBL and IC simulations. The PBL4_QNSE

and PBL5_GBM simulations both initiated the ECSB 30 min earlier than observations. In

addition, the PBL3_ACM2, IC4_0606, and IC5_0612 simulations initiated one or both of

the SBs 30 minu later than observations. This sensitivity to the PBL and IC simulations is also seen in the variation of the SB depths, where the SB depth varies greatly for these simulations as compared to the MP and CU simulations. The mergers of the SBs for the CU and MP simulations also show only a slight difference from the CTRL and with little internal variation of merger times. In contrast, the PBL and IC simulations show large differences in SB merger timing ranging from 20 min earlier to 2 h later than observations. Finally, the SB merger time and SB depth is also show to be sensitive to grid spacing, as the SB depth increases and initiation time gets more accurate with greater gray-zone resolution. Overall, the best simulation for resolving the timing of the SB in both grid spacings is the 2WAY simulation, which is due to the effects of the higher resolution being fed back up to the coarser resolution.

3.3.2 Convective Initiation Sensitivities

Table 3.5 shows the CI timing offset for the P/IC simulations compared observations. None of the P/IC simulations were able to capture the exact timing of the SB CI, though the PBL1_MYJ simulation showed the best results in capturing the timing of the simulated CI in both gray-zone grid spacings. The PBL4_QNSE and IC2_0518 simulations are the worst in terms of correctly forecasting the times of the SB CI, with the IC2_0518 simulation initiating the convection too soon, while the PBL4_QNSE simulation initiates the convection too late. All simulations shows sensitivity to the timing of the CI, however the PBL and IC simulations see the most variability in terms of CI start times as compared to the CTRL simulations. Improvements from d03 to d04 for CI timing are seen for all P/IC simulations as well.

Table 3.5 also shows the QPF results of the P/IC simulations to the CCPA and Stage IV analyses data in terms of the average Threat and Bias scores for the four precipitation thresholds (annotated in Section 3.1). As seen by the relatively low TS scores, all the P/IC simulations are relatively poor in forecasting the correct intensities for the SB event in both gray-zone grid spacings, while the BS shows that all the P/IC simulations are still underforecasting the intensity of the precipitation events, with the exception of the PBL4_QNSE simulation. Improvements in forecasting precipitation intensities with the higher resolution grid scale (d04) are once again shown for all simulations. The top and bottom 10% of simulations in terms of skill scores are chosen as our best and worst forecasts, respectively. The PBL4_QNSE and MP3_Mor simulations showed the greatest skill in correcting forecasting the intensities of the two gray-zones' SB convection, while the IC2_0512 and PBL2_MYNN3 simulations showed the worst skill. The PBL simulations once again showed the largest range in Threat Scores, indicating a greater sensitivity of precipitation intensity to the PBL simulations.

As with the convective intensities, differences in spatial coverage of the SB precipitation accumulations are seen for all the P/IC simulations. A comparison of the diversity of the convective precipitation spatial coverage and intensity for 8 P/IC simulations (2 CU, 2 MP, 2 IC, and 2 PBL simulations) with the CCPA precipitation accumulations are given in Figure 3.6. The largest diversity of convective locations and intensity are seen in the PBL simulations, though sensitivity to location and intensity of convection is seen in all P/IC simulations. Furthermore, there is slightly better accuracy in the spatial coverage of precipitation in the d04 simulations as compared to the d03 results (not shown) due to the higher resolution's tendency to produce smaller, more

numerous convective cells.

3.4 Summary of P/IC Numerical Simulation Results

None of the P/IC simulations was the best at overall forecasting the correct timing, intensity, and spatial locations of the SBs and their associated convection. However, based on the subjective and quantitative results of each simulation's ability to resolve the location, timing, and intensity of the SBs and the CI, the 2WAY and PBL1_MYJ simulations perform the best overall in the gray-zone grid spacing for our case study. However, as the 2WAY simulation has information and effects of the innermost domain fed back upon the coarser parent grids, thus impacting the numerical results, the PBL1_MYJ scheme is used as the "best" simulation for further analysis of differences in model output between the two gray-zone grid spacings (d03 and d04) in Chapter 4.

3.4.1 Sensitivity to Physical Parameterizations

The timing and evolution of the SB showed little to no sensitivity to the CU and MP parameterizations, as seen in the lack of diversity in the SB initiation timing and frontal depths amongst the CU and MP simulation members. This is expected as the CU and MP parameterizations mostly effect how the model handles convection and precipitation processes, not boundary layer interactions that produce the SB. In contrast, the timing and strength of the SB is strongly sensitive to the PBL parameterizations, as seen in the large differences for the PBL simulations' SB initiation/merger times and depths. This sensitivity to the PBL parameterizations is partly due to the differences in

how the PBL and associated LSM schemes determine the land-surface sensible heating and boundary layer vertical fluxes, as seen with the PBL schemes' differences in handling surface temperature (Figure 3.5) and SB initiation timing (Table 3.3). As the boundary layer heats up at different times and rates in the PBL simulations, the SB is also initiated at different times and various strengths.

The timing, intensity, and location of the SB CI shows slight sensitivity to the CU and MP parameterizations, as seen in the differences in threat scores, CI timing, and precipitation accumulations given in Table 3.5 and Figure 3.6 for these physical parameterizations. Two simulations with anomalous precipitation intensities are found within the CU and MP simulations (as seen in TS and BS values in Table 3.5): the CU2_G3 (Figure 3.6b) and MP3_Mor (Figure 3.6d). The Morrison MP scheme is the only MP scheme tested that includes a 2-moment scheme which specifies the hydrometeor concentration numbers, which seems to aid convection in our case study. The G3 CU scheme allows for subsidence effects to neighboring grids, which may account for the ability of the model to produce more intense convective cells in the simulation due to a decrease in numerous updrafts.

The SB CI also showed sensitivity to the PBL parameterizations as well, as seen in the large variability in the PBL threat scores, CI timing, and spatial locations (Table 3.5 and Figures 3.6) This large sensitivity is due, in part, to the fact that the PBL schemes greatly affected the SB timing and development as described in Section 3.3.1., which in turn impacted the timing and evolution of the CI along the SBFs. This can be seen in the differences between the PBL2_MYNN3 and PBL4_QNSE simulations (Figures 3.5b, 3.5d, 3.6h, and 3.6i). The PBL4_QNSE simulation shows a much warmer land surface,

which leads to much stronger SBFs and more intense convective precipitation, while the PBL2_MYNN3 simulation has a cooler land surface in comparison, producing weaker SBFs and weaker CI.

3.4.2 Sensitivity to Initial Conditions

The FL SB initiation timing and strength is slightly sensitive to the ICs. The simulations with the latest initialization times (0600 UTC and 1200 UTC 6 September 2012) show the greatest variability in SB initiation timing, however, these sensitivities could partly be due to their shorter spin-up time (2-8 h) prior to SB initiation as compared to the other IC simulations ($\geq$14 h). The initiation time, locations of, and intensity of the SB CI is also sensitive to the ICs, as seen in Figure 3.6 and Table 3.5. As the IC2_0512 and IC3_0518 simulations were able to simulate the 5 September 2012 convective precipitation at the beginning of their simulation periods, these simulations had added effects of a moister low-level atmosphere within the simulations. This is seen in the simulations increased soil moisture values (0.1-0.2 m/m^3 higher than the CTRL) and surface water vapor mixing ratios (1-2 g/kg higher than the CTRL) at 0600 UTC 6 September 2012 (not shown). This increased low-level moisture led to a saturated convective boundary layer and earlier CI due to decreased entrainment effects (Baker et al. 2001). The IC1_GFS simulation is noticeable similar to the CTRL simulation in terms of timing and intensity of the SB, which shows that the SB and CI are less sensitive to initialization data. However, as the NAM and GFS data are produced by the same agency and use similar processes in their data assimilation, the lack of sensitivity shown in the model could be due to the lack of diversity in the two ICs data sources.

3.4.3 Sensitivity to Gray-Zone Grid Scale

The timing of the SB initiation appears not to be sensitive to the grid spacing, however, the intensity and evolution of the SB (as seen in SB depth and timing of the SBFs' merger) is sensitive to the grid spacing as seen in the range of SB depth and initiation times in Table 3.3. Moreover, consistent improvements are made to the SB CI timing and spatial locations in the higher gray-zone grid resolution (d04), as seen in the TS values and CI timing offset of d03 and d04 in Table 3.5. However, improvements to the intensity of the SB convective cells and precipitation output for the higher resolution grid is mixed as seen in the bias score values for the two gray-zone grids (Table 3.5) and the comparison of the Figures 3.3c and 3.3d for the CTRL simulation. As the largest consistent improvement in simulating the SB and its CI in terms of timing, intensity, spatial location is seen with the variable gray-zone grid spacing, further analysis of the differences of the SBs and their CI and evolution between the two gray-zone grid scales is conducted to determine the factors for the improved forecasting CI skill due to increased grid zone resolution within the WRF-ARW model.
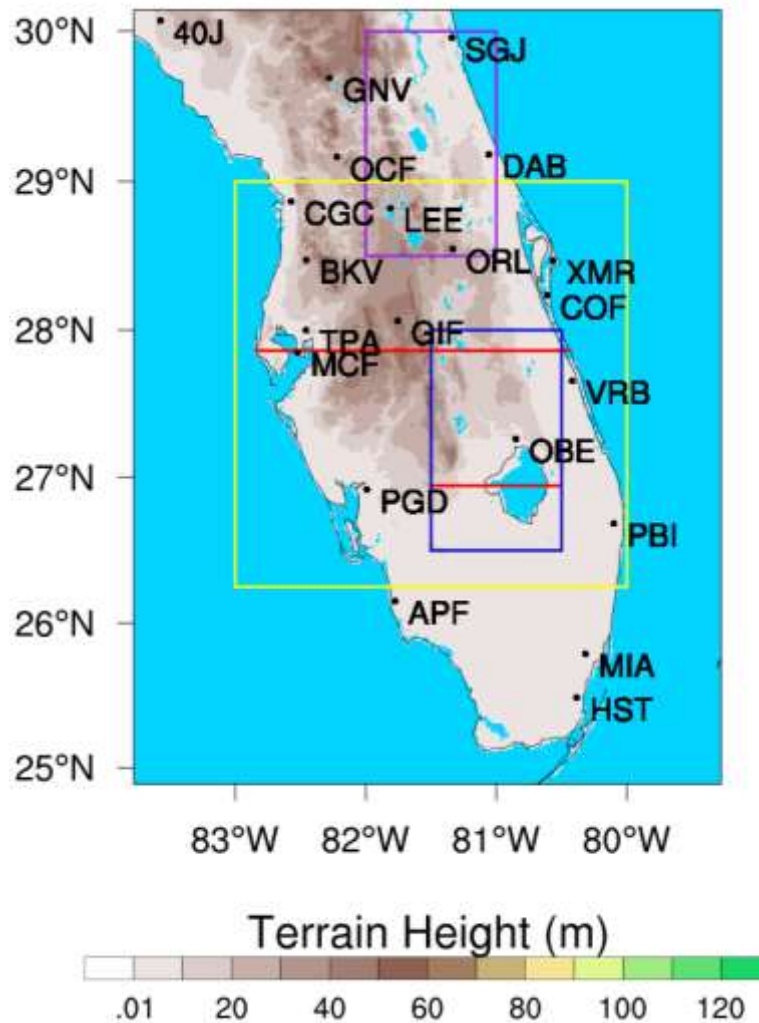
Figure 3.1 Map showing simulation terrain heights and water body locations for this study. Red lines indicate the locations of the vertical cross sections cut west-to-east through MacDill, Air Force Base (MCF, northernmost) and Lake Okeechobee (OBE, southernmost). The colored boxes indicate areas used later in the study for a zoomed-in analysis. The locations of the 23 observing stations used to aid in the verification of the WRF simulations are also plotted.

Table 3.1 Contingency table illustrating the counts used in verification statistics of dichotomous (e.g., Yes/No) forecasts and observations.

Forecast	Observed		
	Yes	No	Sum
Yes	Hits (H)	False alarms	All forecasted (F)
No	Misses	Correct rejections	No forecasted (N-F)
Sum	All observed (O)	No observed (N-O)	Total (N)

Table 3.2 Summary of P/IC simulations' RMSE scores for forecast performance skill of surface variables (temperature, dewpoint, and wind speed) for d03 and d04. "Best" RMSE forecasts are in boldface and "worst" RMSE forecasts in gray italic (see Section 3.3.1 for definition of best and worst).

Simulation	RMSE Temp (°C)		RMSE Dewpoint (°C)		RMSE Wind (ms^{-1})	
	D03	D04	D03	D04	D03	D04
CTRL	2.02	1.95	**1.34**	1.40	1.42	1.41
2WAY	**1.86**	1.95	1.38	1.39	1.41	1.42
CU1_GF	1.91	1.90	1.41	1.38	1.39	1.43
CU2_G3	1.91	1.87	1.40	1.38	1.40	1.41
CU3_NSAS	1.88	1.92	1.38	1.41	1.44	1.46
CU4_NT	1.88	**1.83**	1.36	1.37	1.43	1.44
MP1_Lin	1.95	1.91	1.41	1.39	1.40	1.39
MP2_WSM6	1.96	1.92	1.43	1.39	1.40	1.40
MP3_Mor	2.00	1.97	1.42	1.39	1.40	**1.38**
MP4_SBU	2.03	2.00	1.41	1.38	1.39	1.42
PBL1_MYJ	1.98	1.94	**1.34**	**1.32**	1.52	*1.63*
PBL2_MYNN3	*2.14*	1.99	1.47	1.39	1.38	1.47
PBL3_ACM2	**1.83**	**1.76**	**1.31**	**1.24**	1.41	1.41
PBL4_QNSE	1.94	1.90	1.43	1.41	*1.68*	*1.74*
PBL5_GBM	1.99	1.91	**1.34**	1.35	*1.58*	1.58
IC1_GFS	2.00	1.95	1.52	1.40	**1.34**	1.41
IC2_0512	1.94	1.93	*1.56*	1.47	1.35	**1.38**
IC3_0518	1.98	1.98	1.52	1.44	1.40	1.45
IC4_0606	1.96	*2.00*	1.55	*1.52*	**1.30**	1.41
IC5_0612	*2.07*	*2.03*	*1.64*	*1.58*	1.41	1.48
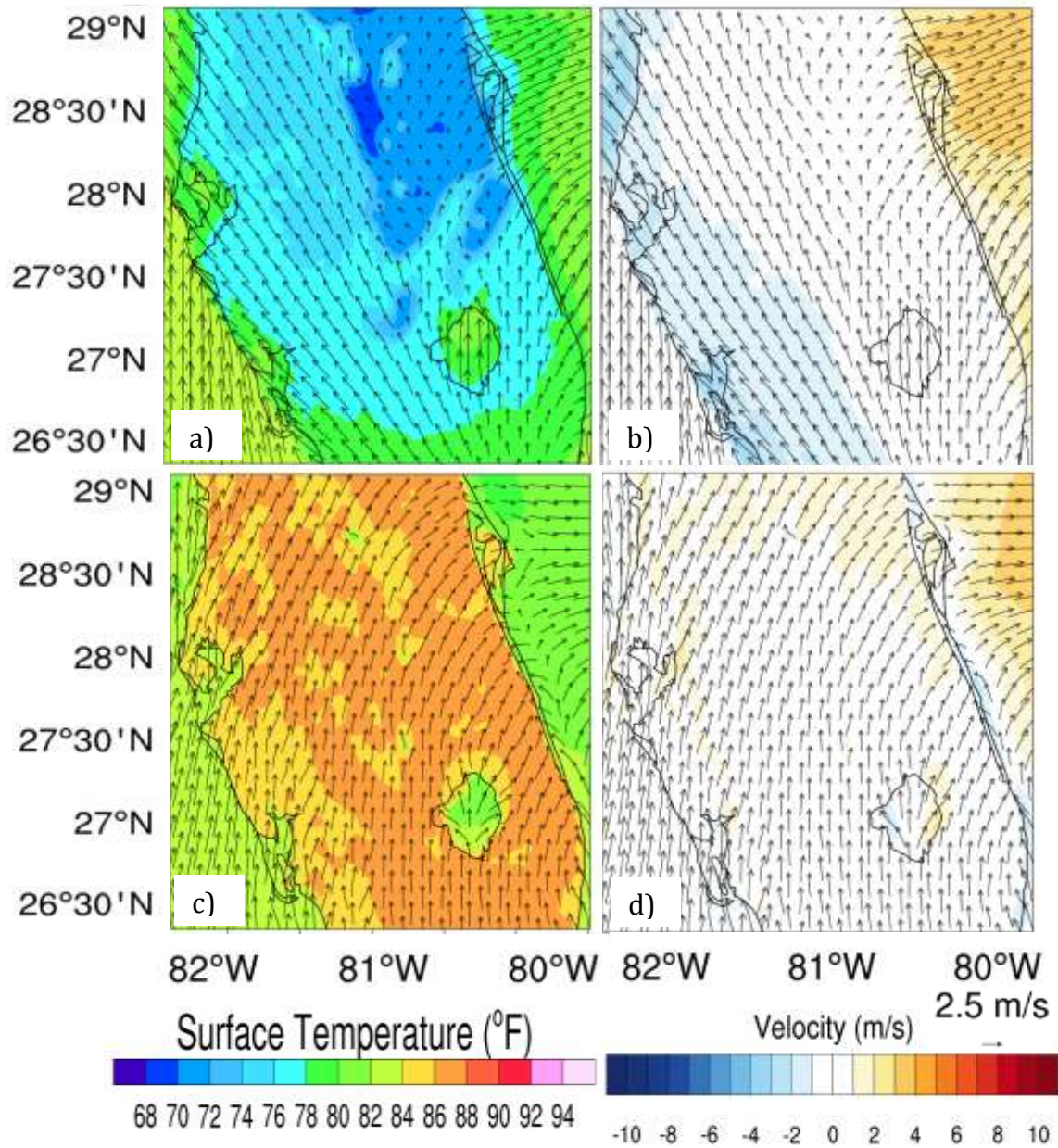
Figure 3.2 D03 CTRL simulation surface temperature (color, units every 2°F) and total surface wind (black arrows, reference vector 2.5 m s^{-1}) for a zoomed-in region of d03 (blue box in Figure 3.1) at: a) 1230 UTC and c) 1430 UTC 6 September 2012. D03 CTRL simulation zonal (u-component) winds (color: red easterly, blue westerly, units m s^{-1}) and total wind (black arrows, unit reference vector 2.5 m s^{-1}) for same region as a) and c) at: b) 1400 UTC and d) 1500 UTC 6 September 2012.

Table 3.3 Summary of P/IC simulation SB CI timing errors (min), maximum SB depth (m), and SB merger time (UTC) for d03 and d04. Zero offset on SB initiation timing is indicated by a green checkmark, blue indicates premature SB formation and red indicates delayed SB formation, as compared to observational data.

| Simulation | Initiation Timing Offset (min) | | | | | | Average SBF Depth (m) | | | |
| | WCSB | | ECSB | | SB Merger | | WCSB | | ECSB | |
	D03	D04	D03	D04	D03	D04	D03	D04	D03	D04
CTRL	✓	✓	✓	✓	+50	+10	950	1000	850	900
2WAY	✓	✓	✓	✓	+10	+10	1000	1000	850	850
CU1	✓	✓	✓	✓	+50	+10	850	950	800	850
CU2	✓	✓	✓	✓	+50	✓	850	950	800	850
CU3	✓	✓	✓	✓	+50	-10	850	950	800	850
CU4	✓	✓	✓	✓	+60	-20	850	950	800	850
MP1	✓	✓	✓	✓	+60	+20	850	950	800	850
MP2	✓	✓	✓	✓	+70	+10	850	950	800	850
MP3	✓	✓	✓	✓	+70	+50	850	950	800	850
MP4	✓	✓	✓	✓	+70	+30	850	950	850	950
PBL1	✓	✓	✓	✓	+50	✓	900	1000	850	950
PBL2	✓	✓	✓	✓	+120	+40	1000	1100	850	900
PBL3	+30	+30	+30	+30	+160	+90	750	900	700	850
PBL4	✓	✓	-30	-30	+60	+30	1150	1250	1000	1100
PBL5	✓	✓	-30	-30	+50	-20	950	1050	850	900
IC1	✓	✓	✓	✓	+50	+20	850	1000	800	900
IC2	✓	✓	-30	-30	+30	✓	900	1000	800	900
IC3	✓	✓	-30	-30	+40	+10	850	1000	800	950
IC4	✓	✓	+30	+30	+90	+30	950	1000	850	900
IC5	+30	+30	✓	✓	+90	+20	950	1000	850	900

Table 3.4 Threat and Bias Score values for four precipitation thresholds over an 18-h forecast period (1200 UTC 6 September 2012 to 0600 UTC 7 September 2012) for the CTRL simulation.

| Domain | Threat Score (TS) | | | | Bias Score (BS) | | | |
| | Precipitation Threshold (mm) | | | | Precipitation Threshold (mm) | | | |
	2.54	6.35	12.7	25.4	2.54	6.35	12.7	25.4
D03	0.12	0.10	0.08	0.00	0.12	0.11	0.12	0.14
D04	0.28	0.19	0.15	0.04	0.26	0.20	0.17	0.23
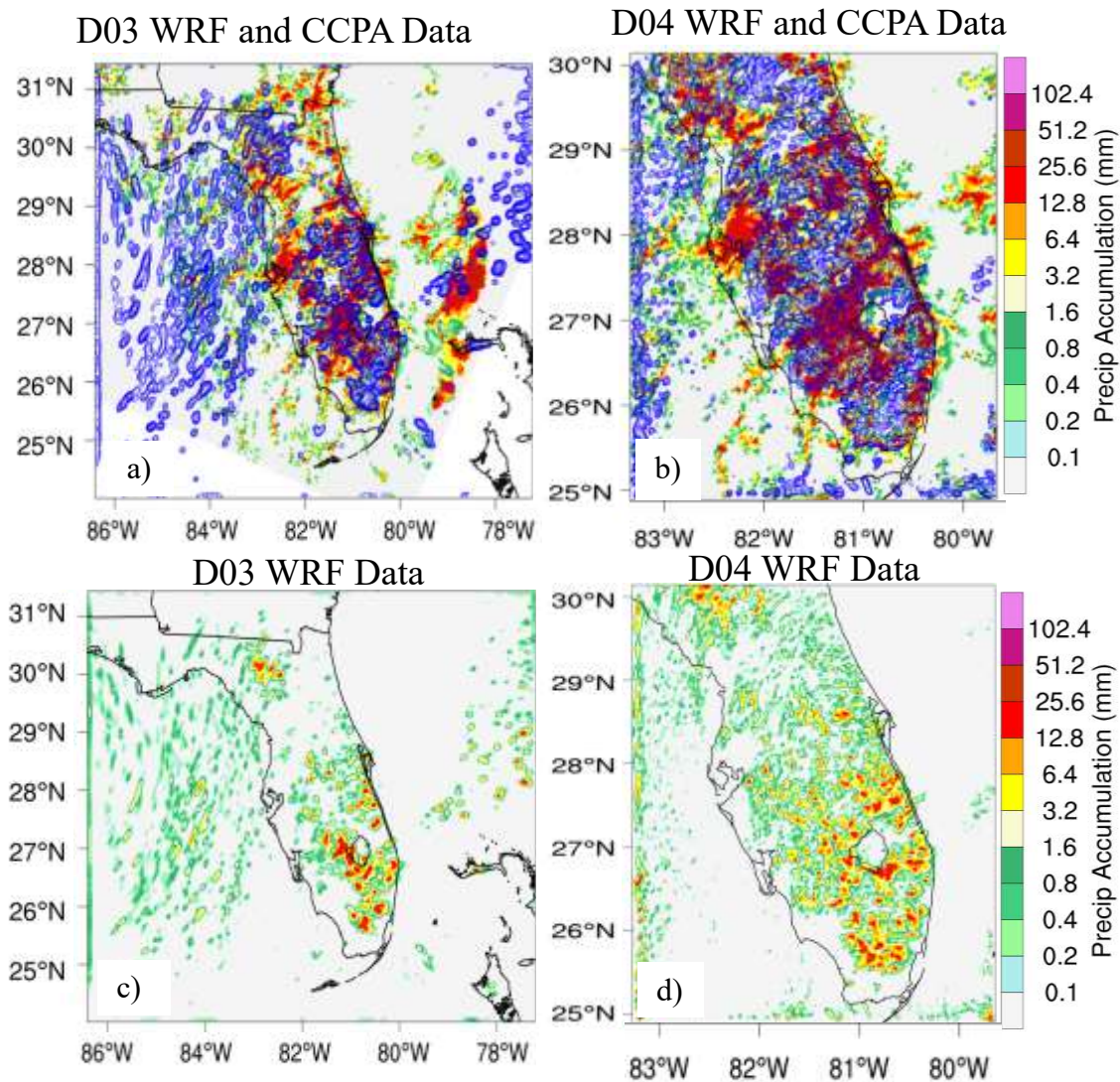
Figure 3.3 18-h rainfall accumulation totals from 1200 UTC 6 September 2012 to 0600 UTC 7 September 2012 for a) d03 CTRL simulation precipitation accumulation totals (blue contours, units mm h^{-1}) and CCPA data (color, units mm h^{-1}). Panel b) is the same as a) but for d04 CTRL simulation. CTRL simulation precipitation accumulation totals (color, units mm h^{-1}) for c) d03 and d) d04 for the same times as a) and b).
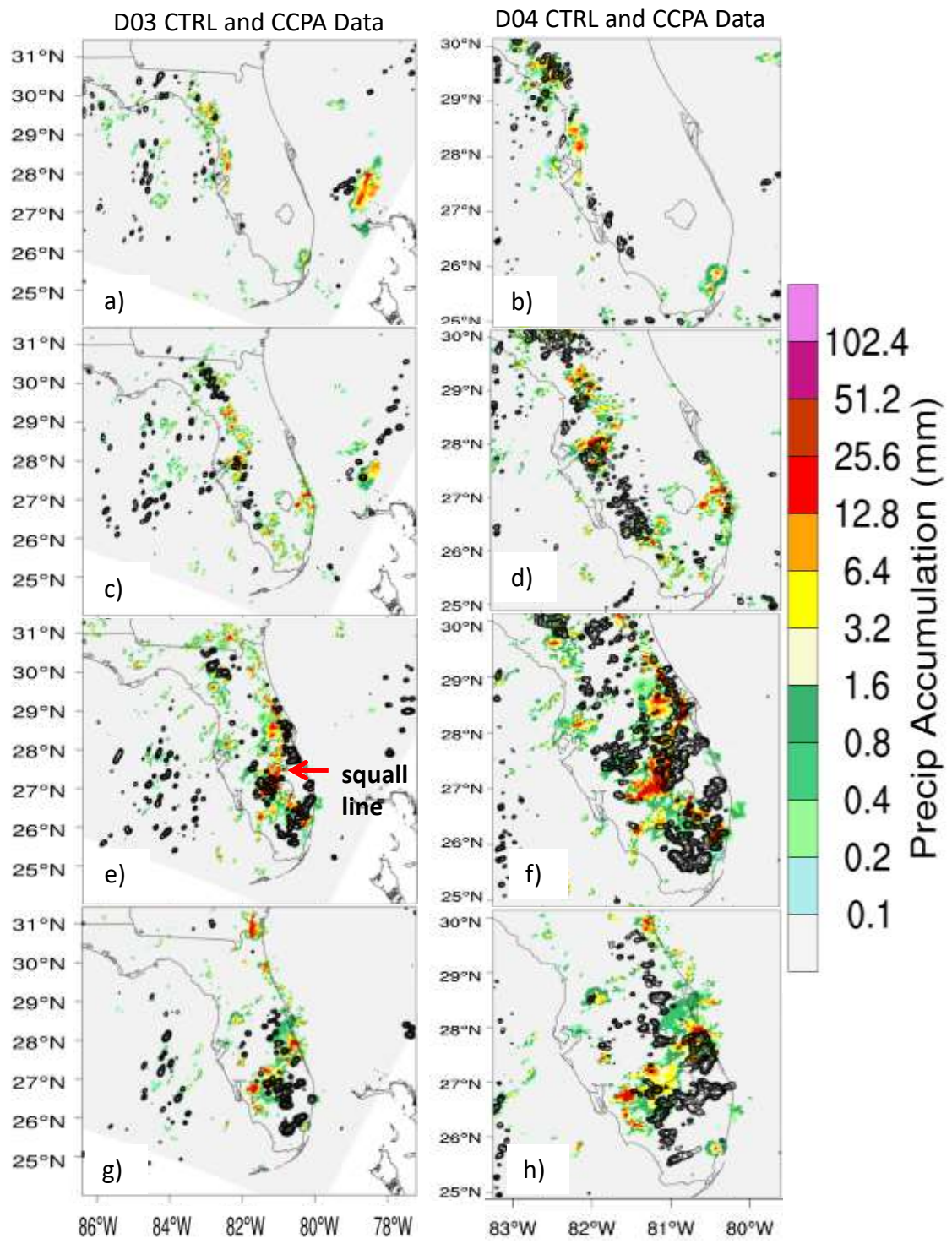
Figure 3.4 Stage IV precipitation accumulation (color, units mm h^{-1}) and d03 (left column) and d04 (right column) CTRL simulation precipitation accumulation (black contours, units mm h^{-1}) at: a-b) 1400 UTC, c-d) 1800 UTC, d-f) 2100 UTC, and g-h) 2300 UTC 6 September 2012.
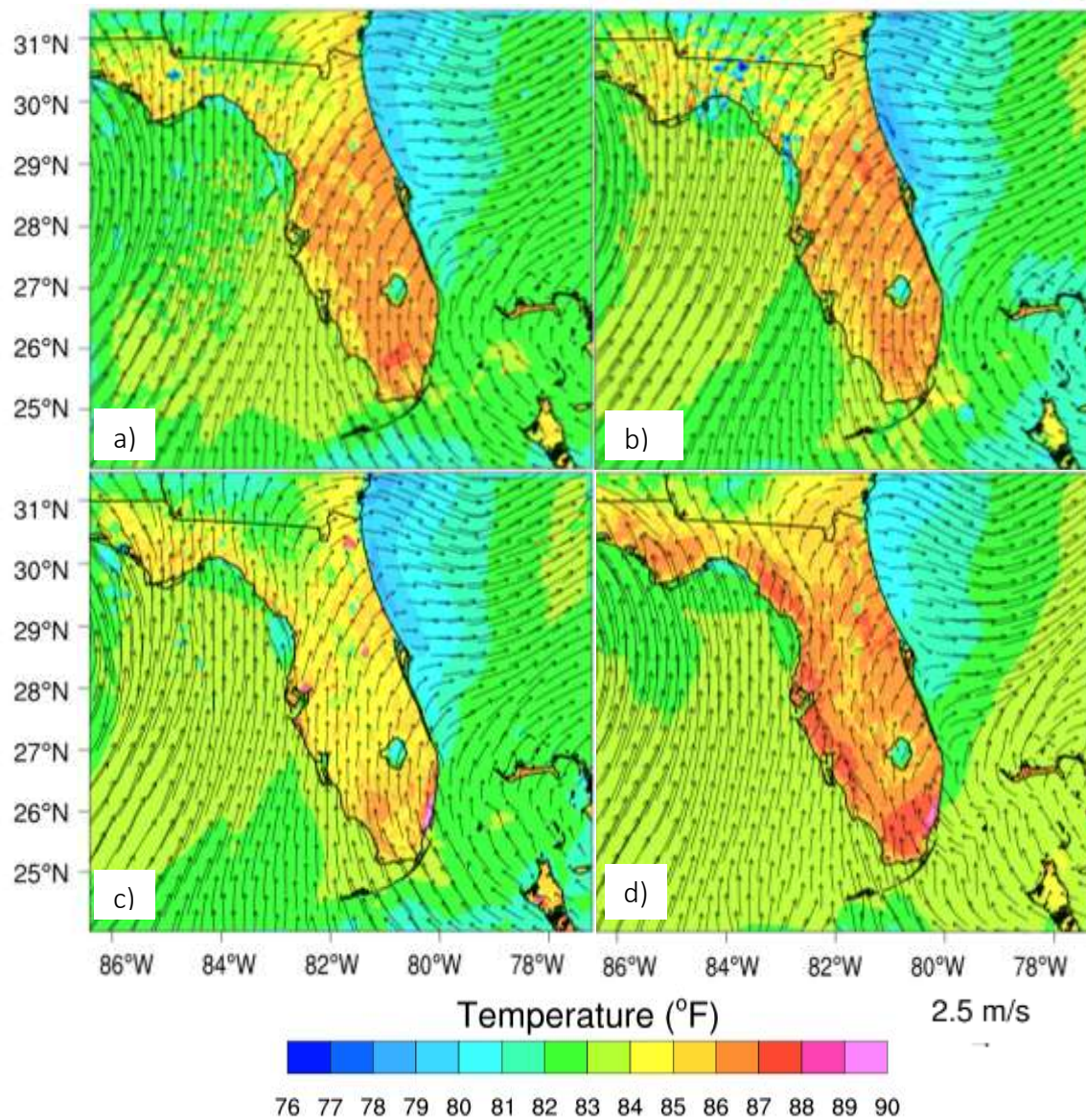
Figure 3.5 D03 surface temperature (color, units °F) and total wind (black arrows, unit reference vector 2.5 m s^{-1}) for a) CTRL, b) PBL2_MYNN3, c) PBL3_ACM2, and d) PBL4_QNSE simulations at 1530 UTC 6 September 2012.

Table 3.5 Summary of WRF simulation average Threat Score, Bias Scores, and SB CI timing errors (min) for d03 and d04. "Best" RMSE forecasts are in boldface and "worst" RMSE forecasts in gray italic (see Section 3.3.2 for definition of best and worst). Zero offset on SB CI timing is indicated by a green checkmark, blue indicates premature CI and red indicates delayed CI, as compared to Stage IV analysis data.

| Simulation | Avg Threat Score | | Avg Bias Score | | Timing Offset (min) | | | | | |
| | | | | | WCSB CI | | ECSB CI | | End of CI | |
	D03	D04	D03	D04	D03	D04	D03	D04	D03	D04
CTRL	0.08	0.17	0.12	0.22	-120	-60	+60	✓	✓	✓
2WAY	**0.15**	0.21	0.18	0.28	-120	-120	✓	✓	✓	✓
CU1_GF	0.13	0.23	0.42	0.34	+60	-60	+60	-60	+60	✓
CU2_G3	0.12	0.24	**0.75**	0.28	-60	-60	+60	✓	+240	+120
CU3_NSAS	0.14	0.26	0.33	0.48	-60	-60	+60	✓	+120	+60
CU4_NT	0.14	0.26	0.22	0.39	-60	-60	+60	-60	✓	✓
MP1_Lin	0.10	0.22	0.19	0.47	-60	+60	+60	-60	+60	+180
MP2_WSM6	0.10	0.20	0.25	0.29	-120	-60	+60	-60	+60	+60
MP3_Mor	0.14	**0.27**	0.31	**0.60**	-60	-60	+60	✓	✓	+120
MP4_SBU	0.09	0.19	0.19	0.27	-180	-120	+60	✓	+120	+120
PBL1_MYJ	0.11	0.17	0.19	0.16	✓	✓	+60	✓	+60	✓
PBL2_MYNN3	*0.06*	0.16	*0.09*	*0.15*	✓	-60	+120	+60	+60	+60
PBL3_ACM2	0.08	*0.15*	0.21	0.18	+60	-60	+180	+120	+60	-120
PBL4_QNSE	**0.20**	**0.33**	**1.11**	**1.51**	+300	+60	+60	+60	+120	+120
PBL5_GBM	0.11	0.22	0.39	0.36	+120	✓	+120	✓	-60	✓
IC1_GFS	0.07	0.17	*0.09*	0.18	-60	-60	+60	✓	✓	-60
IC2_0512	*0.06*	*0.12*	0.23	*0.15*	-180	-180	-120	-120	✓	✓
IC3_0518	0.08	0.20	0.17	0.21	-120	-120	✓	-60	✓	✓
IC4_0606	0.08	0.19	0.17	0.24	+60	✓	+120	✓	✓	✓
IC5_0612	0.14	0.26	0.30	0.50	+180	+120	+60	✓	+60	✓
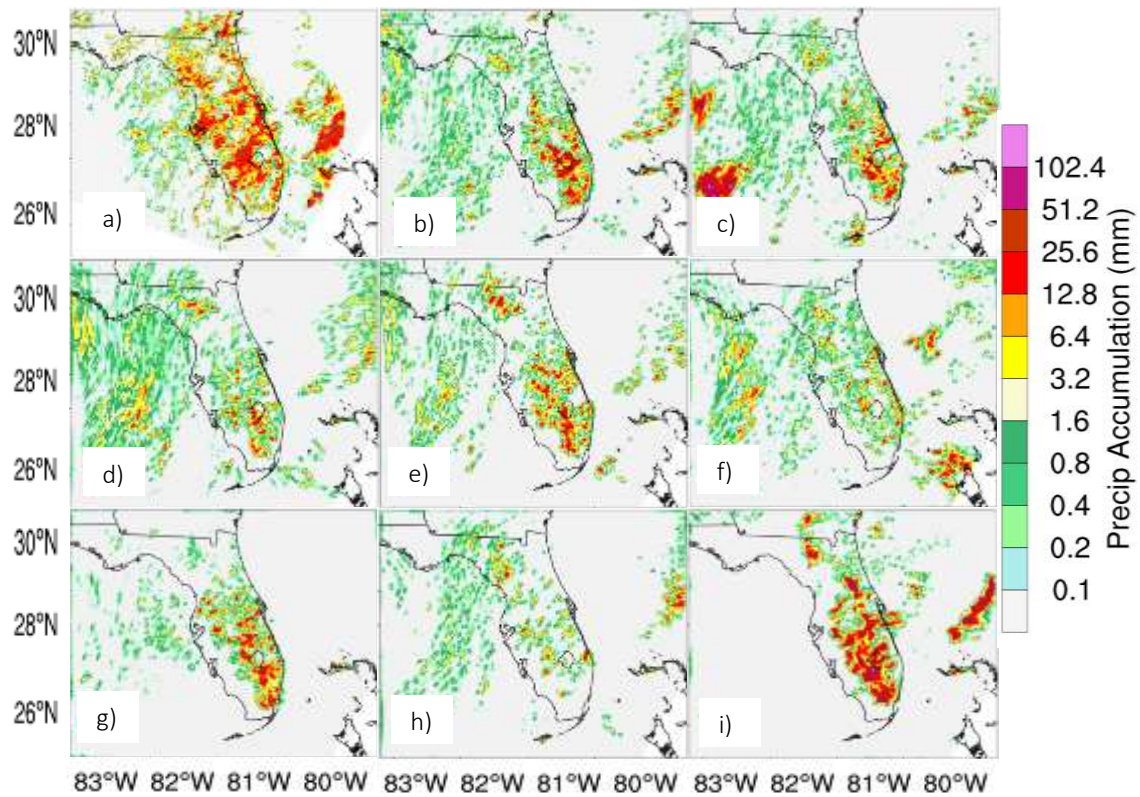
Figure 3.6 18-h (1200 UTC 6 September 2012 to 0600 UTC 7 September 2012) rainfall accumulation totals (color, units mm h^{-1}) for: a) CCPA analysis, b) CU3_NSAS simulation, c) CU4_NT simulation, d) MP3_Mor simulation, e) MP4_SBU simulation, f) IC2_0512 simulation, g) IC5_0612 simulation, h) PBL2_MYNN3 simulation, and i) PBL4_QNSE simulation.

CHAPTER 4

EFFECTS OF GRAY-ZONE GRID SPACING ON

CONVECTIVE INITIATION

According to the results from Chapter 3, the coarser grids are able to resolve the

SB and CI, but the finest grid generally produced better results in many cases. A previous

study by Colby (2003) examined the effect of the grid scale on New England SB

formation using a 36-, 12-, 4-km grid using the fifth-generation Pennsylvania State

University-NCAR Mesoscale Model (MM5). As his study neglects the details on how the

finer grid improves forecasting skill of the SB, as well as the forecasting skill of the finer

grids on SB CI, answers to these questions are warranted. In order to understand the

spatial, timing, and intensity differences produced in the d03 and d04 SB and CI

simulations identified in Chapter 3, further diagnoses of differences in the atmospheric

and geophysical features resolved in these two grid scales for the best simulation

(PBL1_MYJ) is conducted.

4.1 Sensitivity to Geophysical Features

The representation of topography, such as terrain and water bodies, in various grid

scales is important to understanding the differences produced in the gray-zone

simulations. A convex (concave) coastline can enhance (degrade) the formation of the SB

due to the onshore perpendicular flow of the SB enhancing low-level convergence (divergence) over the land area (Figure 4.1, Weaver 2006).

4.1.1 Effects of Coastlines and Bays

A significant difference in the ability of the two gray-zone grids to resolve the observed convective precipitation occurs east of Waccasassa Bay at 1600 UTC 6 September 2012. Specifically, d03 is unable to resolve this convection, while d04 is able to produce convection at this location. Just prior to this time at 1430 UTC 6 September 2012, the WCSB in both domains has been initiated as seen in the u-component of the wind and total winds vectors (Figures 4.2a and 4.2b). However, d04 shows that its higher resolution grid scale allows the WCSB to be initiated more closely along the coastline shape and with slightly stronger winds (Figures 4.2b and 4.2d), leading to areas of enhanced convergence (Figures 4.3b and 4.3d) that are absent in d03 (Figures 4.3a and 4.3c). This narrow band of convergence produced by the SBF in d04 leads to enhanced vertical velocities at the SBF producing the CI seen east of Waccasassa Bay (Figure 4.3d).

In addition, the flow of the winds through the Y-shaped Tampa Bay area (see inset in Figure 4.4) also shows significant enhancement of the winds in the d04 resolution due to its better resolution of the bays' coastline (Figures 4.2b and 4.2d). The marine air flowing through Tampa Bay is funneled to the northwest and northeast around the Interbay peninsula (location of South Tampa Bay and MacDill, AFB) into Old Tampa Bay and Hillsboro Bay, respectively, due to the SB flow (Figure 4.4 inset). This produces strong convergent flow from the SB along the Pinellas peninsula (west of Old Tampa

Bay) and Interbay peninsula. The Tampa Bay breeze and WCSB create a narrow band of enhanced surface convergence which aids in lifting air to its LFC and initiating convection at this time as seen in the bright red reflectivity contours in the d04 simulation just north of the Pinellas peninsula at 1500 UTC (Figure 4.3b). The higher resolution of the FL coastline in d04 also aids in initiating the correct timing of the convection that occurs in the southeast corner of the FL peninsula at 1600 UTC 6 September 2012. In this area, Biscayne Bay creates a convex and concave portion of coastline, which, due to the SB flow, creates two areas of convergent flow to the north and south of the divergent flow produced by the bay breeze.

4.1.2 Lake Effects

In addition to the bay breezes and coastlines affecting the CI in the gray-zone simulations, the lake breezes (LBs) also play an important role in CI. LBs, like SBs, are frequent occurrences in the summertime when cooler lakes create a pressure-gradient effect that generates a lake-to-land movement of air. In addition, lakes are known to significantly impact convection during summer by producing "rain shadows" on the downwind side of the lake (Segal et al. 1997). This occurs when the synoptic wind blowing over the cooler lake surface is cooled and moistened, generating subsidence and the suppression of the CBL, leading to more stable conditions as the wind begins to flow back over land (Segal et al. 1997). It has long been established that Lake Okeechobee, FL's largest lake at 1,825 km^2 (see Figure 4.4), affects convection in terms of LB and rain shadow effects, in both observations and in numerical simulations (e.g., Blanchard and Lopez 1985; Boybeyi and Raman 1992; Segal et al. 1997). As mentioned in Section

3.2.2, the Lake Okeechobee "rain shadow" is observed in observations on 6 September 2012, as well as in the gray-zone WRF simulations (Figures 3.4a and 3.4b), suppressing convection directly downwind of the lake. In contrast to the PBL1_MYJ WCSB and ECSB frontal heights of 850-900 m (Table 3.3), the LB produced by Lake Okeechobee in the d03 PBL1_MYJ simulation is weaker, reaching a height of 400-500 m (Figure 4.5a). In contrast, the d04 PBL1_MYJ simulation for the Okeechobee LB produces a stronger LB with a frontal head of ~800-900 m (Figures 4.5b and 4.5d).

In addition, both PBL1_MYJ gray-zone grid spacings resolve many of the smaller FL lakes, not merely Lake Okeechobee (see Figure 4.4 for lake locations and names). Little research has been done on how the smaller FL water bodies affect the SB, with the exception of studies done on the smaller water bodies surrounding Cape Canaveral (e.g., Laird et al. 1995; Rao and Fuelberg 2000). In the d03 and d04 PBL_MYJ simulations, midsized lakes (lakes between 30-200 km^2), the St. Johns River, and the Indian River are all resolved and effectively produce lake/river breezes at the d03 and d04 grid scales. Small lakes (i.e., lakes between 10-30 km^2) are not resolved in d03, but the higher resolution d04 is able to resolve these lakes and produce associated LBs (see Figure 4.6). Very small lakes (less than 10 km^2) are not resolved at either gray-zone grid scale. Figure 4.7 shows a vertical cross section through the center of the peninsula at 1600 UTC 6 September 2012. The d04 PBL1_MYJ simulation's WCSB and ECSB frontal heads (indicated by blue arrows) show depths of ~600 to 750 m, while in comparison, the LBs (indicated by red arrows) show depths of ~250 m for Lake Weohyakapka (30 km^2) and Lake Marian (23 km^2) to ~375 m for the southern tip of Lake Kissimmee (140 km^2).

In both PBL1_MYJ gray-zone simulations, the LBs produced by the midsized and

small lakes in d03 and d04 are important areas for CI. LBs produce convergent boundary areas on the windward side of the lake that extends in an elongated semicircle around the sides of the lake (due to interactions with the opposing synoptic flow). In the WRF simulation, these convergent frontal areas produced by the LB interacting with the synoptic winds intersect with other boundary areas, such as SBs or other LBs, producing CI. A clear example of this is seen in the interactions of the ECSB, Lake George, Crescent Lake, and Lake Apopka in the d03 grid scale (Figure 4.8). At 1825 UTC 6 September 2012, a strong area of convergence from Lake George and Crescent Lake (Cell 1 in Figure 4.8a) perpendicularly intersects the ECSB, producing a convective cell. Twenty minutes later at 1845 UTC, the convergence area between Lake George and Crescent Lake generates a convective cell (Cell 4 in Figure 4.8d), while just 15 min later, the Crescent Lake breeze again intersects the ECSB (north of the lake), producing a convective cell at 1900 UTC (Cell 5 in Figure 4.8e). A final area of CI due to the LB and ECSB collision in the example occurs at 1910 with the convergent area produced by Lake Apopka (Cell 7 in Figure 4.8f).

In addition to convection produced by the LBs intersecting with other boundary areas, the interaction of the LBs with the synoptic winds also leads to CI. Figure 4.8f shows this interaction. As the LB produced by Lake Apopka interacts with synoptic winds, the convergence area surrounding the lake becomes more and more elongated downstream of the lake in narrow bands. As these convergent bands narrows, vertical velocities increase, causing CI to occur on one of the synoptic wind parallel sides of the lake (Cell 8 in Figure 4.8f). Because the higher resolution of d04 is able to resolve more of the smaller FL lakes, the d04 simulation produces more numerous convergent LB

boundary lines, which in turn, lead to more convective cells being initiated as seen in the d04 PBL1_MYJ simulation (Figure 4.3d) in central FL, as compared to the lack of these convective cells as seen in the d03 PBL1_MYJ simulation (Figure 4.3c).

<p align="center">4.2 Sea Breeze Strength</p>

As mentioned in Chapter 3, all the P/IC simulations produced a larger SB depth and better timing of the SB merger in d04 than in d03. An increase in SB depth is usually indicative of a stronger SBF. Figure 4.9 shows a temporal evolution of the PBL1_MYJ-simulated zonal wind cross sections for d03 and d04, indicating the inland progression and height of the ECSB and WCSB during the afternoon. As can be seen in Figure 4.9, the d04 WCSB and ECSB are significantly deeper than the d03 SBs by several hundred meters.

A stronger SBF is produced by a significant temperature contrast between the continental and maritime air masses and/or a sharp temperature gradient occurring over a narrow horizontal distance, producing a narrow front (Miller et al. 2003). To produce a narrow front, strong low-level convergence must occur associated either with strong opposing offshore winds and/or strong onshore winds within the marine air mass (Miller et al. 2003). Another method to determine frontal strength is analyzing frontogenesis, or the rate of increase of the magnitude of the temperature gradient with time. It can be determined by the following equation:

$$\frac{d}{dt}\left(-\frac{\partial \theta}{\partial y}\right) = -\left(\frac{\partial u}{\partial y}\right)\left(\frac{\partial \theta}{\partial x}\right) + \left(\frac{\partial v}{\partial y}\right)\left(\frac{\partial \theta}{\partial y}\right) + \left(\frac{\partial \omega}{\partial y}\right)\left(\frac{\partial \theta}{\partial p}\right) - \frac{\partial}{\partial y}\left(\frac{\partial \theta}{\partial t}\right) \qquad (\,4.1\,)$$

where the time rate of the temperature gradient $\left(-\frac{\partial \theta}{\partial y}\right)$, is considered a measure of frontal strength. The y-direction is taken to be across the front towards the cooler air. The first

term on the right hand side describes the effect of horizontal shear, the second term terms

contains the effects of convergence, the third term is the tilting term, and the fourth term

is a diabatic term. Arritt (1993) determined that convergence is the dominant term in the

frontogenesis function for a SBF, and what we will consider for the indicator of SB

strength in this study. In the PBL1_MYJ simulations, we see the d04 producing stronger

winds in behind a narrow WCSB and ECSB compared to the d03 (Figure 4.2), thus

producing a sharper thermodynamic temperature gradient and stronger SBF, as also seen

in the more narrow SB frontal convergence zone (Figure 4.3).

4.2.1 Sea Breeze Frontal Convection

While the interaction of the SB with the LBs is a significant factor in producing

convection along the d04 ECSB, this is not seen for the increased d04 WCSB CI (Figures

4.3b and 4.3c). The increased WCSB convection is due to the increased strength and

depth of the d04 WCSB front. D04's stronger SBF is induced in part, by the higher

resolution grid's ability to resolve a slightly larger (1-2°C) land-ocean temperature

difference. This is clearly seen in the temperature differences between d03 and d04 at

1430 UTC 6 September 2012 (Figure 4.10). As the atmosphere above the land and large

bodies of water is sensitive to the specified temperature (Knievel et al. 2010), even this

small temperature difference is enough to produce a stronger land-ocean temperature

gradient in d04 over that in d03.

A larger land-ocean surface temperature gradient will lead to increased low-level

flow within the SBC (i.e., higher SB depth) and increased low-level convergence at the

SBF (for offshore flow). The d03 ECSB band of frontal convergence (Figures 4.3a and

4.3c) is much broader than the d04 ECSB's band of frontal convergence (Figures 4.3b

and 4.3d), showing a much weaker d03 ECSB kinematic front (location of the SBF's

maximum near surface wind convergence (Miller et al. 2003). D04's enhancement of the

SBF (seen in the higher SB depth of 900 m), as compared to d03 (SB depth of 850 m),

leads to increased vertical velocities at the SBF, producing more frequent CI as well.

However, while the d04 convective cells are more numerous, they are also smaller and

produce less organized cells of intense precipitation as compared to the d03 convective

cells. Thus, the higher resolution gray-zone grid spacing seems to have some disability in

developing the convective cells within the simulation, which will be discussed more in

Section 4.3.

4.2.2 Postsquall Line Convection

In the d04 and d03 PBL1_MYJ simulations, the observed squall line produced by

colliding SBs at 2040 and 2120 UTC 6 September 2012, respectively, is captured

reasonably well in terms of timing and spatial location (Figures 4.11a and 4.11b).

However, following the generation of this squall line from the colliding SBs, the

convective system's orientation in the d03 grid simulation evolves quite differently from

the orientation of the observed convective system. From 2300 UTC 6 September 2012 to

0100 UTC 7 September 2012, the pattern of precipitation seen in the d03 simulation is

significantly different from the observations and the d04 simulation results (Figures 4.11c

and 4.11d). CCPA and Stage IV analyses show that the postsquall line convective system

tends to have a northeast to southwest orientation, while the d03 simulation creates a

distinct north to south band of convective cells instead.

The causes of the discrepancies in the postsquall line convective orientation are due to differences in the strength of the squall lines produced in the two gray-zone PBL1_MYJ simulations. Figures 4.12a and 4.12b show the zonal winds of d03 and d04, respectively, just after the SBF merger and generation of the squall line convection at 2100 UTC 6 September 2012. It is evident that the SBF and associated convective cells produced by the d04 output are much stronger than those produced by the d03 output along the squall line. An hour later, the northern half of the d04 squall line continues to propagate eastward (Figure 4.12d), while the weaker squall line in d03 remains essentially motionless in the east central portion of the peninsula (Figure 4.12c). By 2300 UTC 6 September 2012, the d03 postsquall line convection is still in the central portions of the peninsula (Figure 4.12e), while the d04 postsquall line convection system has propagated eastward to FL's eastern coast (Figure 4.12f).

4.3 Summary

In summary, decreasing the gray-zone grid scale demonstrates improvements to forecasting the timing and spatial locations of CI, however, there are still some issues in forecasting the intensity of the convective cells. It is found that improvements to forecasting the timing and spatial locations of CI along SBFs are due to impacts from improved gray-zone resolution of important geophysical features. The improved geophysical resolution of the model leads to enhancements of such atmospheric variables such as low-level convergence and surface sensible heating, which are key ingredients to strengthening the SBFs and aiding in CI. Compared with the 3-km grid scale, the 1-km gray-zone grid scale enables better resolution of the FL coastline and the smaller FL lakes

(10-30 km^2), which leads to added land-water interfaces. The land and water bodies generate a significant temperature gradient between each other, effectively enhancing the SB flow along the sea- and lakeshores. These increased SB and LB winds produce enhanced low-level convergence, and in turn, to stronger SBFs and LBs. The enhanced SBs and LBs produced stronger updrafts at the SBFs' (LBFs') head, which aided the parcels in reaching their LFC and producing convection, thus producing key locations for higher frequency and more numerous CI not seen in the coarser WRF grid domains.

In addition, the stronger SBFs generated in the d04 grid zone simulation led to a more intense squall line being produced following the SBF mergers. This stronger squall line convection in the d04 grid scale was key in determining more accurate postfrontal locations of the convective systems as compared to the d03 grid scale. When the two SBFs merge into the squall line, the stronger SBF and convective cells in d04 aid the propagation of the convection system eastward, rather than it stagnating the MCS in the center of the peninsula as is seen in the d03 simulation of the postsquall line convection. However, the d04 gray-zone grid space did produce some decrease in the forecasting skill of the PBL1_MYJ simulation in the intensity of the convective precipitation, as the d04 simulation produced smaller, more numerous convective cells as compared to the d03 simulation. The decreased forecasting skill in the intensity of the simulated convection at the 1-km grid scale may be due to issues of parameterizations of boundary layer processes (e.g., turbulence, nonlocal mixing effects, dissipation, etc.) in the gray-zone grid spacing being unable to convert energy from the unresolved scales into forcing to the resolved scales in a correct manner. In order to determine this hypothesis, the effects of adding a stochastic representation to the physical variables is examined for the study.
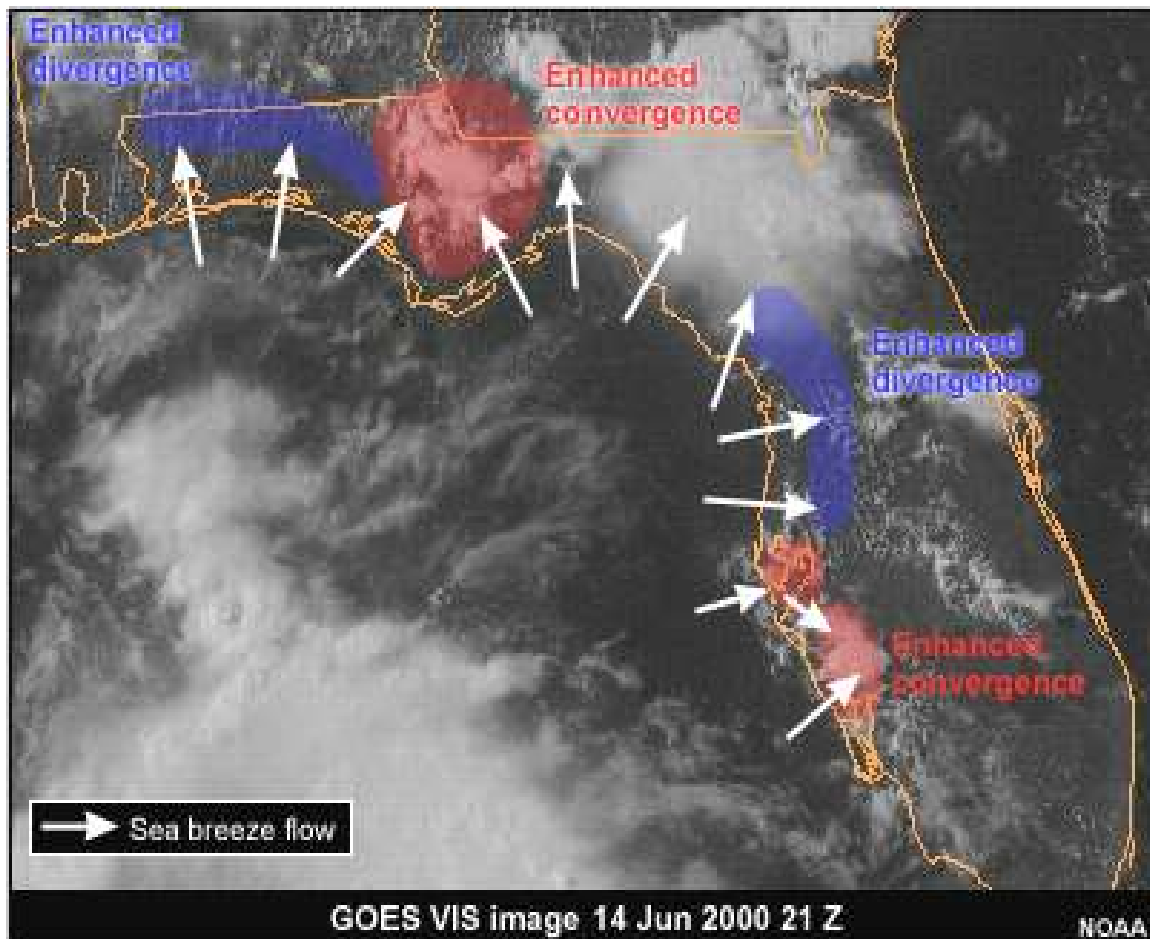
Figure 4.1 Map of convergent and divergent sea breeze flow along the convex and concave coastlines of Florida. Red areas indicate enhanced convergence, blue represents enhanced divergence. (Image courtesy of UCAR COMET program's Thermally-forced Circulation I: Sea Breezes module, http://www.meted.ucar.edu/mesoprim/seabreez/print.htm, 2001).
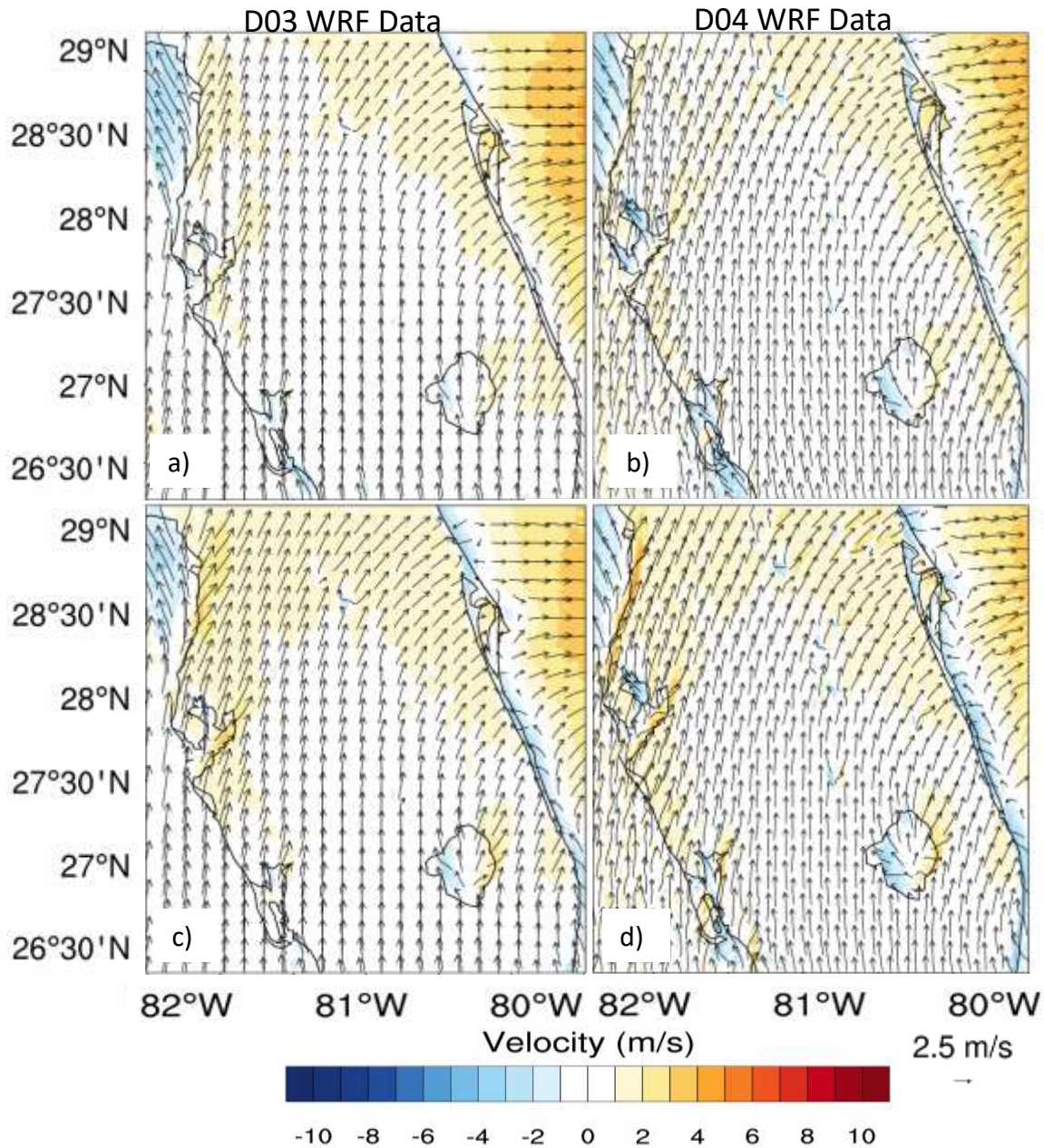
Figure 4.2 PBL1_MYJ simulation zonal (u-component) winds (color: red easterly, blue westerly, units m s^{-1}) and total wind (black arrows, reference vector 2.5 m s^{-1}) for a zoomed-in region of d03 (blue box in Figure 3.1) at a) 1430 UTC and c) 1500 UTC 6 September 2012. Panels b) and d) are the same as a) and c), respectively, but for the zoomed-in region of d04 (blue box in Figure 3.1).

Figure 4.3 PBL1_MYJ simulation divergence (color: red convergence, blue divergence, units s[-1]) and total wind (black arrows, reference vector 2.5 m s^{-1}) for a zoomed-in region of d03 (blue box in Figure 3.1) at: a) 1500 UTC and c) 1530 UTC 6 September 2012. Panels b) and d) are the same as a) and c), respectively, but for the zoomed-in region of d04 (blue box in Figure 3.1) and include max reflectivity (red contours, units dBZ).
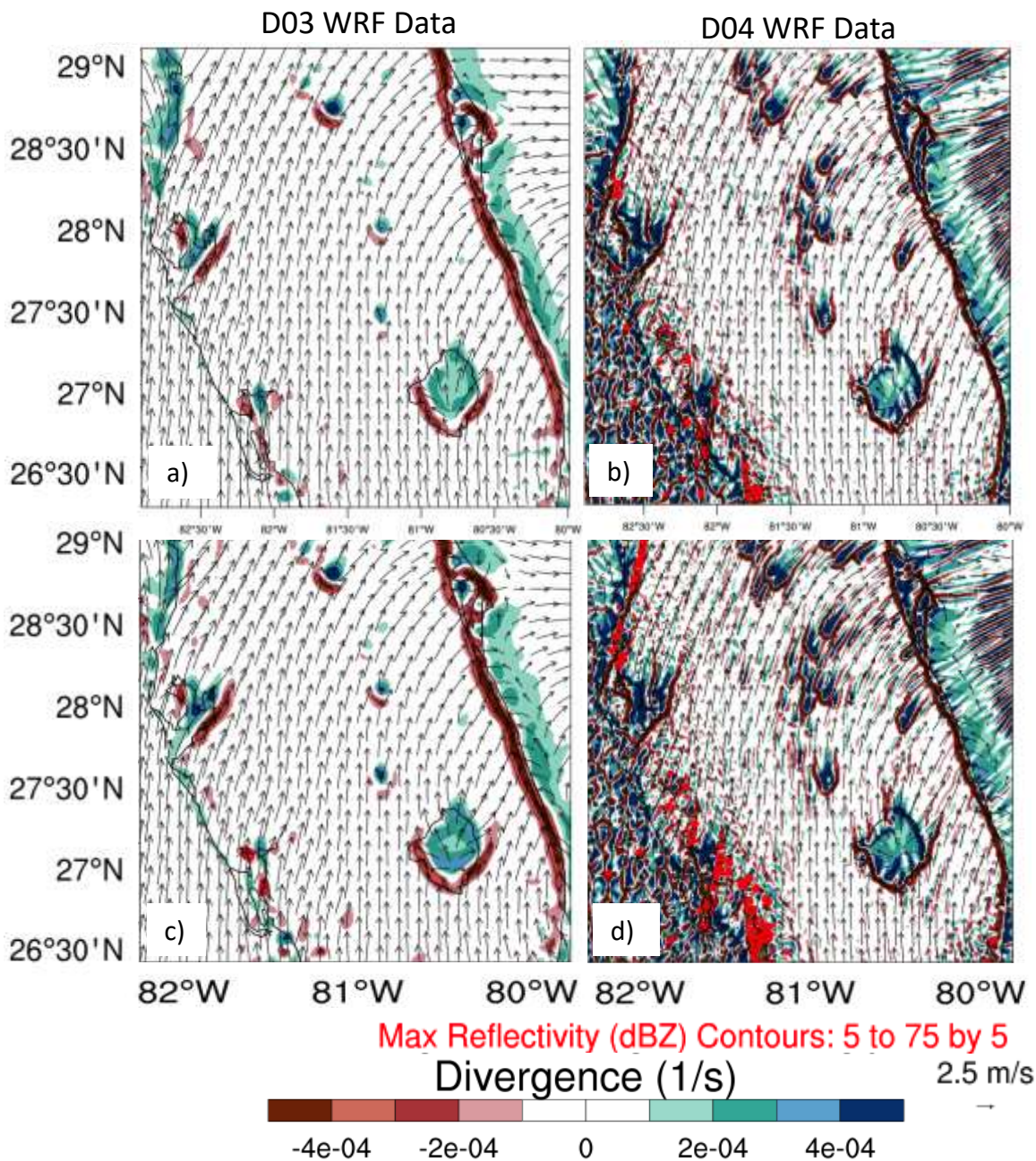
Figure 4.4 Map of locations and names of Florida water bodies, including lakes larger than 50 km2. The inset in the left corner shows a zoomed-in region of Tampa Bay.

Figure 4.5 Cross section (through northernmost red line in Figure 3.1) of WRF-simulated zonal (u-component) winds (color: red easterly, blue westerly, units m s^{-1}) and total horizontal wind (black arrows, reference vector 10 m s^{-1}) at 1700 UTC 6 September 2012 for a) d03 and b) d04. Red contour line indicates the zero wind contour heights, which indicate the Lake Okeechobee's approximate lake breeze heights.

Figure 4.6 Temperature difference (color contours, units °F) between the d03 and d04 PBL1_MYJ simulations at 0330 UTC 6 September 2012 for a zoomed-in region of d03 and d04 (yellow box in Figure 3.1). The temperature differences between the two domains are due to the d04's higher resolution (1 km) enabling it to better resolve the coastlines, rivers, and smaller lakes (10-30 km^2) than the d03 (3 km resolution).
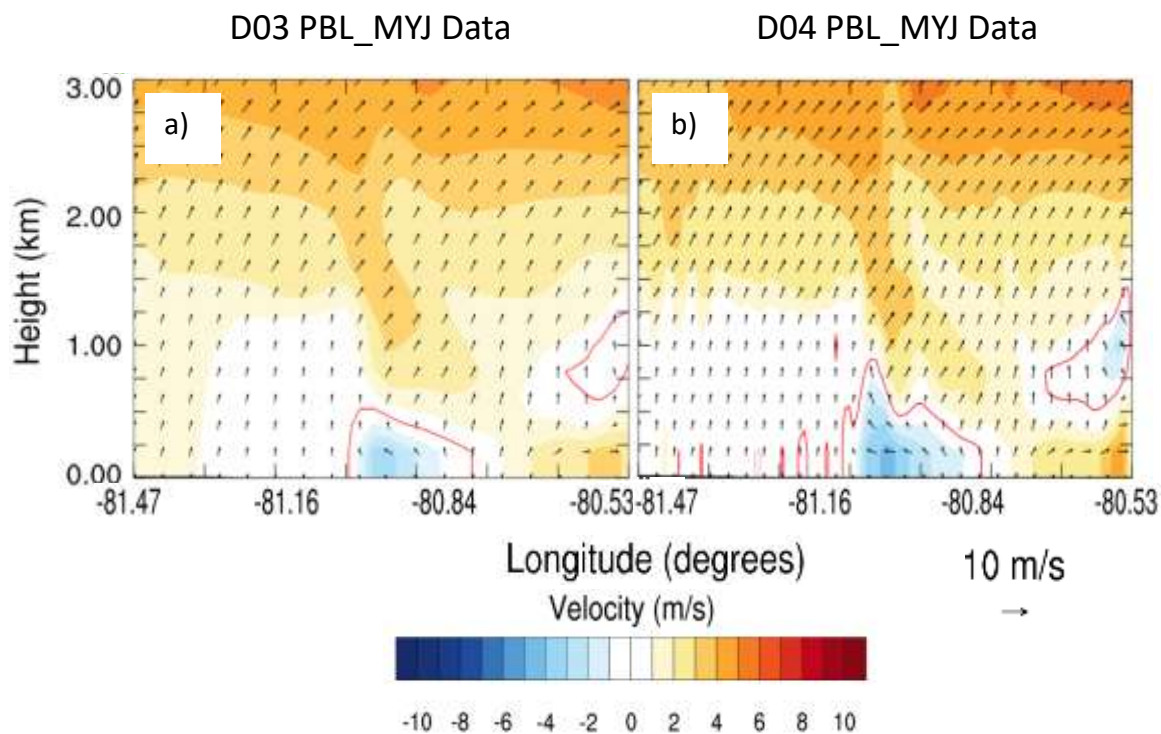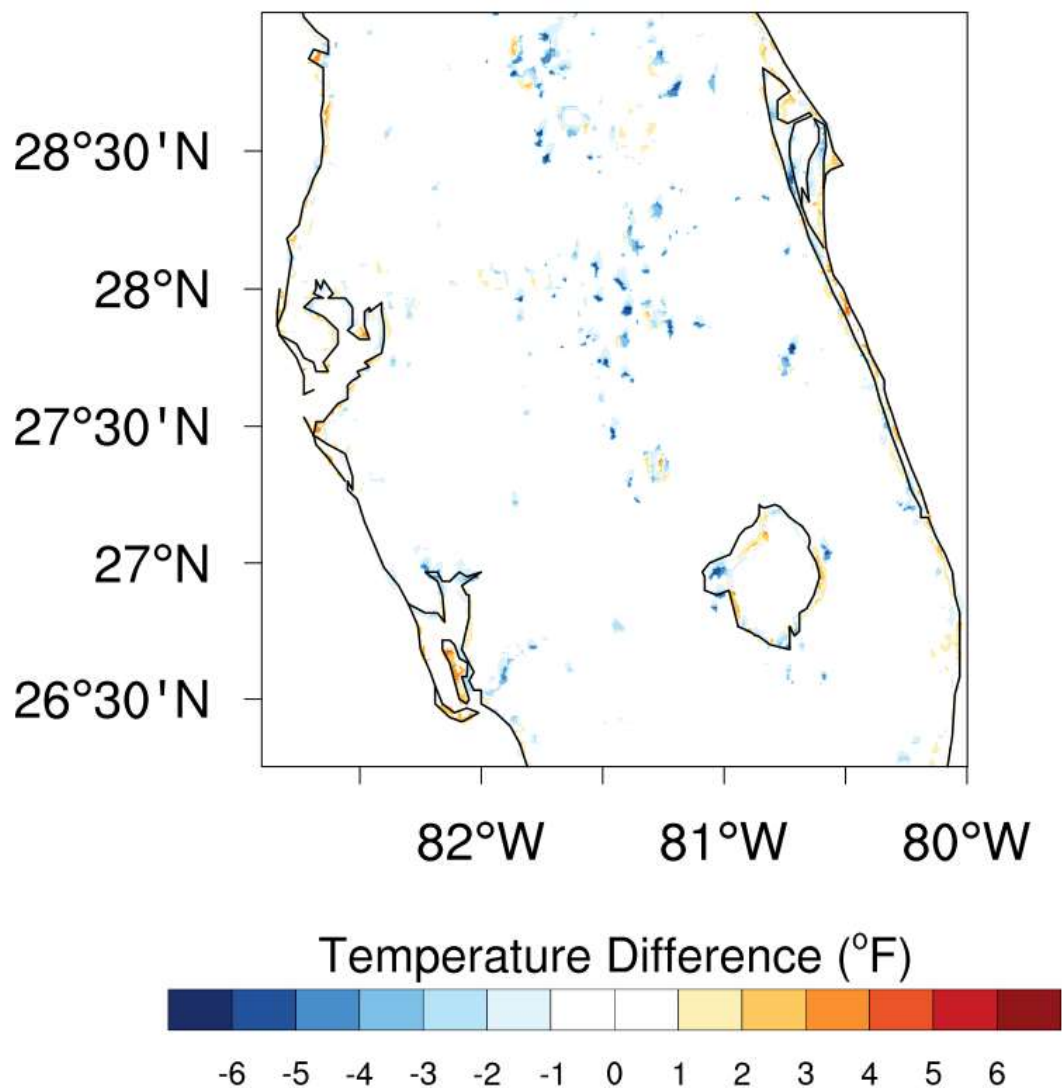
Figure 4.7 Cross section (through northernmost red line in Figure 3.1) of d04 PBL1_MYJ simulation's zonal (u-component) winds (color: red easterly, blue westerly, units m s^{-1}) and total horizontal wind (black arrows, reference vector 10 m s^{-1}) at: a) 1600 UTC 6 September 2012. Red contour line indicates the zero wind contour heights, which indicate the Lake Okeechobee's approximate lake breeze heights. Blue arrows indicate the locations of the SBs, while the red arrows indicate the lake breezes for 1) Lake Weohyakapka, 2) Lake Kissimmee, 3) Lake Marian, and 4) Indian River.
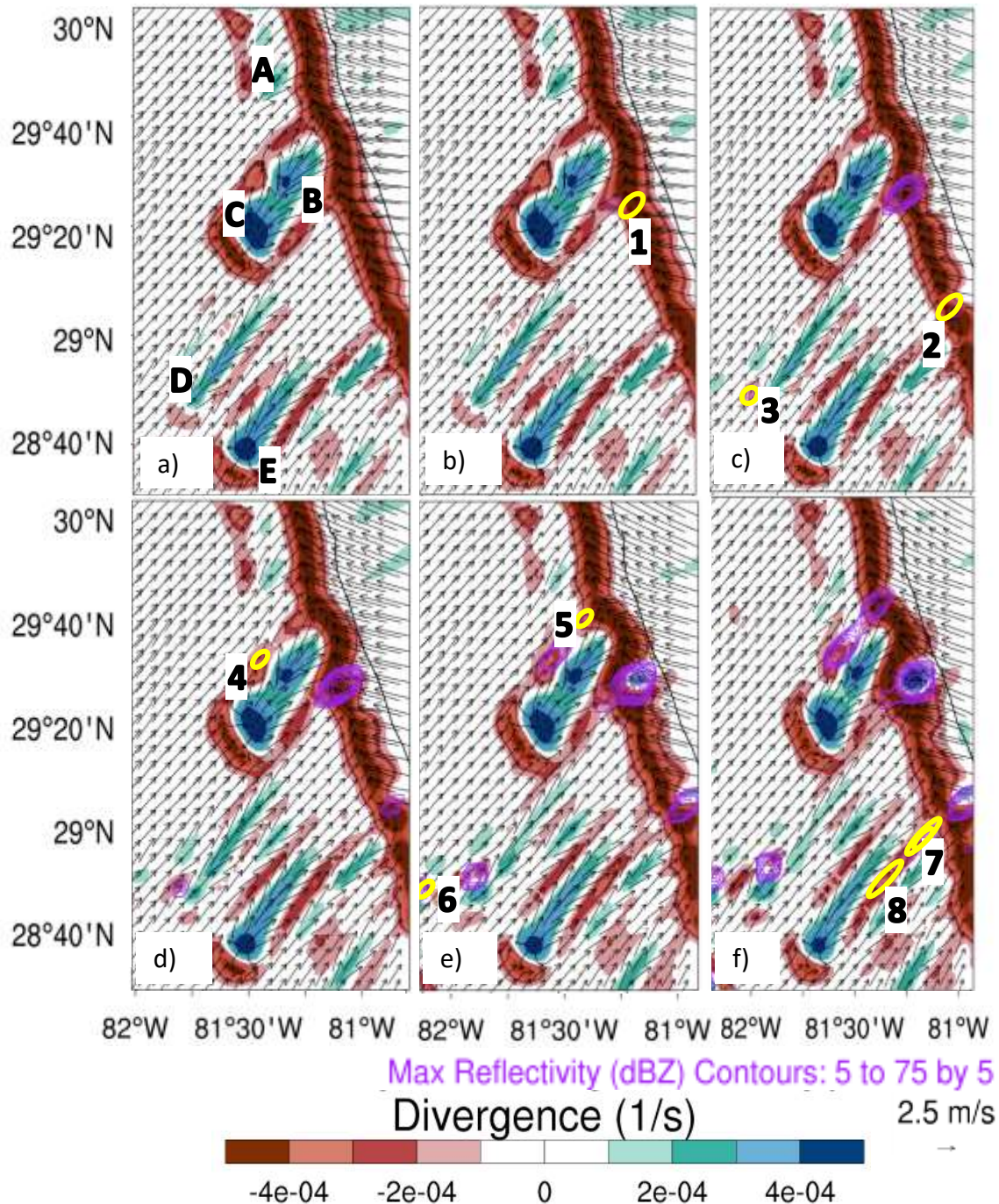
Figure 4.8 D03 PBL1_MYJ-simulated divergence (color, units s^{-1}), max reflectivity (yellow and purple contours, units 5 dBZ) and total wind (black arrows, reference vector 2.5 m s^{-1}) for a zoomed-in region of d03 (purple box in Figure 3.1.) at: a) 1820 UTC, b) 1825 UTC, c) 1840 UTC, d) 1845 UTC, e) 1900 UTC, and f) 1910 UTC 6 September 2012. Yellow reflectivity contour lines indicate the convective cell's first appearance in the simulation and are numbered accordingly in panels b-f), thereafter, the reflectivity contour lines are purple. Panel a) indicates the lake effect divergence from the following water bodies: A) St John's River, B) Crescent Lake, C) Lake George, D) Lakes Griffin, Harris, and Eustis, E) Lake Apopka. See text for more details.
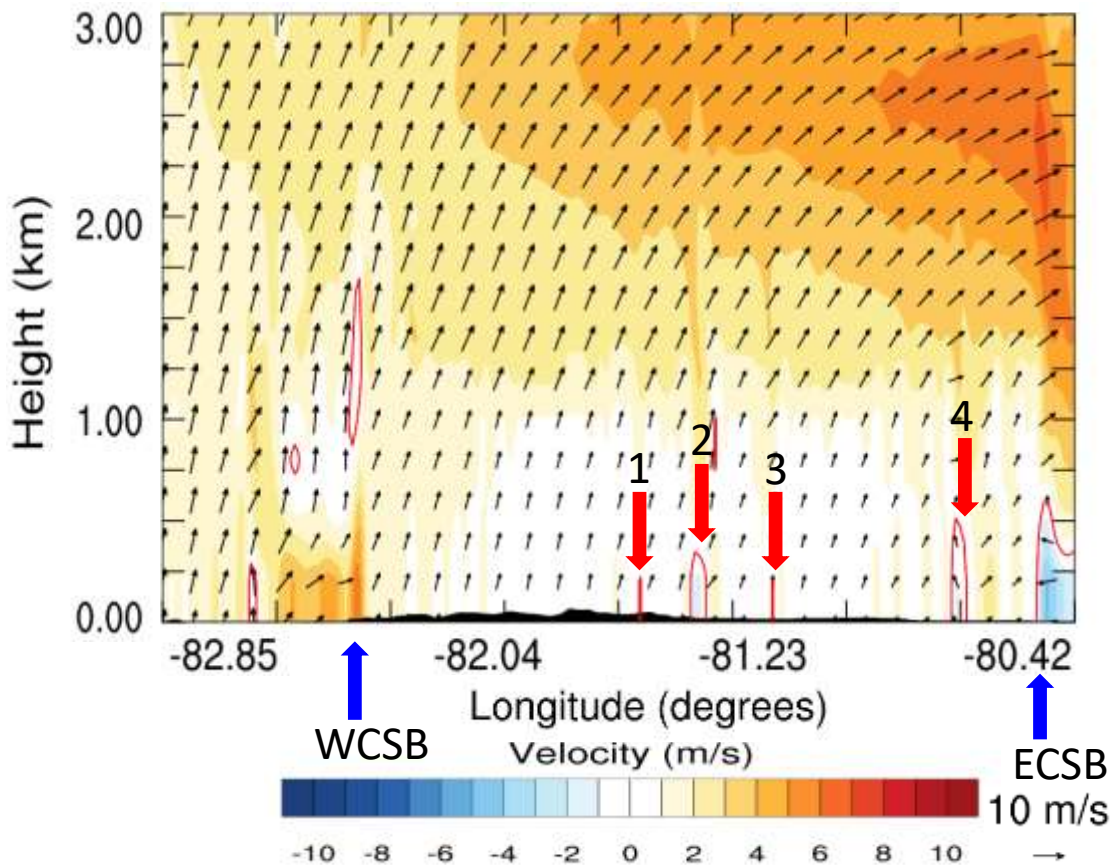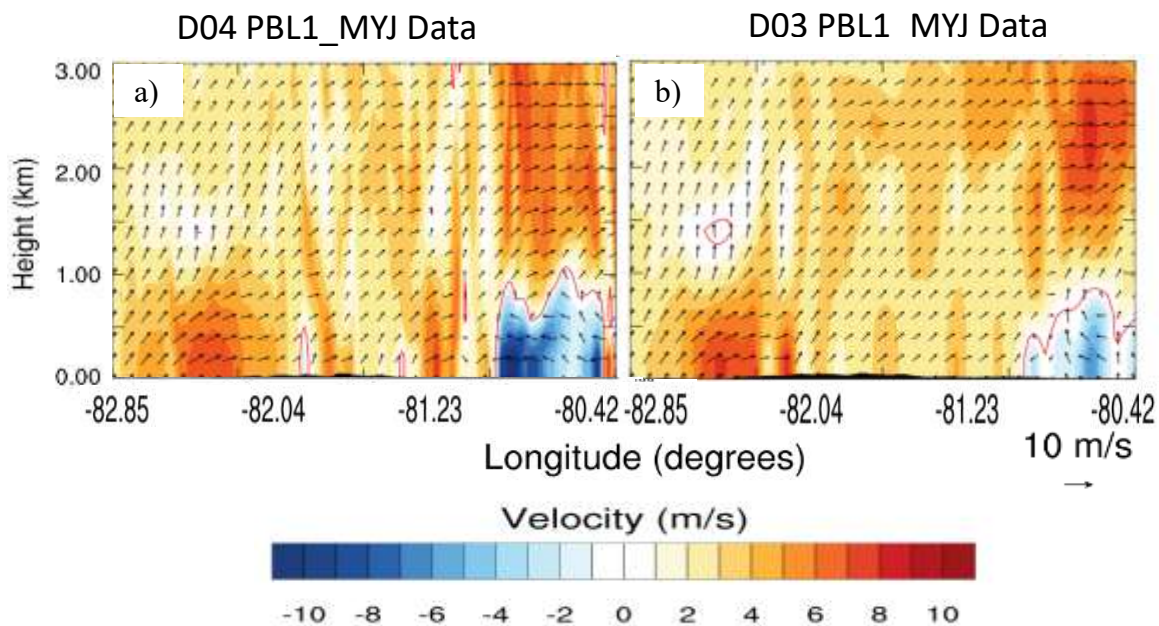
Figure 4.9 Cross section (through northernmost red line in Figure 3.1) of PBL1_MYJ-simulated zonal (u-component) winds (color: red easterly, blue westerly, units m s^{-1}) and total horizontal wind (black arrows, reference vector 10 m s^{-1}) at 2030 UTC 6 September 2012 for a) d04 and b) d03. Red contour line indicates the zero wind contour heights, which indicate the Lake Okeechobee's approximate lake breeze heights.
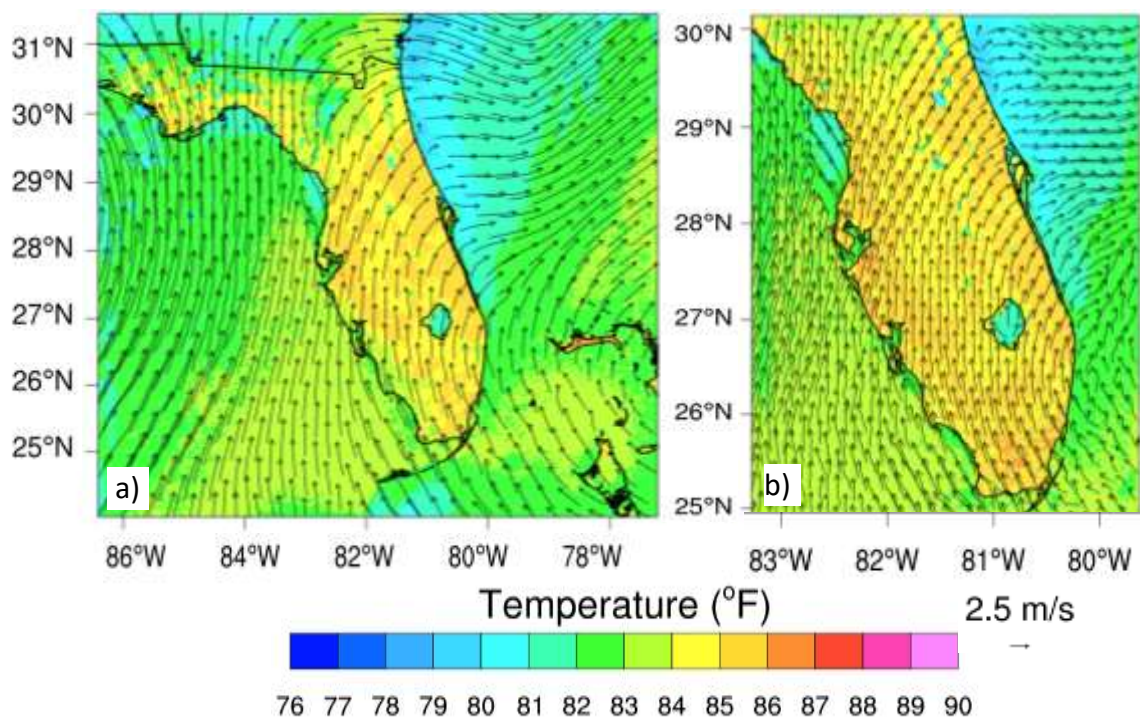
Figure 4.10 PBL1_MYJ-simulated temperature (color, units °F) and total wind (black arrows, unit reference vector 2.5 m s^{-1}) for a) d03 and b) d04 at 1430 UTC 6 September 2012.
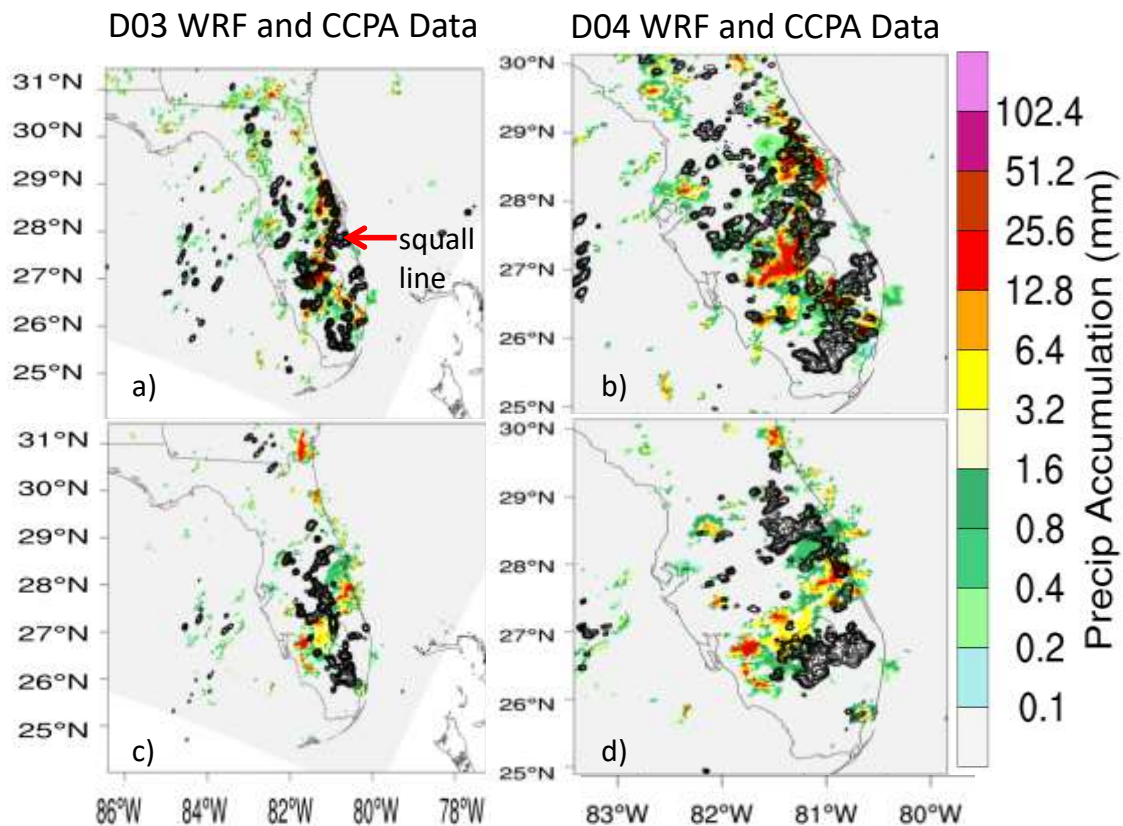
Figure 4.11 Stage IV precipitation accumulation (color, units mm h^{-1}) and d03 (left column) and d04 (right column) PBL1_MYJ-simulated precipitation accumulation (black contours, units mm h^{-1}) at: a-b) 2100 UTC, and c-d) 2300 UTC 6 September 2012.

Figure 4.12 PBL1_MYJ-simulated zonal (u-component) winds (color: red easterly, blue westerly, units m s^{-1}) and total wind (black arrows, reference vector 2.5 m s^{-1}) for a zoomed-in region of d03 (blue box in Figure 3.1) at a) 2100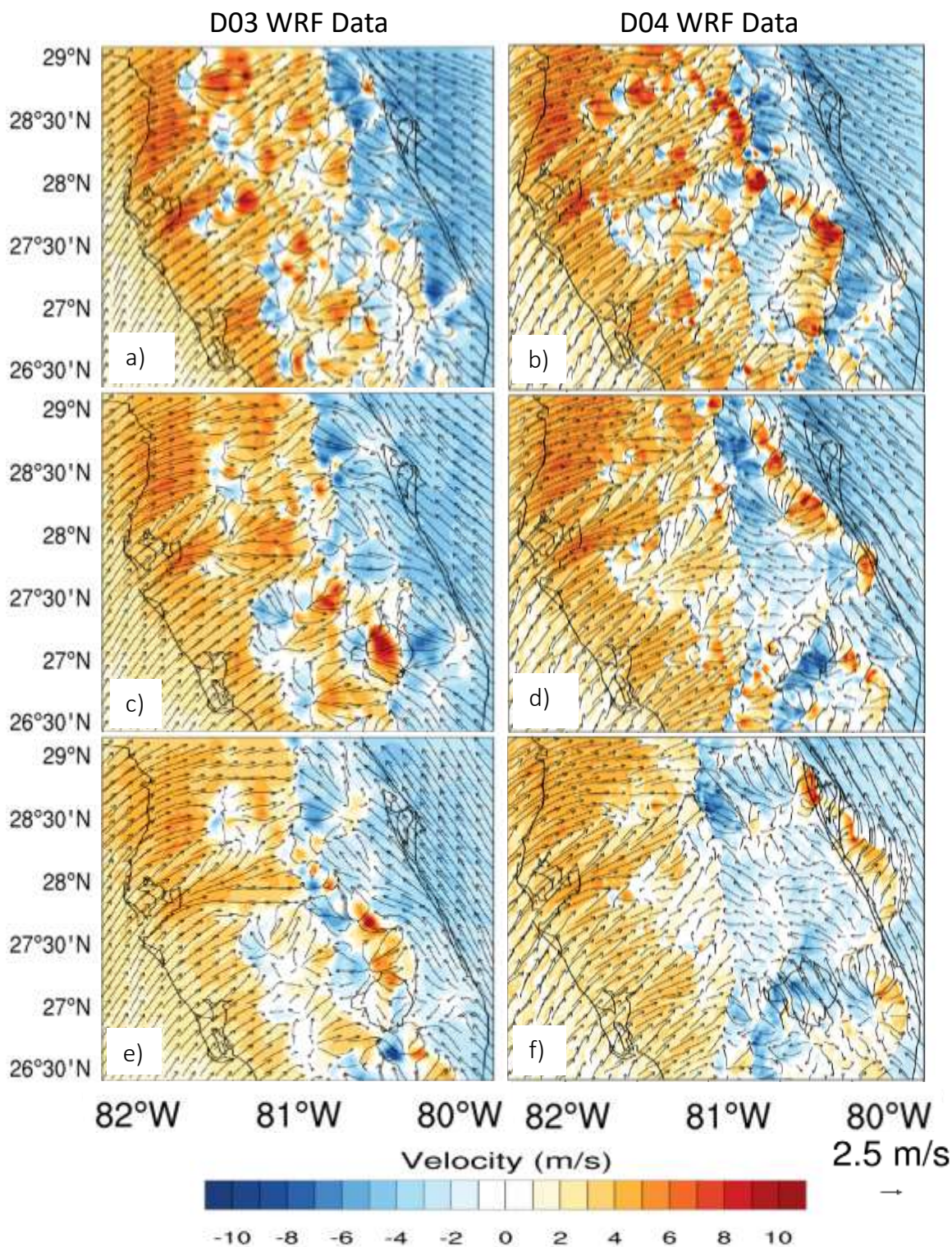 UTC, c) 2200 UTC, and e) 2300 UTC 6 September 2012. Panels b), d), and f) are the same as a), c), and e) respectively, but for the zoomed-in region of d04 (blue box in Figure 3.1).

CHAPTER 5

NUMERICAL SIMULATIONS WITH STOCHASTIC

PERTURBATIONS

As mentioned in Chapter 1, stochastic parameterization (or perturbation) methods act to take a variable or process and express it in terms of a resolved term(s) and an unresolved term(s). The unresolved term(s) is represented as statistical fluctuations (i.e., additive noise with spatial and temporal correlations) in order to better determine the unrepresented two-way interactions of kinetic energy across the model truncation boundary between the resolved and unresolved scales (Berner el al. 2008, 2011).   In addition, stochastic perturbation ensembles increase diversity among ensemble members, making a more reliable and skillful ensemble system (Berner et al. 2008). From an operational standpoint, the stochastic perturbation method is also advantageous as it requires less support and maintenance resources, as well as ensures that all ensemble members have the same climatology and model bias (in contrast to multi-parameterization or multimodel ensembles, which have issues with both of these factors).

The P/IC simulations of the SB convection detailed in Chapter 3 have shown that the WRF model can realistically reproduce the SB CI. However, large sensitivities of the SB and its associated CI to physical parameterizations are seen, especially to the PBL schemes. Within the gray-zone grid scale, the number of subgrid turbulent eddies are no longer large enough to fulfill the "law of large numbers" underlying the bulk

parameterization assumptions, and thus, the use of the parameterizations may cause too much energy to be removed from the resolved to the unresolved scales (Berner et al. 2012). This is where a stochastic approach could be of additional benefit. In order to determine whether an added effect of stochastic parameterization may allow for better representation of the mean state in our simulation, an ensemble of stochastic perturbations for the 6-7 September 2012 SB event (described in Chapter 2) is conducted. We hypothesize that simulations of a SB CI event would show sensitivity to stochastic perturbation simulations, allowing for a unique opportunity to compare how the stochastic and physics parameterization simulations each handle the development of the SB CI within the WRF-ARW model

5.1 Configuration of Simulations with Stochastic Perturbations

The WRF-ARW has an option to stochastically perturb forecasts via a stochastic kinetic energy backscatter scheme (SKEBS). SKEBS aims at representing model uncertainty resulting from interactions with unresolved scales and was originally developed in the context of the LES (Berner et al. 2011). It is based on the notion that the rate of turbulent dissipation is the difference between downscale and upscale spectral transfer, with the parameterized upscale component being available to the resolved flow as a kinetic energy source (Shutts 2005). In the WRF-ARW, SKEBS takes a fraction of the subgrid scale energy (i.e., dissipated kinetic energy) and scatters it upscale to make it available as forcing for the resolved flow (Shutts 2005). To do this, SKEBS introduces random temporally and spatially correlated perturbation fields to the rotational wind components (u, v), and potential temperature (θ) with a prescribed kinetic energy

spectrum, which are simply considered additive noise (Skamarock et al. 2008). These perturbation fields are then added to the physics tendencies of *u, v,* and *θ* variables within the model at each time step. The stochastic perturbations fields for wind and temperature are controlled by the kinetic and potential energy they inject into the flow and are expressed as a constant backscattered dissipation rate. Mathematically, with the SKEBS, the effective streamfunction $\Psi'(x, y, t)$ and potential temperature $\Theta'(x, y, t)$ perturbations are given by

$$\Psi'(x, y, t) = rD(x, y, z)\psi'(x, y, t) \qquad (5.1)$$

$$\Theta'(x, y, t) = rD(x, y, z)\theta'(x, y, t) \qquad (5.2)$$

where *x* and *y* are the zonal and meridional directions in physical space and *t* denotes time. *D(x,y,t)* is the local, instantaneous dissipation rate and *r* denotes the backscatter ratio parameter. ψ' and θ' are the 2D streamfunction and potential temperature patterns with a prescribed kinetic energy spectrum, respectively. The spatial and temporal characteristics of the perturbation pattern are controlled by expanding the ψ and θ patterns in spectral space and evolving each wavenumber as a 1st-order autoregressive process. Further details and description of the SKEBS can be found in Berner et al. (2011).

In the stochastic perturbation experiment study, we chose to use 20 SKEBS simulations, the same number of experiments as the P/IC sensitivity study described in Chapter 2 (SKEBS simulation members are labeled Skeb1 through Skeb20). In order to observe solely the effects of the SKEBS perturbations on the simulation, each SKEBs simulation is configured with the same domain setup, physics options, and ICs as the CTRL simulation (see Chapter 2 for details on the CTRL configuration). Each simulation

is configured with the SKEBS applied to all four domains and their boundary conditions as well, in order to simulate uncertainty in the flow through the boundaries. A constant structure of the perturbations' vertical pattern is also used. The streamfunction and potential backscatter dissipation rates used are 1.E-05 m^2s^{-3} and 1.E-06 m^2s^{-3}, respectively, with a decorrelation time for both perturbations set to 3 h. The standard deviation of the random perturbation fields at each grid point is set to 0.03 and the cutoff tails of the both perturbation patterns is set at a standard deviation of 3.0. The length scale for the random perturbations is 500 km, with a timescale of 6 h. Figures 5.1 and 5.2 show an example of the θ and u,v wind perturbation tendency fields for two SKEBS simulations.

5.2 SKEBS Ensemble Results and Comparison to P/IC

Sensitivity Study

Results from the 20 SKEBS simulations (Skeb1-Skeb20) conducted for the 6-7 September 2012 SB convection case have been analyzed in terms of SB timing, depth, and SBF merger. An analysis of the performance of the SKEB simulations in the timing, location, and intensity of the SB CI is also conducted. The same verification methods used for the ensemble of the P/IC experiments (as described in Section 3.1.) are used in this section to analyze the sensitivity of the stochastic perturbations to the simulated SB and its associated CI in the gray-zone grid spacing. These analyzed results are then compared to previous P/IC sensitivity results.

5.2.1 Sea Breezes in SKEBS Simulations

The initiation times of the SB from the SKEBS simulations is given in Table 5.1.

As with the P/IC simulations, all the SKEBS simulations were able to resolve the SB.

The SKEBS simulations show greater variability in initiation times of the WCSB and

ECSB as compared to the P/IC simulations (Table 3.3), as well as the intensity of the SBs

as seen in the average SBF depth and SB merger time. Initiation of the SBs varied from

60 min prior to observations (Skeb6 and Skeb10) to 30 min after observations (Skeb6 and

Skeb20). However, while the P/IC simulations had 5 out of the 20 simulations (25%) that

varied in SB initiation timing from the observations, the SKEBS simulations had 15 out

of 20 simulations (75%) that showed a difference in SB timing from the observations.

SBF merger timing of the SKEBS simulations averaged +69 min for d03 and +17 min for

d04, which is very similar to the P/IC simulation results (averaged +64 and +17 min for

d03 and d04, respectively).

SB depth in the SKEB simulations ranged from 650 m (Skeb5, d03) to 1,250 m

(Skeb8, d04), showing slightly more variable than the P/IC simulations. As with the P/IC

simulations, the SKEBS simulations also saw increased SBF strength in the d04 from the

d03, as seen in the increased SB depth and earlier SB merger timing. In contrast to the

P/IC simulations that never produced a stronger ECSB over the WCSB, there are six

SKEBS simulations (Skeb5, Skeb10, Skeb12, Skeb16, Skeb17, and Skeb18) that are able

to generate a stronger ECSB over the WCSB. These stronger ECSB fronts show larger

SB depths over the WCSB fronts and propagated much further inland than seen in the

P/IC and other SKEBS simulations, leading to a merger of the SBFs in the central

portions of FL rather than in the east-central portions of FL from observations (Figure

5.3). Furthermore, three SKEBS simulations (Skeb4, Skeb8, and Skeb9) were similar in producing very strong offshore winds along the east coast of FL during the simulation, leading to an ECSB that barely propagated inland and a WCSB and ECSB merger that occurred along the east coast of FL, rather than parallel to the east coast in east central FL (Figure 5.3).

Figure 5.4 shows a vertical cross section of zonal winds across the FL peninsula at 2130 UTC 6 September 2012. The two simulations with an almost stationary ECSB (Skeb8 and Skeb9) and are shown to have strong southwesterly synoptic winds within the lowest 3 km of the atmosphere. In contrast, the two simulations with a strong eastward propagating ECSB (Skeb16 and Skeb18) show much weaker synoptic winds within the PBL. Furthermore, Figure 5.4 shows that the weak southwesterly synoptic winds for the Skeb16 and Skeb18 simulations allowed for a much stronger ECSB (as seen in the larger depth of the ECSB front and penetrated west of -81W), while the strong synoptic winds of the Skeb8 and Skeb9 simulations led to a ECSB that did not penetrate further past the east coast (-80.6W). These weaker southwesterly synoptic winds allowed for a much larger and distinct return current of the WCSB as seen in the negative u-wind values several hundred meters surface in Figures 5.4c and 5.4d Figures 5.4a and 5.4b show the reverse, where there is no distinct return currents seen in the lower atmosphere along the WCSB.

5.2.2 Convective Initiation Results for SKEBS Simulations

Results for the SB CI in the SKEBS simulations are given in Table 5.2, and as with the P/IC simulations, all the SKEBS simulations are able to resolve the SB

convection for the 6-7 September 2012 SB case. As also seen in the P/IC simulations, none of the SKEBS simulations are able to successfully resolve the timing and the SB CI. Simulations Skeb5, Skeb6, Skeb15, Skeb16 are the worst at forecasting the timing of the SB CI and/or the duration of the convective event, while the Skeb2, Skeb3, Skeb7, Skeb9, Skeb11, Skeb12, and Skeb14 SKEBS simulations are among the best in terms of SB CI timing and duration. In addition, the increased resolution of the gray-zone grid spacing shows an overall improvement to SB CI timing and duration within the SKEBS simulations.

In terms of Threat Scores, Skeb1 and Skeb16 simulations produce the best results, while the Skeb9 and Skeb20 simulations produce the worst results. The range and average Threat Scores for the SKEBS simulations is similar to that of the P/IC simulations for d03 (average TS of 0.11 for both ensembles), however the P/IC simulations show higher average TS values in d04 as compared to the SKEBS TS values for d04 (SKEBS TS of 0.15 compared to P/IC TS of 0.21). Furthermore, the d03 bias scores for the SKEBS simulations show a tendency to overforecast precipitation, while the P/IC simulations tended to underforecast precipitation (SKEBS average BS of 1.10 compared to P/IC average BS of 0.30), with eight simulations (Skeb5, Skeb6, Skeb11, Skeb12, Skeb13, Skeb15, Skeb16, and Skeb19) indicating a significant overforecast of the precipitation intensities in several locations as compared to CCPA analysis. The d04 bias scores for the SKEBS show a reversal of intensity forecasting as they now tend to significantly underforecast precipitation intensity, even more so than the P/IC simulations (SKEBS average BS of 0.19 compared to P/IC average BS of 0.36).

As with the convective intensities, differences in spatial coverage of the SB

precipitation accumulations are seen for all the SKEBS simulations. A comparison of the

diversity of the convective precipitation spatial coverage and intensity for 8 SKEBS

simulations against the CCPA precipitation accumulations are given in Figure 5.5

Simulations with a stronger ECSB such as Skeb5, Skeb16, and Skeb18 (Figures 5.5c,

5.5h, and 5.5i) showed the strongest precipitation accumulations in the southwest corner

of the peninsula, while simulations with a stationary ECSB (i.e., strong synoptic winds)

such as Skeb4, Skeb8, and Skeb9 (Figures 5.5b, 5.5e, and 5.5f) produced simulations

with some of the least intense precipitation accumulations over the peninsula.

Furthermore, there is slightly better accuracy in the spatial coverage of precipitation in

the d04 SKEBS simulations as compared to the d03 results (not shown) due to the higher

resolution's tendency to produce smaller, more numerous convective cells, however this

also produced decreased accuracy in the forecasting of the overall intensity of the

convective precipitation accumulations in d04 for the SKEBS simulations.

5.3 Discussion of the P/IC and SKEBS Simulations

While all the P/IC and SKEBS simulations were able to successfully simulate the

FL SBs and their associated CI, there are many differences in the development and

evolution of the SB and CI between the ensembles of the P/IC and SKEBS simulations. A

summary of the impacts to the SB and CI by the various parameters varied in the P/IC

and SKEBS simulations are given in Table 5.3.

The timing and intensity of the SB is sensitive to the PBL, ICs, and SKEBS

parameterizations, though the SB timing is less sensitive to the ICs as compared to the

other two factors. As discussed previously in Chapter 3, the sensitivity of the SB timing

and strength to the PBL and ICs to the SB timing stems from the way the simulations handle the sensible heating of the land surface, or for the IC simulations, how much model spin-up time is allowed for the simulation and the effects of the evolution of the atmospheric variables, such as low-level moisture, in the model's dynamics. The CU and MP parameterization simulations showed little to no sensitivity to the initiation times of the SB or to its intensity.

In comparison, the potential temperature and streamfunction perturbations within the SKEB scheme create added differences in how the model handles not just the low-level heating, but also the low- and mid-tropospheric wind fields, leading to the largest differences seen in simulations on the SB timing and strength. The additive subgrid kinetic energy that is "backscattered" upscale to the resolved temperature and streamflow fields in the SKEBS simulations create large variability in the surface temperature and synoptic wind fields, leading to the variability in the timing and strength of the SB not seen in the P/IC simulations, such as a strongly eastward propagating ECSB or an almost stationary ECSB.

The timing, location, and intensity of the CI showed strong sensitivity to PBL and SKEBS simulations, as well as gray-zone grid spacing. These same CI parameters show only slight sensitivity to the other P/IC simulations. The strong sensitivity of the PBL, SKEBS, and grid scale on CI is in part also due to the fact that these options showed great sensitivity to the SB timing and/or intensity. A premature or late initiation of a SB in a simulation also saw a premature or late CI, though the exact SB timing difference did not produce the same CI timing difference within a simulation.

The SKEBS simulations have shown that adding a stochastic perturbation method

to simulation with physics parameterizations shows mixed results in improvements to forecasts of convective precipitation intensities. The 3-km gray-zone grid can generally produce much larger convective precipitation intensity forecasts if a stochastic parameterization, such as the SKEBS, is added to the simulation, indicating that randomly added kinetic energy from the unresolved grid scales may be necessary for aiding convective processes at this scale. However, the combined stochastic and physical parameterization in the 1-km gray-zone grid spacing produce worse convective precipitation intensities than the P/IC simulations alone, showing that the added kinetic energy from the unresolved grid scales is unbeneficial to the production of higher precipitation intensities for the convective cells at this scale. The SKEBS simulations have shown that improvements can be made to the forecasts of CI, however, as more irregular forecasts of SB intensity and propagation are seen in the ensemble of SKEBS simulations as well, the application of the SKEBS used here may applied too generally to the perturbations fields. Thus, a method to stochastic perturb variable in a more physically consistent way may produce more relevant forecasts of convective precipitation intensities in smaller gray-zone grid spacings.

In summary, the P/IC and SKEBS simulations show a general ability to predict the FL SB convection, although the SKEBS simulations have much more spread in their timing and strength of the SBFs, as well as the timing, location, and intensity of the simulated CI. The parameter that had the worst prediction ability for all 40 simulations was the intensity of the convective precipitation. This is mainly due to the fact that the convective cells produced in the simulations tended to be smaller and more numerous convective cells as compared to NEXRAD radar observations and precipitation analyses.

However, some improvements are seen in the d03 gray-zone grid space forecasts of precipitation intensities with the application of combined stochastic and physics parameterizations.
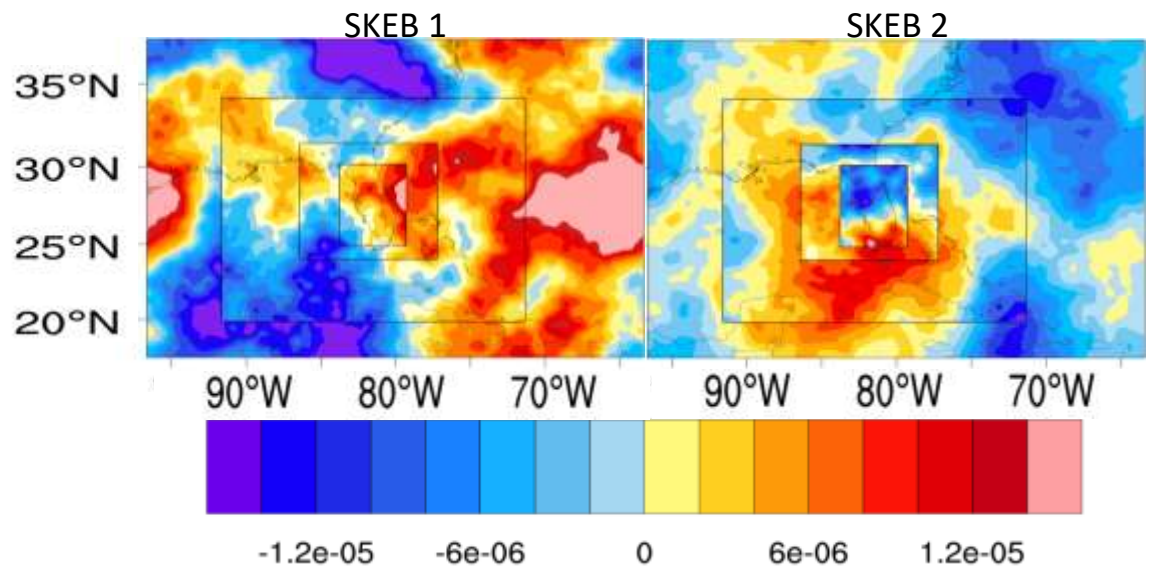
Figure 5.1 Output of potential temperature perturbation tendency fields (color, units Ks^{-2}) for SKEBS simulation Skeb1 (left) and Skeb2 (right). Domain areas are the black boxes.
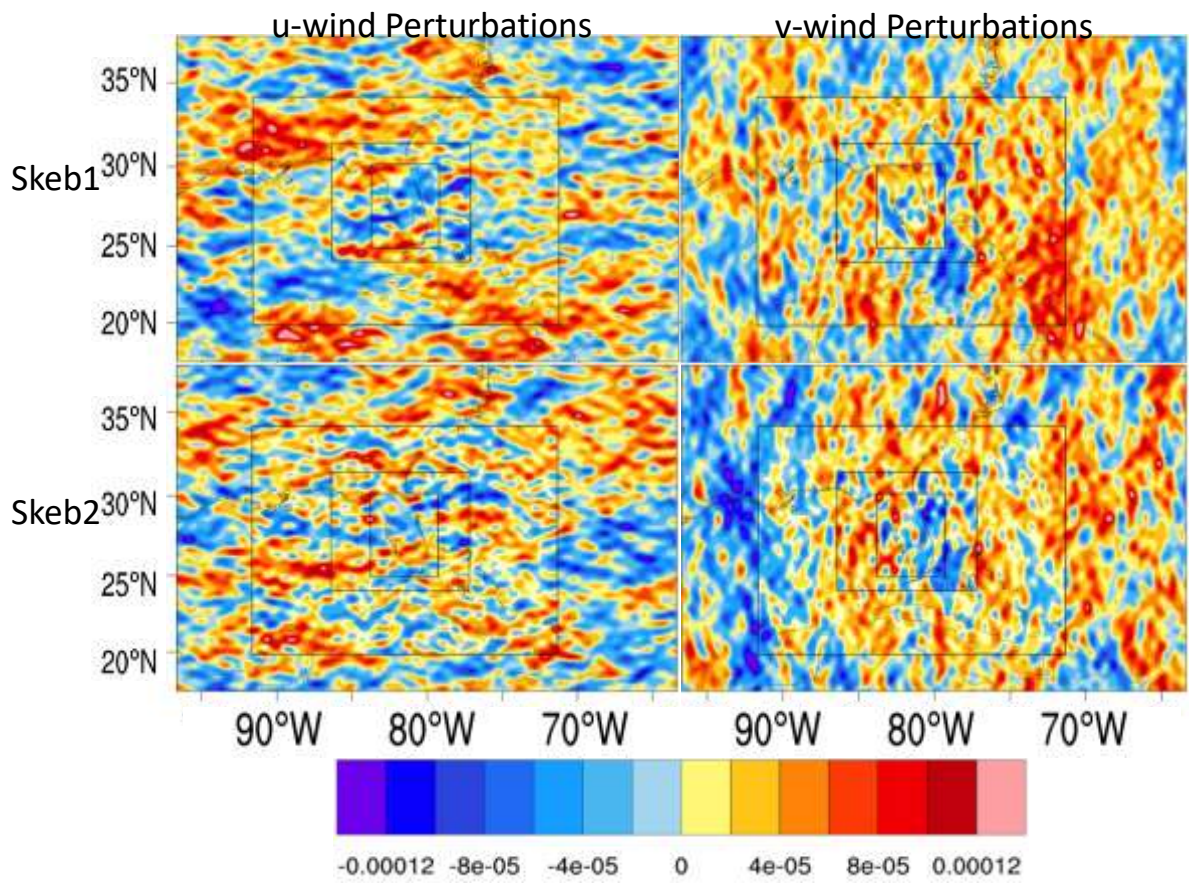

Figure 5.2 Output of u-wind (left) and v-wind (right) perturbation tendency fields (color, units m^2s^{-3}) for SKEBS simulation Skeb1 (top) and Skeb2 (bottom). Domain areas are the black boxes.

Table 5.1 Summary of SKEB simulations' SB CI timing errors (min), maximum SB depth, and SB merger time for gray-zone domains d03 and d04. Zero offset on SB initiation timing is indicated by a green checkmark, blue indicates premature SB formation and red indicates delayed SB formation, as compared to observational data. Simulations in bold indicate simulations that produced a strongly westward propagating ECSB, while simulations that are underlined indicate simulations that produced an almost stationary ECSB.

| | Initiation Timing Offset (min) | | | | | | Average SBF Depth (m) | | | |
| | WCSB | | ECSB | | SB Merger | | WCSB | | ECSB | |
Simulation	D03	D04	D03	D04	D03	D04	D03	D04	D03	D04
Skeb1	✓	✓	✓	✓	+60	+30	850	950	850	900
Skeb2	✓	✓	✓	✓	+30	-20	1000	1100	900	950
Skeb3	-30	-30	✓	✓	+60	-20	1000	1100	900	950
Skeb4	✓	✓	-30	-30	+90	-10	750	900	700	850
<u>Skeb5</u>	✓	✓	-30	-30	+90	+50	650	700	700	750
Skeb6	+30	+30	-60	-60	+50	+10	850	950	800	900
Skeb7	-30	-30	-30	-30	+60	+70	900	950	800	900
Skeb8	✓	✓	✓	✓	-10	-30	1100	1250	900	950
Skeb9	✓	✓	✓	✓	+40	-10	900	1000	500	750
<u>Skeb10</u>	-30	-30	-60	-60	+70	✓	800	900	900	950
Skeb11	✓	✓	-30	-30	+120	+10	900	950	850	900
<u>Skeb12</u>	✓	✓	-30	-30	+90	+50	850	950	1000	1200
Skeb13	✓	✓	-30	-30	+70	+10	900	1000	850	950
Skeb14	✓	✓	-30	-30	+70	+10	950	1050	900	950
Skeb15	-30	-30	✓	✓	+70	-10	850	950	700	800
<u>Skeb16</u>	-30	-30	-30	-30	+90	+40	850	900	900	950
<u>Skeb17</u>	-30	-30	✓	✓	+90	+40	800	950	900	1100
<u>Skeb18</u>	-30	-30	-30	-30	+100	+50	700	850	850	1200
Skeb19	✓	✓	✓	✓	+10	-30	950	1100	800	950
Skeb20	+30	+30	✓	✓	+130	+90	850	950	800	900
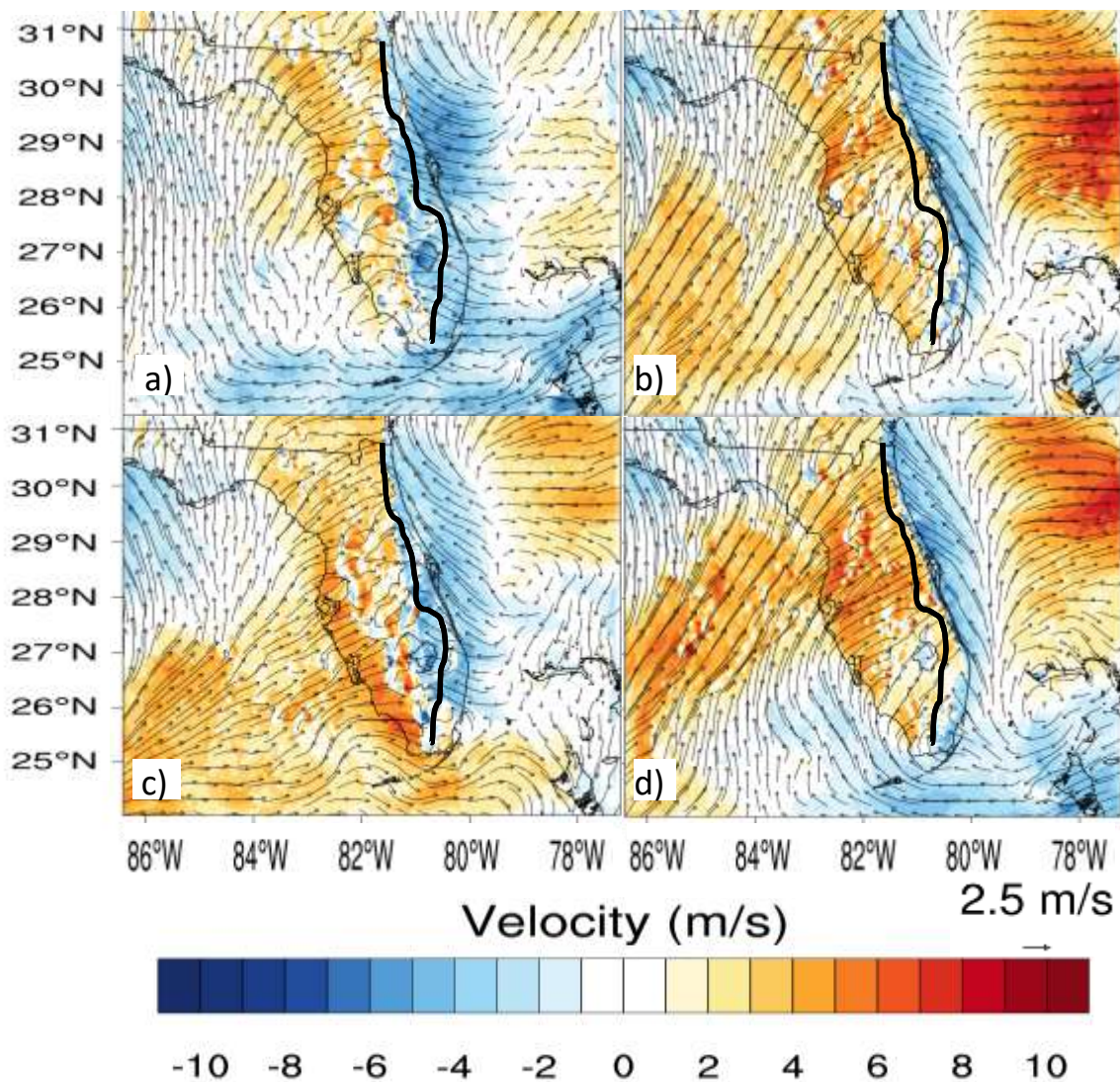
Figure 5.3 SKEB simulation of u-wind field at 2130 UTC 6 September 2012 for a) Skeb16, b) Skeb8, c) Skeb18, and d) Skeb9. Location of the ECSB at this same time for the CTRL simulation is the dark black line. Note the variance between the Ensemble members on the varying distances of the ECSB inland propagation.

Figure 5.4 Cross section (through northernmost red line in Figure 3.1) of d03 WRF-simulated zonal (u-component) winds (color: red easterly, blue westerly, units m s^{-1}) and total horizontal wind (black arrows, reference vector 10 m s^{-1}) at 2130 UTC 6 September 2012 for a) Skeb8, b) Skeb9, c) Skeb16, and d) Skeb18.

Table 5.2 Summary of SKEB simulations' average Threat Score, Bias Scores, and SB CI timing errors (min) for gray-zone domains d03 and d04. "Best" RMSE forecasts are in boldface and "worst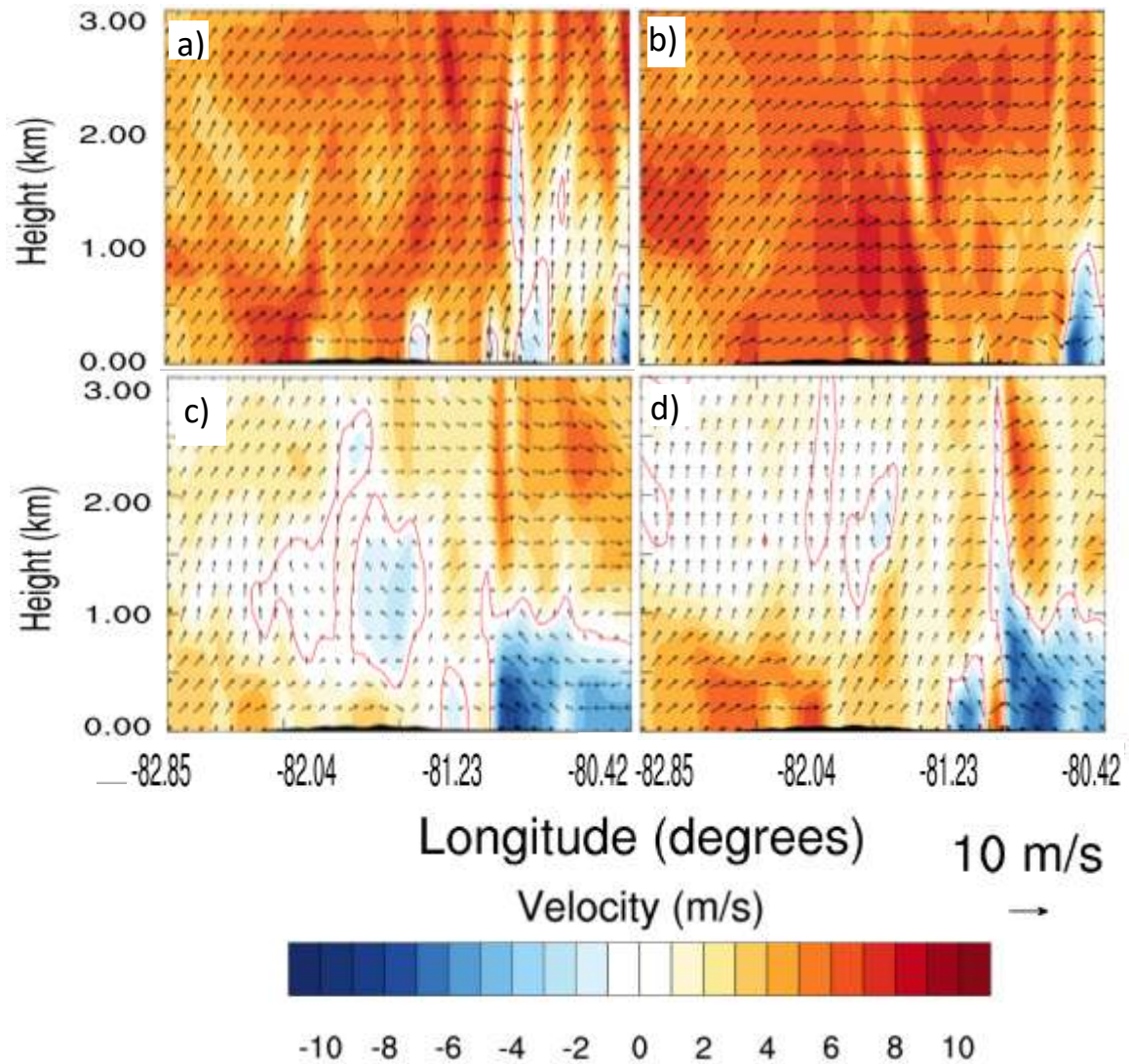" RMSE forecasts in gray italic (see Section 3.3.2 for definition of best and worst). Zero offset on SB CI timing is indicated by a green checkmark, blue indicates premature CI and red indicates delayed CI, as compared to Stage IV analysis data.

| | Avg Threat Score | | Avg Bias Score | | Timing Offset (min) | | | | | |
| | | | | | WCSB CI | | ECSB CI | | End of CI | |
Simulation	D03	D04	D03	D04	D03	D04	D03	D04	D03	D04
Skeb1	**0.15**	**0.24**	**0.96**	**0.31**	✓	✓	+60	✓	-60	-60
Skeb2	0.08	0.16	0.15	0.16	✓	✓	+60	✓	✓	-60
Skeb3	0.10	0.15	0.22	0.21	-60	✓	+60	✓	✓	✓
Skeb4	0.08	0.13	0.15	*0.10*	✓	✓	+60	✓	-120	-180
Skeb5	0.10	0.14	*2.47*	0.25	✓	✓	+120	✓	+120	+120
Skeb6	**0.15**	0.19	2.30	0.21	✓	✓	+120	-60	+60	✓
Skeb7	0.09	0.16	0.09	0.18	✓	✓	+60	✓	✓	-60
Skeb8	0.12	0.15	0.36	0.19	✓	✓	+60	-60	+60	-120
Skeb9	*0.04*	0.10	0.05	0.15	✓	✓	+60	-60	✓	✓
Skeb10	0.10	0.14	0.89	0.16	✓	✓	+60	✓	+60	-60
Skeb11	0.12	0.18	*2.74*	0.26	✓	✓	✓	-60	+60	✓
Skeb12	**0.15**	0.15	1.90	0.17	✓	✓	+60	✓	+60	✓
Skeb13	0.08	*0.09*	1.34	*0.09*	✓	✓	+60	-60	+60	+60
Skeb14	0.11	0.15	0.12	0.17	✓	✓	✓	✓	-60	-60
Skeb15	0.13	0.16	2.34	0.28	+180	+60	+60	✓	+60	+60
Skeb16	**0.15**	**0.21**	2.17	0.27	✓	✓	+60	-60	+120	+60
Skeb17	0.07	0.11	0.09	*0.10*	✓	✓	✓	✓	+60	-120
Skeb18	0.11	0.15	**0.99**	0.13	+60	✓	+60	-60	✓	✓
Skeb19	0.14	0.18	2.46	**0.32**	✓	✓	✓	✓	+120	-120
Skeb20	*0.05*	*0.09*	0.13	0.13	✓	✓	+60	✓	+60	-60
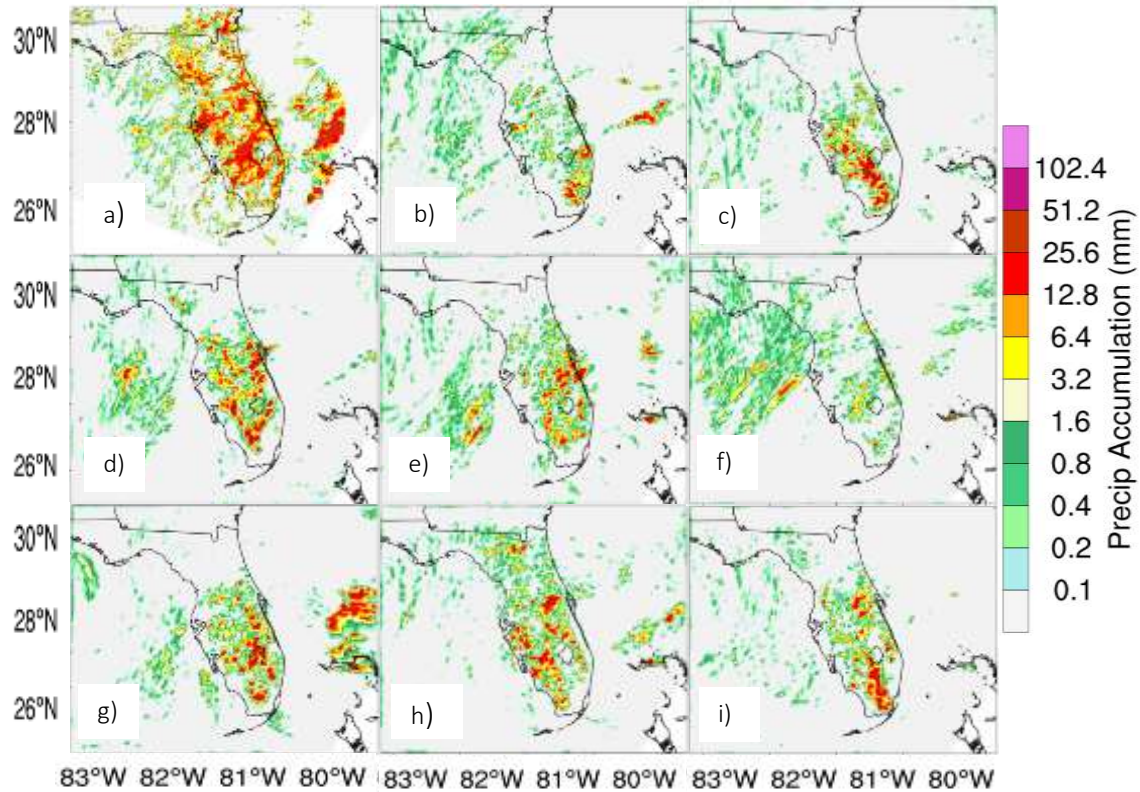
Figure 5.5 18-h (1200 UTC 6 September 2012 to 0600 UTC 7 September 2012) rainfall accumulation totals (color, units mm h^{-1}) for: a) CCPA analysis, b) Skeb4 simulation, c) Skeb5 simulation, d) Skeb6 simulation, e) Skeb8 simulation, f) Skeb9 simulation, g) Skeb15 simulation, h) Skeb16 simulation, and i) Skeb18 simulation.

Table 5.3 Summary of impact on SB and its associated CI by CU, MP, PBL physics parameterizations, ICs, stochastic parameterizations, and grid scale. Factors that have a smaller impact on the SB or CI are indicated with a *.

Factor (simulation)	SB		CI		
	Timing	Intensity	Timing	Location	Intensity
Cumulus (CU)			*	*	*
Microphysics (MP)			*	*	*
Boundary Layer (PBL)	X	X	X	X	X
Initial Conditions (ICs)	*	*	X	*	*
Stochastic (SKEBS)	X	X	X	X	X
Grid Scale		X	X	X	X

CHAPTER 6

SUMMARY AND CONCLUDING REMARKS

This study conducted a series of gray-zone grid scale simulations of an enhanced

WCSB or "Type 3" SB convective event (Blanchard and Lopez 1985) that occurred 6-7

September 2012. Results from a CTRL simulation indicate that with the state-of-the-art

WRF model, the FL SBs and their associated convection can be accurately simulated at

the gray-zone scale, although discrepancies are found in the timing, spatial location, and

intensity of convective cells produced when compared to surface data and Stage IV and

CCPA precipitation analyses. Further studies of 20 simulations varying the physics

parameterizations and initial conditions (P/IC) within the WRF-ARW model are

conducted in order to examine the sensitivities of the model to the initiation of the SB and

its associated convection. An additional 20 simulations using a stochastic kinetic energy

backscatter scheme (SKEBS) are conducted and analyzed in order to identify additional

sensitivities of the numerical simulations of SB and its CI to unresolved scales of motion

and subgrid energy effects within the model.

The results of the 40 numerical simulations show that the FL SB and its

associated convection is most sensitive to the PBL and SKEBS parameterizations, ICs,

and gray-zone grid spacing. Further analysis of the P/IC simulations and a grid spacing

comparison shows that the specific representation of geophysical features (e.g., coastline

shape and lake resolution) are important for resolving atmospheric variables, such as sensible surface heating, synoptic winds, surface moisture, and low-level convergence, that effect the development of the SB in determining the strength of the SBFs (and other boundary convergence lines such as LBs) within the WRF-ARW simulation. Accurate representations of the SBFs and LBs are important for the better representation of the timing and location of the SB CI in the case study. However, the gray-zone grid spacing seems to have issues in resolving the correct precipitation intensities of the SB convection, especially in the lowest gray-zone grid domain (1-km), most likely due to issues with the bulk parameterization schemes used in the P/IC configurations.

SKEBS simulations showed a much larger variability in the SB timing and intensity as compared to the P/IC simulations, indicating that the method of transported kinetic energy at unresolved scales upscale may be too generally applied in the model. Furthermore, it is also found that the addition of the SKEBS to the CTRL configuration showed a general improvement in the d03 grid spacing forecasts of convective precipitation intensities. However this improvement was not seen in d04 indicating that the SKEBS configuration in the model may be too broad in its application of the perturbations and that applying a stochastic parameterization in a more physically consistent manner may need to be considered in order to prevent degradation of the simulation as seen in the spurious intensities of the SB in some of the SKEBS simulations (i.e., too strong a ECSB or WCSB producing an erroneous SBF merger location). Ensuring that turbulent perturbation amplitudes remain in the variability of the boundary layer may be one consideration in creating a physically based stochastic perturbation method.

Limitations of this study are found in its scope, as it presents only one SB case and utilized a relatively small sample size for the number of simulation members within

the P/IC and SKEBS ensembles. Future work should include additional FL SB case studies (e.g., "Type 1" and "Type 2" SBs as classified by Blanchard and Lopez 1985) of the P/IC and SKEBS numerical simulations at terra incognita grid scales so as to verify results found in this single case study. In addition, as only a small sample of the physics options and SKEBS configurations within the WRF-ARW are used for the small sample size of the ensembles of P/IC and SKEBS ensembles, a more comprehensive evaluation of the sensitivity of the SB CI to the various physics and stochastic parameterization options through increased ensemble size is warranted. Furthermore, since the NAM and GFS initialization data showed similar results, a more comprehensive study using different initialization data such as the Canadian Global Deterministic Prediction System (GDPS), the European Center for Medium Range Weather Forecast Integrated Forecast System (ECMWF), or the UK Met Office Unified Model (UKMO) and IC starting times could result in a larger sensitivity to IC choice than shown here, and is worthy of future study.

As decreasing the gray-zone grid scale shows the most consistent improvement in the realistic forecasts for the locations and timing of the SB and CI, the upcoming plans of the operational modeling centers to produce regional NWP models at gray-zone scale seem to be advantageous, at least for diurnally-forced weather features such as the SB, that would find the higher resolution land-surfaces in the gray-zones to aid in their accurate forecasts. However, the gray-zone grid scale still shows issues in handling parameterizations, as seen in the inaccuracies of convective intensity found by going to higher gray-zone resolutions. Thus, research needs to continue on improvements of parameterization processes, both for physics and stochastic parameterizations.

In conclusion, the resulting connection made here between land surface resolution, low-level atmospheric variables, upscale subgrid energy forcing, SB strength, and convective initiation can help bridge the gap between the small-scale lower atmospheric processes and larger-scale convective dynamics of the SB thunderstorm systems. If our case study results of the sensitivities of the SB and CI to PBL and SKEBS parameterization and grid scale spacing hold true with further case studies, this information can aid in the improvement of parameterization design and use within the gray-zone. This could result in an improvement of the gray-zone numerical model's ability to resolve the CI processes associated with the SBs along the FL peninsula and other peninsular locations globally.

REFERENCES

Abbs, D.J. and W.L. Physick, 1992: Sea-breeze observations and modeling: A review. *Aust. Meteor. Mag.*, **41,** 7-19.

Abulikemu, A., Xin Xu, Y. Wang, J.F. Ding, S. Zhang, and W. Shen, 2016: A modeling study of convection initiation prior to the merger of a sea-breeze front and a gust front. *Atmos. Res.,* **182**, 10-19, doi: 10.1016/j.atmosres.2016.07.003.

Arritt, R.W., 1993: Effects of the large-scale flow on characteristics features of the sea breeze, *J. Appl. Meteor.,* **32**, 116-125, doi: 10.1175/1520-0450(1993)032<0116:EOTLSF>2.0.CO;2.

Arakawa, A., 2004: The cumulus parameterization problem: past, present, and future. *J. Climate,* **17,** 2493-2525, doi: 10.1175/1520-0442(2004)017<2493:RATCPP>2.0.CO;2.

Atkins, N.T. and R.M. Wakimoto, 1997: Influence of the synoptic-scale flow on sea breezes observed during CaPE. *Mon. Wea. Rev.*, **125**, 2112-2130, doi: 10.1175/1520-0493(1997)125<2112:IOTSSF>2.0.CO;2.

Baker, R.D., B.H. Lynn, A. Boone, W. Tao, and J. Simpson, 2001: The influence of soil moisture, coastline curvature, and land-breeze circulations on sea-breeze-initiated precipitation. *J. Hydrometeor.,* **2,** 193-211, doi: 10.1175/1525-7541(2001)002<0193:TIOSMC>2.0.CO;2.

Barnston, A.G., 1992: Correspondence among the correlation, RMSE, and Heidke forecast verification measures: refinement of the Heidke score. *Wea. Forecasting,* **7,** 699-709, doi: 10.1175/1520-0434(1992)007<0699:CATCRA>2.0.CO;2.

Bechtold, P., J.P. Pinty, and F. Mascart, 1991: A numerical investigation of the influence of large-scale winds on sea-breeze- and inland-breeze-type circulations. *J. Appl. Meteor.,* **30,** 1268-1279, doi: 10.1175/1520-0450(1991)030<1268:ANIOTI>2.0.CO;2.

Berner, J., F. J. Doblas-Reyes, T. N. Palmer, G. Shutts, and A. Weisheimer, 2008: Impact of a quasi-stochastic cellular automaton backscatter scheme on the systematic error and seasonal prediction skill of a global climate model. *Philos. Trans. Roy. Soc. London*, **366A**, 2561–2579, doi: 10.1098/rsta.2008.0033.

Berner, J., M. L. G. Shutts, and T. Palmer, 2009: A spectral stochastic kinetic energy backscatter scheme and its impact on flow-dependent predictability in the ECMWF ensemble prediction system. *J. Atmos. Sci.*, **66**, 603–626, doi: 10.1175/2008JAS2677.1.

Berner, J, S.Y. Ha, J.P. Hacker, A. Fournier, and C. Snyder, 2011: Model uncertainty in a mesoscale ensemble prediction system: Stochastic versus multiphysics representations. *Mon. Wea. Rev.,* **139,** 1972-1995, doi: 10.1175/2010MWR3595.1.

Berner, J., T. Jung, and T.N. Palmer, 2012: Systematic model error: the impact of increased horizontal resolution versus improved stochastic and deterministic parameterizations. *J. Climate*, **25,** 4946-4962, doi: 10.1175/JCLI-D-11-00297.1.

Berri, G.J. and J. Paegle, 1990: Sensitivity of local predictions to initial conditions. *J. Appl. Meteor.* **29,** 256-267, doi: 10.1175/1520-0450(1990)029<0256:SOLPTI>2.0.CO;2.

Blanchard, D.O. and R.E. Lopez, 1985: Spatial patterns of convection in south Florida. *Mon. Wea. Rev.,* **113,** 1282-1299, doi: 10.1175/1520-0493(1985)113<1282:SPOCIS>2.0.CO;2.

Boybeyi, Z. and S. Raman, 1992: A three-dimensional numerical sensitivity study of convection over the Florida peninsula, *Boundary-Layer Meteor.*, **60**, 325-359, doi: 10.1007/BF00155201.

Burpee, R.W. and L.N. Lahiff, 1984: Area-average rainfall variations on sea-breeze days in south Florida. *Mon. Wea. Rev.,* **112**, 520-535, doi: 10.1175/1520-0493(1984)112<0520:AARVOS>2.0.CO;2.

Byers, H.R. and H.R. Rodebush, 1948: Causes of thunderstorms of the Florida peninsula. *J. Meteor.,* **5,** 275-280, doi: 10.1175/1520-0469(1948)005<0275:COTOTF>2.0.CO;2.

Challa, V.S., J. Indracanti, M.K. Rabarison, C. Patrick, J.M. Baham, J. Young, R. Hughes, M.G. Hardy, S.J. Swanier, and A. Yerramilli, 2009: A simulation study of mesoscale coastal circulations in Mississippi Gulf coast. *Atmos. Res.,* **91,** 9-25, doi: 10.1016/j.atmosres.2008.05.004.

Charron, M., G. Pellerin, L. Spacek, P.L. Houtekamer, N. Gagnon, H.L. Mitchell, and L. Michelin, 2010: Toward random sampling of model error in the Canadian ensemble prediction system. *Mon. Wea. Rev.,* **138,** 1877-1901, doi: 10.1175/2009MWR3187.1.

Christensen, H.M., J. Berner, D.R.B. Coleman, and T.N. Palmer, 2017: Stochastic parameterization and El Nino-Southern Oscillation. *J. Climate,* **30,** 17-38, doi: 10.1175/JCLI-D-16-0122.1.

Clark, P.A., K.A. Browning, R.M. Forbes, C.J. Morcrette, A.M. Blyth, and H.W. Lean, 2014: The evolution of an MCS over southern England. Part 2: Model simulations and sensitivity to microphysics, *Quart. J. Roy. Meteor. Soc.,* **140**, 458-479.

Cohen, A.E., S.M. Cavallo, M.C. Coniglio, and H.E.. Brooks, 2015: A review of planetary boundary layer parameterization schemes and their sensitivity in simulating southeastern U.S. cold season severe weather environments. *Wea. Forecasting,* **30,** 591-612, doi: 10.1175/WAF-D-14-00105.1.

Cohen, C., 2002: A comparison of cumulus parameterizations in idealized sea-breeze simulations. *Mon. Wea. Rev.,* **130,** 2554-2571, doi: 10.1175/1520-0493(2002)130<2554:ACOCPI>2.0.CO;2.

Colby Jr., F.P., 2004: Simulation of the New England sea breeze: The effect of grid spacing. *Wea. Forecasting,* **19,** 277-285, doi: 10.1175/1520-0434(2004)019<0277:SOTNES>2.0.CO;2.

Crosman, E.T. and J.D. Horel, 2010: Sea and lake breezes: A review of numerical studies. *Bound.-Layer Meteor.,* **137,** 1-29, doi: 10.1007/s10546-010-9517-9.

Duda, J.D., X. Wang, F. Kong, M. Xue, and J. Berner, 2016: Impact of a stochastic kinetic energy backscatter scheme on warm season convection-allowing ensemble forecasts. *Mon. Wea. Rev.,* **144,** ,1887-1908, doi: 10.1175/MWR-D-15-0092.1.

Etherton, B. and P. Santos, 2008: Sensitivity of WRF forecasts for south Florida to initial conditions. *Wea. Forecasting,* **23,** 725-740, doi: 10.1175/2007WAF2006115.1.

Evans, J.P. Ekström, and F. Ji, 2012: Evaluating the performance of a WRF physics ensemble over south-east Australia. *Climate Dyn.,* **39,** 1241-1258, doi: 10.1007/s00382-011-1244-5.

Fankhauser, J.C., N.A. Crook, J. Tuttle, L.J. Miller, and C.G. Wade, 1995: Initiation of deep convection along boundary layer convergence lines in a semitropical environment. *Mon. Wea. Rev.,* **123,** 291-313, doi: 10.1175/1520-0493(1995)123<0291:IODCAB>2.0.CO;2.

Fovell, R.G., 2005: Convective initiation ahead of the sea-breeze front. *Mon. Wea. Rev.*, **133**, 264-278, doi: 10.1175/MWR-2852.1.

Gilliam, R.C., S. Raman, D.D.S. Niyogi, 2004: Observational and numerical study on the influence of large-scale flow direction and coastline shape on sea-breeze evolution. *Bound.-Layer Meteor.*, **111**, 275-300, doi: 10.1023/B:BOUN.0000016494.99539.5a.

Grell, G. A., and S. R. Freitas, 2014: A scale and aerosol aware stochastic convective parameterization for weather and air quality modeling. *Atmos. Chem. Phys.*, **14**,

5233–5250, doi:10.5194/acp-14-5233-2014.

Grenier, H. and C.S. Bretherton, 2001: A moist PBL parameterization for large-scale models and its application to subtropical cloud-topped marine boundary layers. *Mon. Wea. Rev.,* **129,** 357-377, doi: 10.1175/1520-0493(2001)129<0357:AMPPFL>2.0.CO;2.

Ha, S., J. Berner, and C. Snynder, 2015: A comparison of model error representations in mesoscale ensemble data assimilation. *Mon. Wea. Rev.*, **143,** 3893-3911.

Hahmann, A.N., Y. Liu, and T. T. Warner, 2006: Mesoscale circulations over the Athens metropolitan area during the 2004 summer Olympic games. *Joint Forum on Managing our Physical and Natural Resources and 6th Symp. on the Urban Environment,* Atlanta, GA, Amer. Meteor. Soc., J9.3. [Available online at https://ams.confex.com/ams/Annual2006/techprogram/paper_105087.htm.]

Halverson, J., M. Garstang, J. Scala, W.-K. Tao, 1996: Water and energy budgets of a Florida mesoscale convective system: A combined observational and model study, *Mon. Wea. Rev.*, **124**, 1161-1180, doi: 10.1175/1520-0493(1996)124<1161:WAEBOA>2.0.CO;2.

Han, J. and H. Pan, 2011: Revision of convection and vertical diffusion schemes in the NCEP global forecast system. *Wea. Forecasting,* **26,** 520-533, doi: 10.1175/WAF-D-10-05038.1.

Haurwitz, B., 1947: Comments on the sea-breeze circulation. *J. of Meteor.,* **40,** 1-8, doi: 10.1175/1520-0469(1947)004<0001:COTSBC>2.0.CO;2.

Hong, S.Y. and J.O.J. Lim, 2006: The WRF single-moment 6-class microphysics scheme (WSM6). *J. Korean Meteor. Soc.,* **42,** 129-151.

Hong, S.Y., Y. Noh, and J. Dudhia, 2006: A new vertical diffusion package with an explicit treatment of entrainment processes. *Mon. Wea. Rev.,* **134,** 2318-2341, doi: 10.1175/MWR3199.1.

Hong, S.Y. and J. Dudhia, 2012: Next-generation numerical weather prediction. Bridging parameterization, explicit clouds, and large eddies. *Bull. Amer. Meteor. Soc.,* **93,** ES6-ES9, doi: 10.1175/2011BAMS3224.1.

Hou, D., M. Charles, Y. Luo, Z. Toth, Y. Zhu, R. Krzysztofowicz, Y. Lin, P. Xie, D.J., Seo, M. Pena, and B. Cui, 2014: Climatology-calibrated precipitation analysis at fine scales: Statistical adjustment of stage IV toward CPC gauge-based analysis. *J. of Hydrol.,* **15**, 2542-2557, doi: 10.1175/JHM-D-11-0140.1.

Janjic´, Z. I., 1994: The step-mountain Eta coordinate model: Further developments of the convection, viscous sublayer, and turbulence closure schemes. *Mon. Wea.*

Rev.,**122**, 927–945, doi: 10.1175/1520-0493(1994)122<0927:TSMECM>2.0.CO;2.

Kain, J. S., and J. M. Fritsch, 1993: Convective parameterization for mesoscale models: The Kain–Fritsch scheme. The Representation of Cumulus Convection in Numerical Models, Meteor. Monogr., No. 46, Amer. Meteor. Soc., 165–170, doi: 10.1007/978-1-935704-13-3_15.

Kain, J. S., 2004: The Kain-Fritsch convective parameterization: an update. *J. Appl. Meteor.,* **43**, 170-181, doi: 10.1175/1520-0450(2004)043<0170:TKCPAU>2.0.CO;2.

Kalnay, E., 2003: *Atmospheric Modeling, Data Assimilation and Predictability*. Cambridge University Press, 341 pp.

Knievel, J.C., D.L. Rife, J.A. Grim, A.N. Hahmann, J.P. Hacker, M. Ge, and H.F. Fisher, 2010: A simple technique for creating regional composites of sea surface temperature from MODIS for use in operational mesoscale NWP. *J. Appl. Meteor. Climatol.,* **49**, 2267-2284, doi: 10.1175/2010JAMC2430.1.

Laird, N.F., D.A.R. Kristovich, R.M. Rauber, H.T. Ochs, and L.J. Miller, 1995: The Cape Canaveral sea and river breezes: Kinematic structure and convective initiation, *Mon. Wea. Rev.*, **123**, 2942-2956, doi: http://dx.doi.org/10.1175/1520-0493(1995)123<2942:TCCSAR>2.0.CO;2.

Lin, Y.L., R.D. Farley, and H.D. Orville, 1983: Bulk parameterization of the snow field in a cloud model. *J. Climate Appl. Meteor.,* **22,** 1065-1092, doi: 10.1175/1520-0450(1983)022<1065:BPOTSF>2.0.CO;2.

Lin Y. and B.A. Colle, 2011: A new bulk microphysical scheme that includes riming intensity and temperature-dependent ice characteristics. *Mon. Wea. Rev.,* **139,** 1013-1035, doi: 10.1175/2010MWR3293.1.

Lin, Y., and K.E. Mitchell, 2005: The NCEP stage II/IV hourly precipitation analyses: Development and applications. Preprints, *19th Conf. on Hydrology,* San Diego, CA, Amer. Meteor. Soc., 1.2. [Available online at https://ams.confex.com/ams/pdfpapers/83847.pdf.]

Lock, N.A and A.L. Houston, 2014: Empirical examination of the factors regulating thunderstorm initiation. *Mon. Wea. Rev.,* **142**, 240-258.

Lombardo, K., E. Sinsky, Y. Jia, M.M. Whitney, and J. Edson, 2016: Sensitivity of simulated sea breezes to initial conditions in complex coastal regions. *Mon. Wea. Rev.,* **144,** 1299-1320, doi: 10.1175/MWR-D-15-0306.1.

Mesinger, F., G. Dimego, E. Kalnay, K. Mitchell, P. Shafran, W. Ebisuzaki, D. Jovic, J. Woollen, E. Rogers, E. Berbery, M. Ek, Y. Fan, R. Grumbine, W. Higgins, H. Li, Y. Li, G. Manikin, D. Parrish, W. Shi, 2006: North American Regional Reanalysis. *Bull.*

Amer. Meteor. Soc., **87.3**, 343-360, doi: 10.1175/BAMS-87-3-343.

Miao, J.F., K. Wyser, D. Chen, and H. Ritchie, 2009: Impacts of boundary layer turbulence and land surface process parameterizations on simulated sea breeze characteristics. *Ann. Geophys.,* **6,** 2303-2320, doi: 10.5194/angeo-27-2303-2009.

Miller, S.T.K., B.D. Keim, R.W. Talbot, and H. Mao, 2003: Sea breeze: Structure, forecasting, and impacts. *Rev. Geophys.,* **41,** 1/1-131, doi: 10.1029/2003RG000124.

Morrison, H., G. Thompson, and V. Tatarskii, 2009: Impact of cloud microphysics on the development of trailing stratiform precipitation in a simulated squall line: comparison of one- and two-moment schemes. *Mon. Wea. Rev.,* **137,** 991-1007, doi: 10.1175/2008MWR2556.1.

Nakanishi, M. and H. Niino, 2006: An improved Mellor-Yamada level-3 model: Its numerical stability and application to a regional prediction of advection fog. *Boundary-Layer Meteor.,* **119,** 397-407, doi: 10.1007/s10546-005-9030-8.

Nicholls, M.E., R.A. Pielke, and W.R. Cotton, 1991: A two-dimensional numerical investigation of the interaction between sea breezes and deep convection over the Florida peninsula, *Mon. Wea. Rev.,* **119**, 298-323, doi: http://dx.doi.org/10.1175/1520-0493(1991)119<0298:ATDNIO>2.0.CO;2.

Ogawa, S., W. Sha, and T. Iwasaki, 2003: A numerical study on the interaction of a sea-breeze front with convective cells in the daytime boundary layer. *J. Meteor. Soc. Japan*, **81,** 635-651, doi http://doi.org/10.2151/jmsj.81.635.

Pielke, R.A., 1974: A comparison of three-dimensional and two-dimensional numerical predictions of sea breezes. *J. Atmos. Sci,* **31,** 1577-1585, doi: http://dx.doi.org/10.1175/1520-0469(1974)031<1577:ACOTDA>2.0.CO;2.

Pleim, J.E., 2007: A combined local and nonlocal closure model for the atmospheric boundary layer. Part I: Model description and testing. *J. Appl. Meteor. Climatol.,* **46,** 1383-1395, doi: 10.1175/JAM2539.1.

Randall, D.A., R.A. Wood, S. Bony, R. Colman, T. Fichefet, J. Fyfe, V. Kattsov, A. Pitman, J. Shukla, J. Srinivasan, R.J. Stouffer, A. Sumi and K.E. Taylor, 2007: Climate Models and Their Evaluation. *Climate Change 2007: The Physical Science Basis. Contribution of Working Group I to the Fourth Assessment Report of the Intergovernmental Panel on Climate Change,* S. Solomon, D. Qin, M. Manning, Z. Chen, M. Marquis, K.B. Averyt, M.Tignor and H.L. Miller, Eds. Cambridge University Press., pp. 601.

Rao, P.A. and H.E. Fuelberg, 2000: An investigation of convection behind the Cape Canaveral sea-breeze front. *Mon. Wea. Rev.*, **128**, 3437-3458, doi: http://dx.doi.org/10.1175/1520-0493(2000)128<3437:AIOCBT>2.0.CO;2.

Romine, G.S., C.S. Schwartz, J. Berner, K.R. Fossell, C. Snyder, J.L. Anderson, and M.L. Weisman, 2014: Representing forecast error in a convection-permitting ensemble system. *Mon. Wea. Rev.,* **142,** 4519-4541, doi: 10.1175/MWR-D-14-00100.1.

Rubes, M.T., H.J. Cooper, and E.A. Smith, 1993: A study of the Merritt Island, Florida sea breeze flow regimes and their effect on surface heat and moisture fluxes, *NASA Contract. Rep.* 4537, 141 pp., NASA, Greenbelt, Md., 1993.

Segal, M., M. Leuthold, R.W. Arritt, C. Anderson, and J. Shen, 1997: Small lake daytime breezes: Some observational and conceptual evaluations. *Bull.Amer. Meteor. Soc.,* **6**, 1135-1147.

Shutts, G., 2005: A kinetic energy backscatter algorithm for use in ensemble prediction systems. *Quart. J. Roy. Meteor. Soc.,* **131,** 3079-3102, 10.1256/qj.04.106.

Skamarock, W.C., J.B. Klemp, J. Dudhia, D.O. Gill, D.M. Barker, M.G. Duda, X. Huang, W. Wang, and J.G. Powers, 2008: A description of the Advanced Research WRF version 3. NCAR Tech. Note NCAR/TN-475+STR, 113 pp.

Song, J.-L., 1986: A numerical investigation of Florida's sea breeze-cumulonimbus interactions. Ph.D. dissertation, Dept. of Atmos. Sci., Colorado State University, 187 pp.

Srinivas, C. V., R. Venkatesan, K. M. Somayaji, and A. B. Singh, 2006: A numerical study of sea-breeze circulation observed at a tropical site Kalpakkam on the east coast of India, under different synoptic flow situations. *J. Earth Syst. Sci.,* **115**, 557–574, doi:10.1007/BF02702909.

Srinivas, C. V., R. Venkatesan, and A.B. Singh, 2007: Sensitivity of mesoscale simulations of land-sea breeze to boundary layer turbulence parameterization. *Atmospheric Environment,* **41,** 2534-2548, doi: 10.1016/j.atmosenv.2006.11.027.

Stenstrud, D.J., J.W. Bao, and T.T. Warner, 2000: Using initial condition and model physics perturbations in short-range ensemble simulations of mesoscale convective systems. *Mon. Wea. Rev., 128,* 2077-2107, doi: 10.1175/1520-0493(2000)128<2077:UICAMP>2.0.CO;2.

Sukoriansky, S., B. Galperin and V. Perov, 2005: Application of a new spectral theory of stably stratified turbulence to the atmospheric boundary layer over sea ice. *Boundary-Layer Meteor.,* **117,** 231-257, doi: 10.1007/s10546-004-6848-4.

The COMET Program (COMET). (2001). Thermally-forced circulation I: Sea breezes. The COMET©Program (Last updated 2 December, 2016). Retrieved 1 February, 2017, from http://www.meted.ucar.edu/mesoprim/seabreez/print.htm.

Thompson, G., P.R. Field, R.M. Rasmussen, and W.D. Hall, 2008: Explicit forecasts of winter precipitation using an improved bulk microphysics scheme. Part II: Implementation of a new snow parameterization. *Mon. Wea. Rev.*, **136**, 5095-5115, doi: 10.1175/2008MWR2387.1.

Tiedtke, M., 1993: Representation of clouds in large-scale models. *Mon. Wea. Rev.,* **121,** 3040-3061, doi: 10.1175/1520-0493(1993)121<3040:ROCILS>2.0.CO;2.

Trier, S.B., 2003: Convective storms: Convective initiation. *Encyclopedia of Atmospheric Sciences*, Academic Press.

Tripoli, G.J. and W.R. Cotton, 1980: A numerical investigation of several factors contributing to the observed variable intensity of deep convection over south Florida. *J. Appl. Meteor,* **19,** 1037-1063, doi: http://dx.doi.org/10.1175/1520-0450(1980)019<1037:ANIOSF>2.0.CO;2.

Ulanski, S.L. and M. Garstang, 1978: The role of surface divergence and vorticity in the life cycle of convective rainfall. Part I: Observation and analysis. *J. Atmos. Sci.*, **35**, 1047-1062, doi: 10.1175/1520-0469(1978)035<1047:TROSDA>2.0.CO;2.

Walsh, J.E., 1974: Sea breeze theory and applications. *J. of Atmos. Sci.,* **31**, 2012-2026, doi: 10.1175/1520-0469(1974)031<2012:SBTAA>2.0.CO;2.

Watson, L.R., B. Hoeth, P.F. Blottman, 2007: Weather research and forecasting model sensitivity comparisons for warm season convective initiation. *Preprints, 22nd Conf. on Wea. Analysis and Forecasting and 18th Conf. on Numerical Wea. Prediction*, Amer. Meteor. Soc., Park City, UT, J11A1. [Available online at https://ams.confex.com/ams/22WAF18NWP/techprogram/paper_124079.htm.]

Watson, L.R., and B.T. Zavodsky, 2015: High-resolution mesoscale model setup for the eastern range and Wallops flight facility. *19th Conf. on Integrated Observing and Assimilation Systems for the Atmosphere, Oceans, and Land Surface*, Phoenix, AZ, Amer. Meteor. Soc., 12A.3. [Available online at https://ams.confex.com/ams/95Annual/webprogram/Paper267445.html.]

Weaver, J.C., 2006: The impact of synoptic-scale flow on sea breeze front propagation and intensity at Eglin Air Force Base. M.S. thesis, Dept. of Meteor., Naval Postgraduate School, 129 pp.

Williams, S., K. Caeser, and K. Southwick, 1992: Convection and Precipitation Experiment operations summary and data inventory. Office of Field Project Support, Boulder, CO, 425 pp.

Wilson, J.W., and D.L. Megenhardt, 1997: Thunderstorm initiation, organization, and lifetime associated with Florida boundary layer convergence lines, *Mon. Wea. Rev.*, **125**, 1507-1525, doi: http://dx.doi.org/10.1175/1520-

0493(1997)125<1507:TIOALA>2.0.CO;2.

Wyngaard, J.C., 2004: Toward numerical modeling in the "terra incognita". *J. of Atmos. Sci.*, **61**, 1816-1826, doi: 10.1175/1520-0469(2004)061<1816:TNMITT>2.0.CO;2.

Xu, L., S. Raman, R.V. Madala, and R. Hodur, 1996: A non-hydrostatic modeling study of surface moisture effects on mesoscale convection induced by sea breeze circulation. *Meteor. Atmos. Phys.*, **58**, 103-122, doi: 10.1007/BF01027559.

Zhang, R. and T.L. Delworth, 2005: Simulated tropical response to a substantial weakening of the Atlantic thermohaline circulation, *J. Climate,* **18,** 1853-1860, doi: 10.1175/JCLI3460.1.